DOUBLE-LOOP MICROTRAP ARRAY FOR ULTRACOLD ATOMS

BIN JIAN

A DISSERTATION SUBMITTED TO
THE FACULTY OF GRADUATE STUDIES
IN PARTIAL FULFILLMENT OF THE REQUIREMENTS
FOR THE DEGREE OF
DOCTOR OF PHILOSOPHY

GRADUATE PROGRAM IN PHYSIC AND ASTRONOMY
YORK UNIVERSITY
TORONTO, ONTARIO

May 2014

Abstract

A novel kind of magnetic microtrap is demonstrated for ultracold neutral atoms. It consists of two concentric loops of radii r_1 and r_2 having oppositely oriented currents. A magnetic field minimum is generated in three dimensions that can be used to trap the atoms with a trap depth of about 1 mK using a current of 2.6 A. The condition $r_2/r_1 = 2.2$ maximizes the restoring force on the atoms toward the trap center. Unlike conventional magnetic microtraps, an external bias field is not required. Moreover, a one dimensional array of double-loop microtraps can be created by daisy chaining single microtrap circuits.

A linear array of three microtraps having $r_1 = 300$ μm was fabricated as part of an atom chip. The following three techniques were developed to load the microtrap array: 1) atoms initially contained in a magneto-optical trap (MOT) were transported to the atom chip by a conventional magnetic trap, 2) atoms were first loaded into a mirror MOT and 3) atoms were initially loaded in a far off resonance optical dipole trap (FORT). Each technique loaded greater than 10^5 ^{87}Rb atoms into the microtrap array. The lowest temperature of 30 μK for the microtrapped atom cloud was achieved using FORT loading. The strength and the position of the microtrap could be precisely adjusted over a range from 300 to 50 μm above the atom chip surface by applying an external bias magnetic field. The lifetime of the atoms trapped in the microtrap array was measured to be 350 ms which was limited by the collisions with residual background gas.

Acknowledgements

The work described in this thesis would not have been possible without the assistances and support from many people. I would like to extend my appreciation especially to the following.

First and foremost, I would like to express my gratitude to my supervisor, Dr. William A. van Wijngaarden. It is difficult to assess how much I learned from William over the past several years in his lab. His guidance and encouragement helped me get through the tough times and made all of this possible. His enthusiasm for physics and strong determination to overcome the difficulties left a deep impression on me and definitely will influence the rest of my life. As well, I acknowledge my committee members for providing insights during the course of my study.

My sincere thanks to all the labmates for their friendship, company, and assistance. Brad E. Schultz introduced the equipment in the lab to me and helped me get started with the experiment immediately after I joined the lab; Pengyi Zhao, the postdoc fellow in the lab in my first year, taught me various valuable tips and tricks of experimental skills; Isaac De Souza worked with me as an undergraduate research assistant towards the assembly of the microtrap array apparatus. His excellent machine shop skills freed me from the heavy duty of machine shop work and speeded up the progress dramatically; Ephrem Chemali and Jie Wang, working on the lithium spectroscopy experiment in the lab at different phases during my tenure, were always willing to stop their work to help me when I needed an extra pair of hands. At the same time, I would also like to thank Matthew George for loaning me numerous useful tools and giving valuable suggestions on constructing a microwave cavity.

I would like to acknowledge the technical, academic and financial support of York University and its staff. A thank you to Frank Canzona for his help provided in the machine shop. Many thanks to Marlene Caplan for always kind assistance on the administrative side. Furthermore, I am grateful to the financial support of the (International) Ontario Graduate Scholarship and the Provost Dissertation Scholarship of York University.

Last but not least, I would like to express my deepest thanks to my family for their constant support, understanding, and love.

Table of Contents

List of Tables

List of Figures

1 Introduction

1.1 Motivation

Precision spectroscopy has been an important tool to discover new physical phenomena. Measurements of spectral lines have been key to revealing fine and hyperfine structure [1, 2, 3] as well as the Lamb shift [4]. These measurements have in turn tested theory including quantum electrodynamics [5] and revealed effects such as the small contribution to isotope shifts due to the finite size of the nucleus [6]. A limitation in experimental accuracy is broadening of spectral lines due to the Doppler shift. This can be as large as 1 GHz for an atomic vapor in vacuum at room temperature. This was the prime motivation for work beginning about three decades ago to decrease the atomic velocities using laser cooling [7, 8, 9].

Laser cooling of atoms in three dimensions is now routinely done. Typically, atoms are collected from a background vapour [10] or from a decelerated atomic beam enclosed in a vacuum chamber [11, 12]. Millions of neutral atoms can be cooled to temperatures of a few μK above absolute zero [13, 14, 15]. At these low temperatures, the distance between atoms can be comparable to their de Broglie wavelength leading to the creation of a so called Bose Einstein Condensate (BEC) [16, 17]. The creation of a BEC in 1995 using a dilute gas of alkali atoms [18, 19] received the Physics Nobel Prize in 2001 [20, 21]. More recently, there has been work to generate ultracold atoms to study degenerate fermi gases [22].

Ultracold atoms in a vacuum must be trapped to avoid being accelerated by gravity. A variety of atom traps was therefore developed including using focussed

laser beams to generate an optical trap [23, 24, 25] as well as magnetic fields that interact with the atom's magnetic dipole moment [26]. Magnetic traps use a spatially varying magnetic field [27]. The so called quadrupole trap is particularly simple using two coaxial coils having oppositely oriented currents [26]. The atoms are then trapped at the zero field minima located midway between the two coils. A number of different types of magnetic traps have been demonstrated [28, 29, 30, 31, 32].

A challenge to trap ultracold atoms is that an ultra high vacuum (UHV) must exist to minimize collisions with background gas atoms and molecules that heat the atoms. Magnetic traps also require large field gradients generated by large currents in coils located close to the atoms. Magnetic microtraps were therefore proposed and developed that utilize wires as small as tens of microns [33, 34, 35, 36]. These wires are fabricated onto a chip using lithographic techniques [37]. These microtraps not only simplify the apparatus but also generate higher field gradients to tightly trap the atoms [38, 39]. Microtraps were first used to generate BECs on atom chips in 2001 [40, 41]. They have also been employed to study the interaction between ultracold atoms with a nearby surface [42, 43]. Other applications include studying the atom field coupling between BECs and an optical cavity [44, 45, 46]. There is also considerable interest in possible applications to quantum information processing [47].

This thesis demonstrates a new kind of magnetic microtrap. It consists of two concentric microwire loops having oppositely oriented currents. Unlike existing microtraps, it does not require a bias field created by macroscopic coils to generate a microtrap. Secondly, the arrangement of microwires is ideally suited to creating a one and even two dimensional array of microtraps [48]. Another novel feature of our double-loop microtrap is that its position relative to the chip surface can be precisely specified using a bias field.

This thesis is organized as follows. Chapter 1 discusses relevant background information. The following chapter describes the double-loop microtrap array in detail.

Chapter 3 discusses the apparatus. The next three chapters describe three different techniques to load atoms into the microtrap array that were experimentally demonstrated. Finally, Chapter 7 gives conclusions and discusses possible future work.

1.2 Rubidium

The alkali atoms are commonly used in experiments because their relatively low melting points facilitate the creation of atomic vapours and beams. They also can be excited from the ground state using visible or near infrared radiation which can be conveniently generated using dye and diode lasers. Finally, an alkali atom can be simply modelled as consisting of a single valence electron interacting with the closed electron core which shields the nucleus. Hence, an alkali atom is well approximated as a hydrogenic system for which theoretical calculations can be accurately performed [49, 50].

Rubidium is the alkali atom in the fourth row of the Periodic Table with the atomic number of 37. Its melting point is 39 °C. Rubidium has two stable isotopes, ^{87}Rb and ^{85}Rb, with abundances of 27.8% and 72.7%, respectively. The nuclear spin I of ^{87}Rb is 3/2 while that of ^{85}Rb is 5/2. Figure 1.1 shows the hyperfine levels comprising the D2 line of ^{87}Rb [51]. The hyperfine levels are labelled by quantum number F which is the vector sum of the electronic angular momentum of the valence electron and the nuclear spin. F has integral values of $\hbar = h/2\pi$ where h is Planck's constant, meaning that the rubidium atom behaves as a boson. ^{87}Rb was selected for this work because relatively inexpensive diode lasers were available that generated about 100 mW at the D2 wavelength of 780 nm.

1.3 Laser cooling

An atom interacting with a radiation field can absorb a photon and later reemit a photon via spontaneous emission. Assuming the laser remains on resonance, after

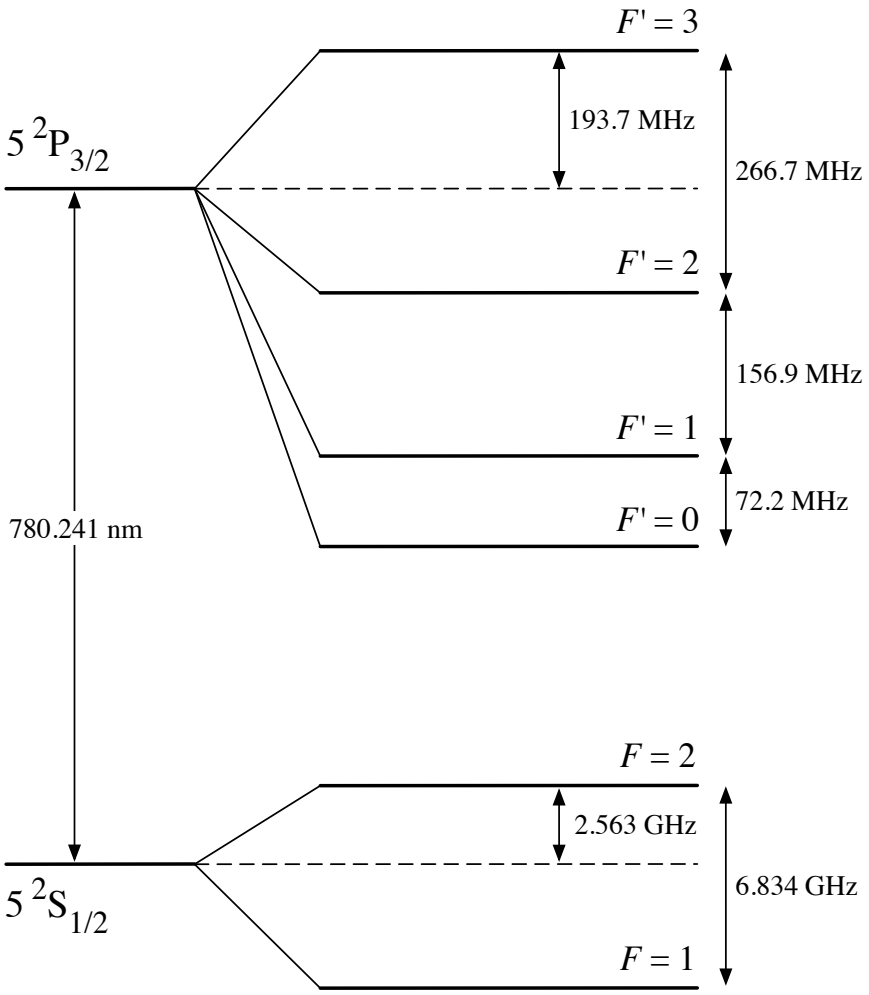

Figure 1.1: D2 line hyperfine structure of ^{87}Rb.

the absorption and reemission of N photons, the atom's momentum changes by an amount

$$M\Delta\vec{v} = N\hbar\vec{k} - \sum_{i=1}^{N} \hbar\vec{k_i}'. \tag{1.1}$$

Here M is the atom's mass, $\Delta\vec{v}$ is the change of the atom's velocity, $\vec{k}$ is the wavevector of the laser photon and $\vec{k}'$ is the wavevector of the reemitted photon. The radiated photon is emitted in a random direction. Hence, for a large value of N, the second term in the above equation averages to zero. The atom therefore experiences a force in the direction of the oncoming laser beam.

The dissipative force exerted by the laser on the atom can be expressed as [52, 53]

$$\vec{F} = \hbar\vec{k}\,\Gamma_{\mathrm{SC}}, \tag{1.2}$$

where Γ_{SC} is the photon scattering rate given by [52, 53]

$$\Gamma_{\mathrm{SC}} = \frac{\gamma}{2}\frac{I/I_s}{1 + I/I_s + (2\delta/\gamma)^2}. \tag{1.3}$$

Here γ equals the inverse of the excited state radiative lifetime τ and $\delta = \omega - \omega_0$ is the detuning of the laser angular frequency ω relative to the atom's transition angular frequency ω_0. I_s is the saturation intensity which is defined as

$$I_s = \frac{\pi hc}{3\lambda^3\tau}, \tag{1.4}$$

where c is the light speed and λ is the transition wavelength.

A complication to the simplified picture described above is that as the atom decelerates due to absorbing oncoming photons, it experiences a Doppler shift which shifts the laser out of resonance. The force on an atom moving with velocity $\vec{v}$ due to an oncoming laser beam propagating in the $\vec{k}$ direction is given by

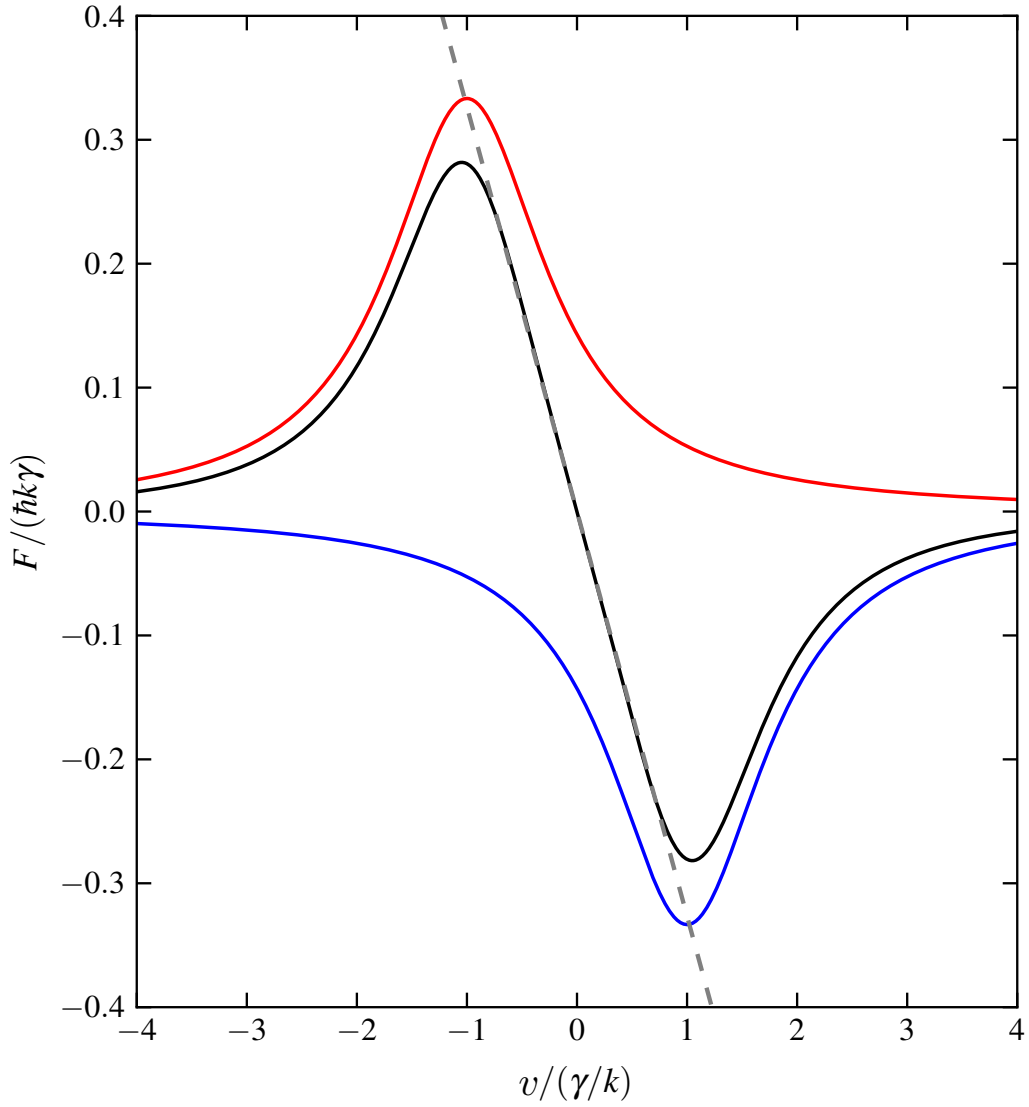

Figure 1.2: Total force (black curve) exerted on an atom moving with velocity v exerted by an oncoming laser (blue curve) and laser propagating in the opposite direction (red curve). Both laser beams are detuned below the atom's transition frequency such that $\delta = -\gamma$ and have equal intensities $I = 2I_s$. The grey dashed line is the linear approximation of the total force described by Equation 1.7.

$$\vec{F}(\vec{k}) = \hbar\vec{k}\frac{\gamma}{2}\frac{I/I_s}{1 + I/I_s + 4/\gamma^2\left(\delta - \vec{k}\cdot\vec{v}\right)^2}. \tag{1.5}$$

In order to stop an atom moving in one dimension, an atom must interact with two counterpropagating laser beams. The net force exerted on the atom is given by

$$\vec{F}_{\text{Tot}} = \vec{F}(+\vec{k}) + \vec{F}(-\vec{k}) \tag{1.6}$$

Figure 1.2 shows the force exerted on an atom by two counterpropagating laser beams. For the case when the Doppler shift is small i.e. $|\vec{k}\cdot\vec{v}| \ll \gamma$, the net force is linearly proportional to the velocity and is given by

$$\vec{F}_{\text{Tot}} = -\beta\vec{v} \tag{1.7}$$

where

$$\beta = \frac{8\hbar k^2\delta(I/I_s)}{\gamma[1 + I/I_s + (2\delta/\gamma)^2]^2}. \tag{1.8}$$

The atom therefore experiences a force in the opposite direction to its velocity and is slowed down. This laser cooling enables the production of a cloud of slowly moving atoms called optical molasses (OM) [54].

1.4 Magneto optical trap

The magneto optical trap (MOT) has been the workhorse for laser cooling and atom trapping experiments since it was first demonstrated in 1987 [9, 11]. A MOT consists of a pair of so called antiHelmholtz coils having oppositely oriented currents as illustrated in Figure 1.3(a). These coils generate a magnetic field that is zero at the point midway between the coils. For distances close to this point that defines the origin, the magnetic field varies linearly according to

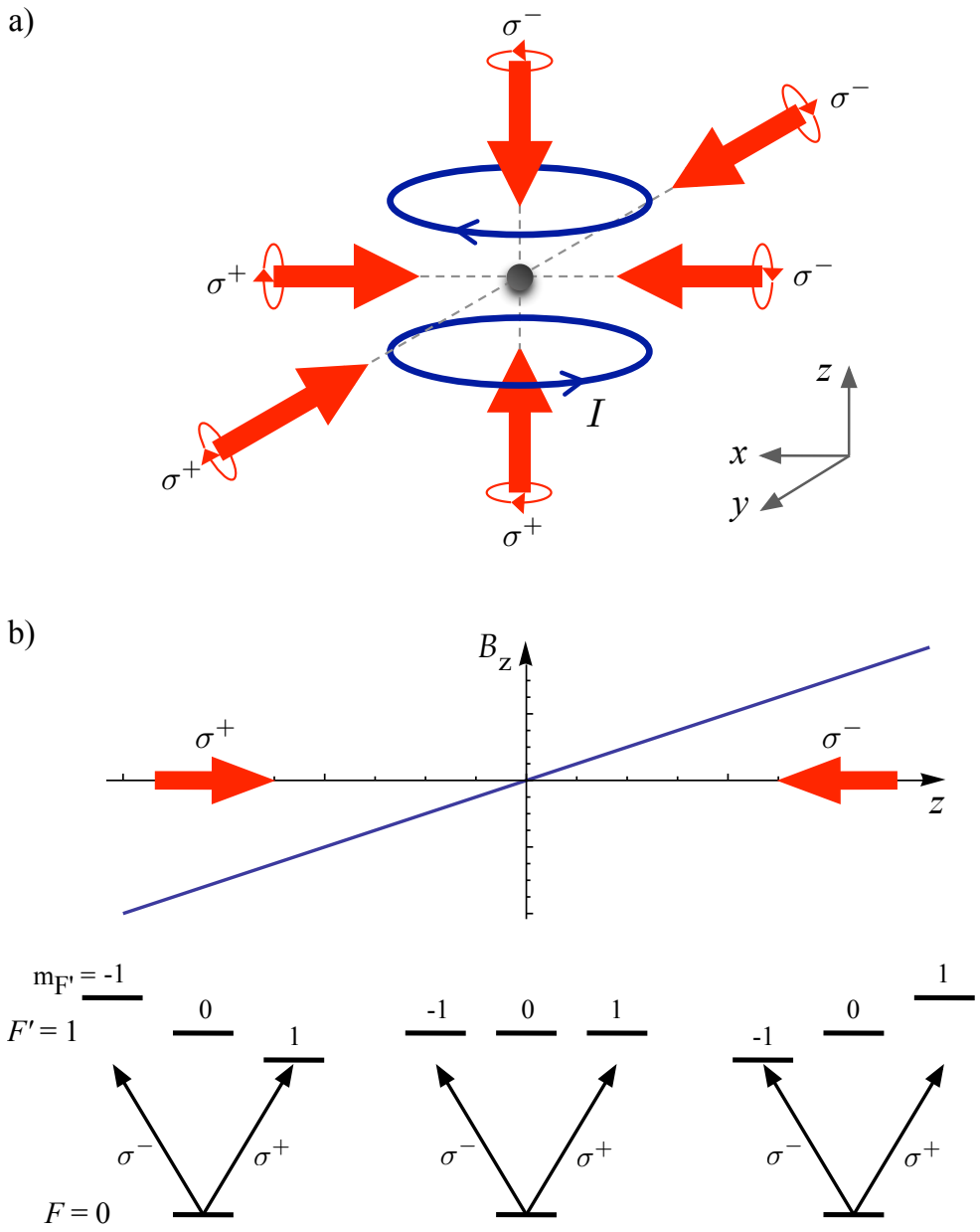

Figure 1.3: (a) Schematic of a standard 3d MOT. Thick arrows denote three pairs of counterpropagating circular polarized laser beams. The laser beams intersect at the point midway between a pair of antiHelmholtz coils. The coils carry oppositely oriented currents I and generate a quadrupole magnetic field. The black solid dot indicates the trapped atom cloud. (b) Schematic of the energies of the Zeeman sublevels along the z-axis generated by the spatially varying magnetic field. The black arrows denote possible excitation of the $F = 0$ ground state hyperfine level by the two laser beams counterpropagating along the z-axis.

$$B_z(0,0,z) = \frac{dB_z}{dz} z \tag{1.9}$$

Three pairs of counterpropagating circularly polarized laser beams pass through the coils. The spatially varying magnetic field shifts the atom state energies so that an atom primarily absorbs light if its velocity is opposite the laser beam direction. Typical field gradients are a few tens of G/cm.

The principle of a one dimensional MOT as illustrated in Figure 1.3(b), is now discussed for the case of an atom having $F = 0$ for the ground state and $F' = 1$ for the excited state. The energies of the excited $F' = 1$ level Zeeman sublevels $m_{F'}$ are given by

$$E_{m_{F'}} = g_{F'} m_{F'} \mu_B B_z(0,0,z) \tag{1.10}$$

where g_F is the Landé g factor and μ_B is the Bohr magneton. The spatially varying magnetic field along the z direction shifts the Zeeman sublevel energies as shown in Figure 1.3(b). Two circularly polarized laser beams having opposite helicities (σ^+ and σ^-) propagate along the $\pm$ z direction, respectively. Both laser beams have the same detuning below the atom's resonance frequency. To understand the MOT operation, consider an atom located at $z < 0$. The atom can only absorb light from the σ^+ laser beam propagating towards $+z$. Hence, the atom gains momentum towards the origin. Similarly, if an atom is in the region $z > 0$, it absorbs light from the σ^- laser beam propagating in the $-z$ direction, and the atom again is pushed towards the origin.

The force on an atom at location z moving with velocity $\vec{v}$ due to an oncoming laser beam propagating in the $\vec{k}$ direction with polarization σ^- is given by

$$\vec{F}_+ = \hbar \vec{k} \frac{\gamma}{2} \frac{I/I_s}{1 + I/I_s + 4/\gamma^2 \left(\delta - \vec{k} \cdot \vec{v} - g_{F'} m_{F'} \mu_B \frac{dBz}{dz} z/h\right)^2}. \tag{1.11}$$

Similarly, the force exerted by the laser beam with polarization σ^+ propagating in

the opposite direction is given by

$$\vec{F}_{-} = \hbar\vec{k}\frac{\gamma}{2}\frac{I/I_s}{1 + I/I_s + 4/\gamma^2\left(\delta + \vec{k}\cdot\vec{v} + g_{F'}m_{F'}\mu_B\frac{dBz}{dz}z/h\right)^2}. \tag{1.12}$$

The interaction of an atom with the two counterpropagating laser beams results in a total force given by

$$\vec{F}_{\text{Tot}} = \vec{F}_{+} + \vec{F}_{-}. \tag{1.13}$$

For the case where the Doppler shift and Zeeman shifts are small compared to γ, this force can be approximated by

$$\vec{F}_{\text{Tot}} = -\beta\vec{v} - \kappa\vec{z} \tag{1.14}$$

where β was defined by Equation 1.7 and

$$\kappa = \frac{g_{F'}m_{F'}\mu_B}{\hbar k}\frac{dB_z}{dz}\beta. \tag{1.15}$$

Equation 1.14 is identical to that of the damped harmonic oscillator. This explanation for the operation of a one dimensional model can be extended to describe the three dimensional MOT illustrated in Figure 1.3(a).

For the case of ^{87}Rb, there are several hyperfine levels of the lower and upper states as shown in Figure 1.1. The atoms were laser cooled using a so called trap laser that was red detuned from the D2 line cycling $F = 2 \rightarrow F' = 3$ transition. A second so called repump laser resonant with the $F = 1 \rightarrow F' = 2$ transition of the D2 line prevented the atoms from accumulating in the $F = 1$ ground state hyperfine level.

The laser cooling obviously depends strongly on the laser detuning δ. If $\delta = 0$, the atoms are heated whereas if $\delta \ll 0$, very few atoms can absorb laser photons. Optimum cooling occurs when $\delta = -\Gamma/2$ where $\Gamma = \gamma/2\pi$ [53]. Equating the cor-

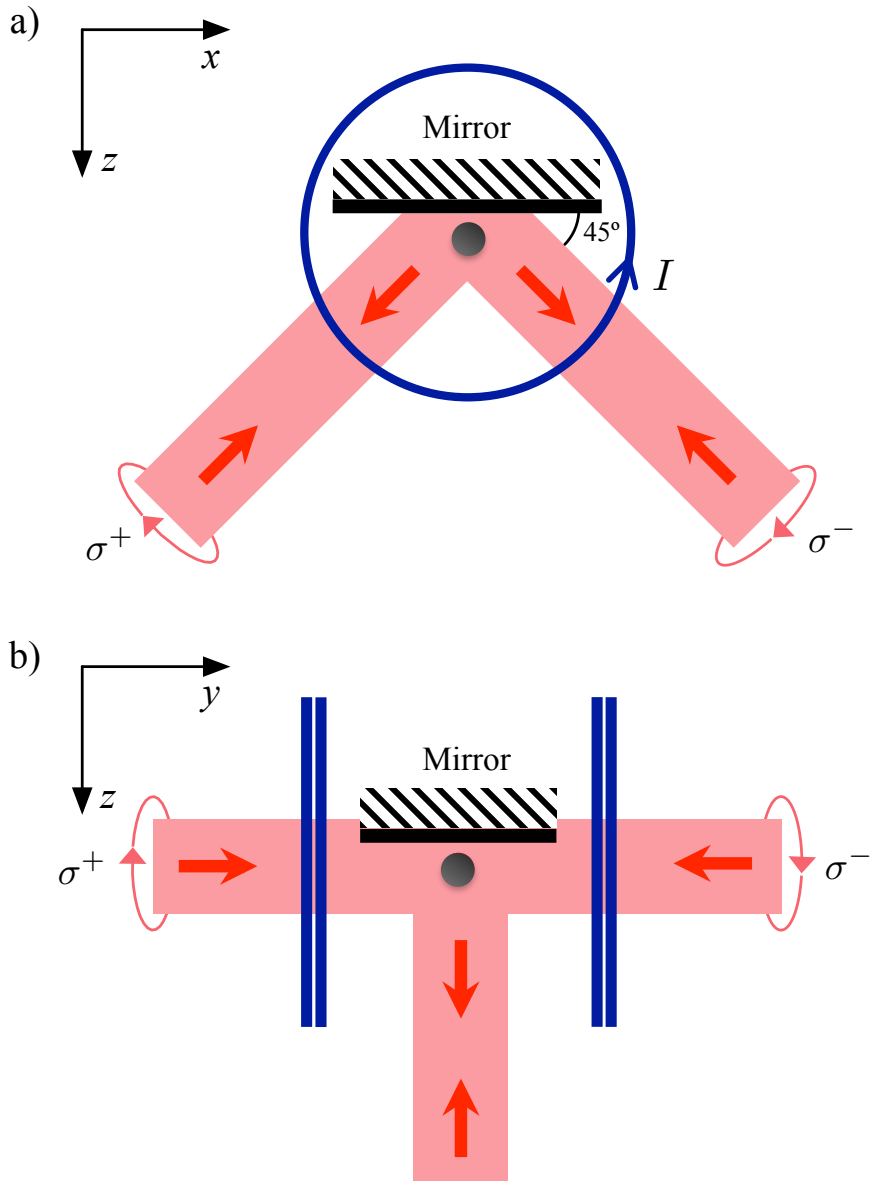

Figure 1.4: Schematic of the mirror MOT in (a) the x-z and (b) the y-z planes. The laser beams reflect off the mirror surface as indicated by the red arrows. The mirror surface is located slightly above the point midway between the two antiHelmholtz coils that have oppositely oriented currents I and are indicated in blue. The black solid dot indicates the atom cloud trapped in the MOT.

responding energy $\hbar\delta$ to $k_{\rm B}T$ where $k_{\rm B}$ is Boltzmann's constant gives the so called Doppler temperature

$$T_{\rm D} = \frac{\hbar\gamma}{2k_{\rm B}}. \tag{1.16}$$

For ^{87}Rb, $\gamma = 3.83 \times 10^7$ s^{-1} and $T_{\rm D} = 148$ μK.

The so called mirror MOT is illustrated in Figure 1.4 [34, 38]. It uses a mirror that is surrounded by one pair of coils with oppositely oriented currents to generate the quadrupole magnetic field. The mirror surface is located a few millimeters above the point midway between the coils. A total of four circularly polarized laser beams are used. Two laser beams are directed along the $\pm y$ direction while two additional beams reflect off the mirror. One advantage of the mirror MOT is that it only requires four laser beams rather than six beams for a conventional MOT. Secondly, the mirror surface can also contain microwires used to create a microtrap as will be discussed later. This work demonstrated that loading atoms into a microtrap is particularly simple if atoms are initially in a nearby mirror MOT.

1.5 Polarization gradient cooling

Temperatures below the Doppler limit $T_{\rm D}$ have been observed in optical molasses [55]. The cooling mechanism responsible for these temperatures is known as polarization gradient cooling (PGC) or Sisyphus cooling [13, 14]. It is illustrated in Figure 1.5 for an atom having ground state angular momentum $J = 1/2$ and upper state angular momentum $J' = 3/2$. The atom interacts with a standing wave generated by two laser beams travelling in the $\pm z$ directions. The two counterpropagating laser beams are linearly polarized in the x and y directions. The resulting standing wave created by the interference of the laser beams generates a spatially varying polarization as described in Figure 1.5(c).

The laser light is resonant with the transition between the upper and lower states.

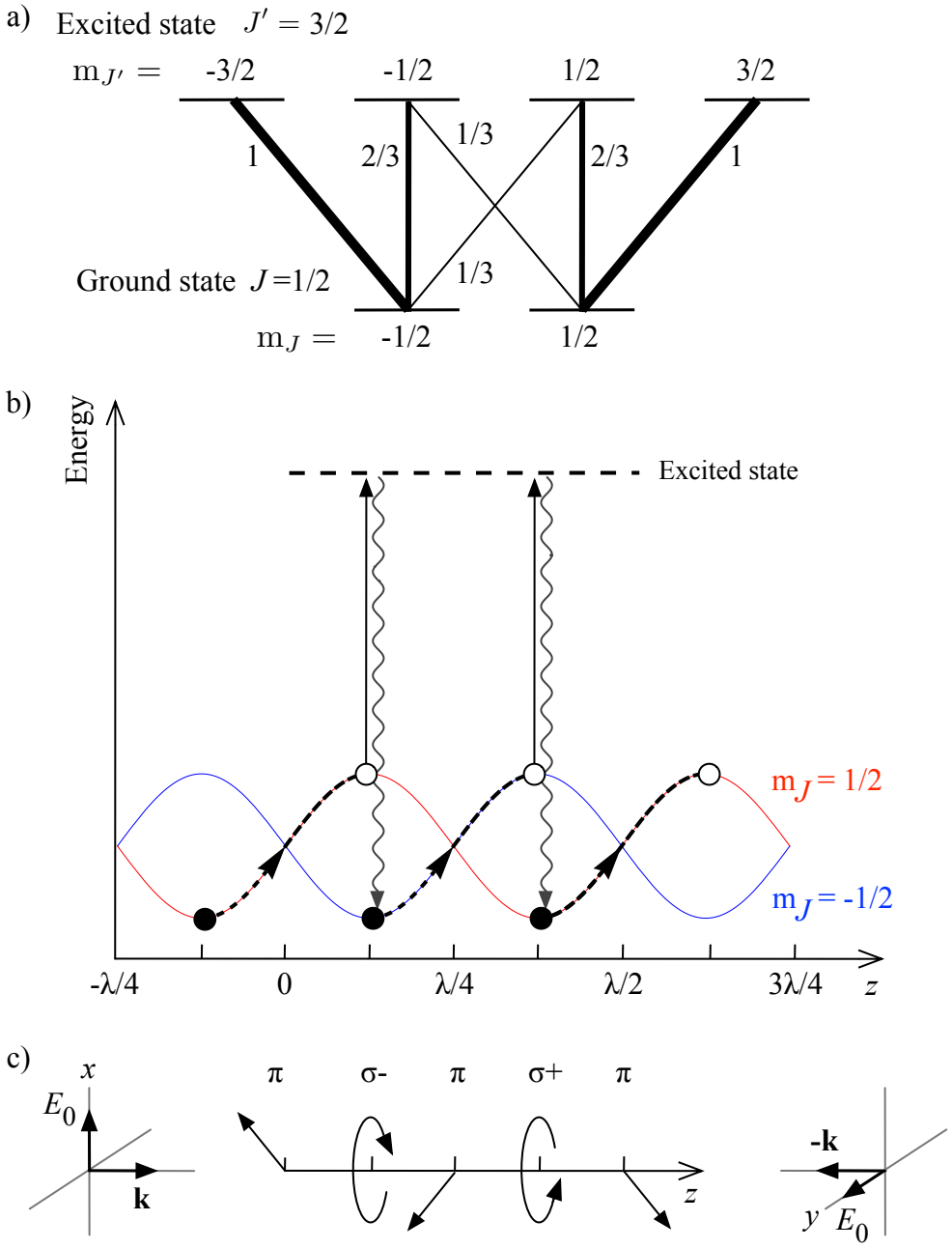

Figure 1.5: Illustration of polarization gradient cooling. (a) Relative transition probabilities between the lower state having angular momentum $J = 1/2$ and the upper state having angular momentum $J' = 3/2$. (b) Illustration of the light shifts of the two ground state Zeeman sublevels and the loss of energy of an atom travelling in the $+z$ direction as is discussed in the text. (c) Spatially dependent light polarization resulting from interference of the two counterpropagating laser beams.

The transition probability is proportional to the square of the Clebsch Gordan coefficient. The relative strengths of the transitions are given in Figure 1.5(a). For example, the probability an atom in the $m_J = -1/2$ ground state sublevel being excited to the $m_{J'} = -1/2$ excited state sublevel by linearly polarized light is 2/3 the probability the atom is excited to the $m_{J'} = -3/2$ upper state sublevel by an equal intensity of σ^- light.

The light shifts the energies of the two ground state Zeeman sublevels as shown in Figure 1.5(b) [25, 56]. For example, at $z = \lambda/8$, the σ^- light couples the $m_J = -1/2$ sublevel three times more strongly to the excited state than it does the $m_J = 1/2$ sublevel. Hence, the $m_J = -1/2$ ground state sublevel has a lower energy. To understand how an atom loses energy, consider an atom initially at $z = -\lambda/8$ in the $m_J = 1/2$ ground state sublevel moving in the $+z$ direction. The atom can only be excited by σ^+ light but it then decays back to the same sublevel. As the atom moves to $z = +\lambda/8$, the atom climbs a potential hill losing kinetic energy. It can then be excited by σ^- light. The excited state can decay to the ground state $m_J = -1/2$ sublevel which is at a lower energy. This process can be repeated cooling the atom. The minimum kinetic energy achievable using polarization gradient cooling is determined by the recoil energy acquired by an atom due to absorption of a single photon given by

$$E_{\mathrm{r}} = \frac{\hbar^2 k^2}{2M}, \tag{1.17}$$

Equating the recoil energy to $k_{\mathrm{B}}T$ gives a temperature for ^{87}Rb of less than 1 μK. In practice, temperatures of a few μK are typical due to imperfect experimental conditions affecting the laser polarization and intensity.

1.6 Magnetic traps

The interaction of an atom having a magnetic dipole $\vec{\mu}$ with a magnetic field $\vec{B}$ is given by

$$V = -\vec{\mu} \cdot \vec{B}. \tag{1.18}$$

The magnetic dipole moment is related to the atom's total angular momentum $\vec{F}$ by

$$\vec{\mu} = -g_F \mu_B \vec{F}. \tag{1.19}$$

The total angular momentum $\vec{F}$ is given by

$$\vec{F} = \vec{J} + \vec{I} \tag{1.20}$$

where $\vec{J}$ is the total electronic angular momentum which equals the sum of the orbital angular momentum $\vec{L}$ and the electron spin $\vec{S}$, and $\vec{I}$ is the nuclear spin. The Landé g-factor can be written as

$$g_F = \left[1 + \frac{J(J+1) + S(S+1) - L(L+1)}{2J(J+1)}\right] \left[\frac{F(F+1) + J(J+1) - I(I+1)}{2F(F+1)}\right]. \tag{1.21}$$

The energy shift of an atom occupying a Zeeman sublevel m_F due to the magnetic field is

$$E_{m_F} = g_F m_F \mu_B B. \tag{1.22}$$

For atoms satisfying $g_F m_F > 0$, the energy shift increases linearly with the magnetic field. Such atoms ("low-field seekers") experience a force toward the local magnetic field minima. Similarly, atoms satisfying $g_F m_F < 0$ ("high-field seekers") experience a decreasing energy as the magnetic field increases [36]. Only the low-field

seekers can be trapped using a static magnetic trap since a local magnetic field maximum cannot exist [57].

For the ^{87}Rb atoms in the $5S_{1/2}$ $F = 2$ ground state hyperfine level, only two of the Zeeman sublevels can be magnetically trapped, i.e. $m_F = +1$ and $+2$. Hence, transferring the atoms from a MOT into a magnetic trap will result in a substantial loss of atoms. This can be prevented by optically pumping the atoms into the $m_F = 2$ sublevel using circularly polarized laser light as is illustrated in Figure 1.6 [58, 59]. The optical pumping is done using a bias magnetic field of a few Gauss directed along the laser beam propagation direction to define the quantization axis. The optical pumping light is on resonance with the $F = 2 \rightarrow F' = 2$ transition of the ^{87}Rb D2 line. The σ^+ polarized laser beam excites the transitions according to $\Delta m = m'_F - m_F = +1$. The excited atoms radiatively decay back to the lower state. However, repeated excitation by circularly polarized light results in pumping all of the atoms into the $m_F = +2$ sublevel. In practice, the optical pumping laser beam is overlapped with a small amount of repump laser light to prevent atoms from accumulating in the $F = 1$ hyperfine level.

Atoms are trapped by a magnetic field arrangement that has a localized minimum. The simplest magnetic trap known as a quadrupole trap is generated using a pair of coils having oppositely oriented currents as illustrated in Figure 1.7. Typical magnetic traps use coils consisting of over 100 windings and have a radius of at least several cm [60]. Currents in excess of 10 A then generate up to a kilowatt of heat which requires the coils to be water cooled. The coils are therefore usually positioned outside the vacuum system. This in turn limits the maximum field gradient or trap depth experienced by the atoms.

The number of trapped atoms obtained using quadrupole traps is limited by the zero magnetic field at the trap center. The atomic angular momentum precesses about the magnetic field. For an atom in the ground state hyperfine level F, this so called Larmor angular frequency is given by

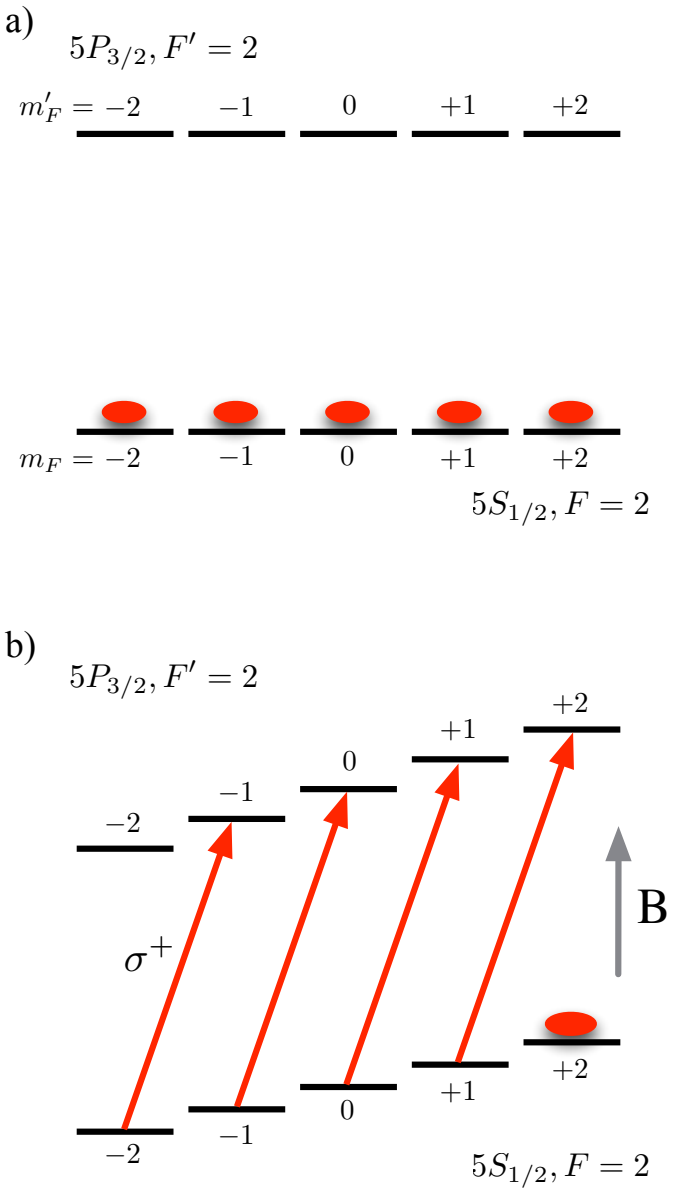

Figure 1.6: Schematic of Zeeman sublevel populations (a) before and (b) after optical pumping.

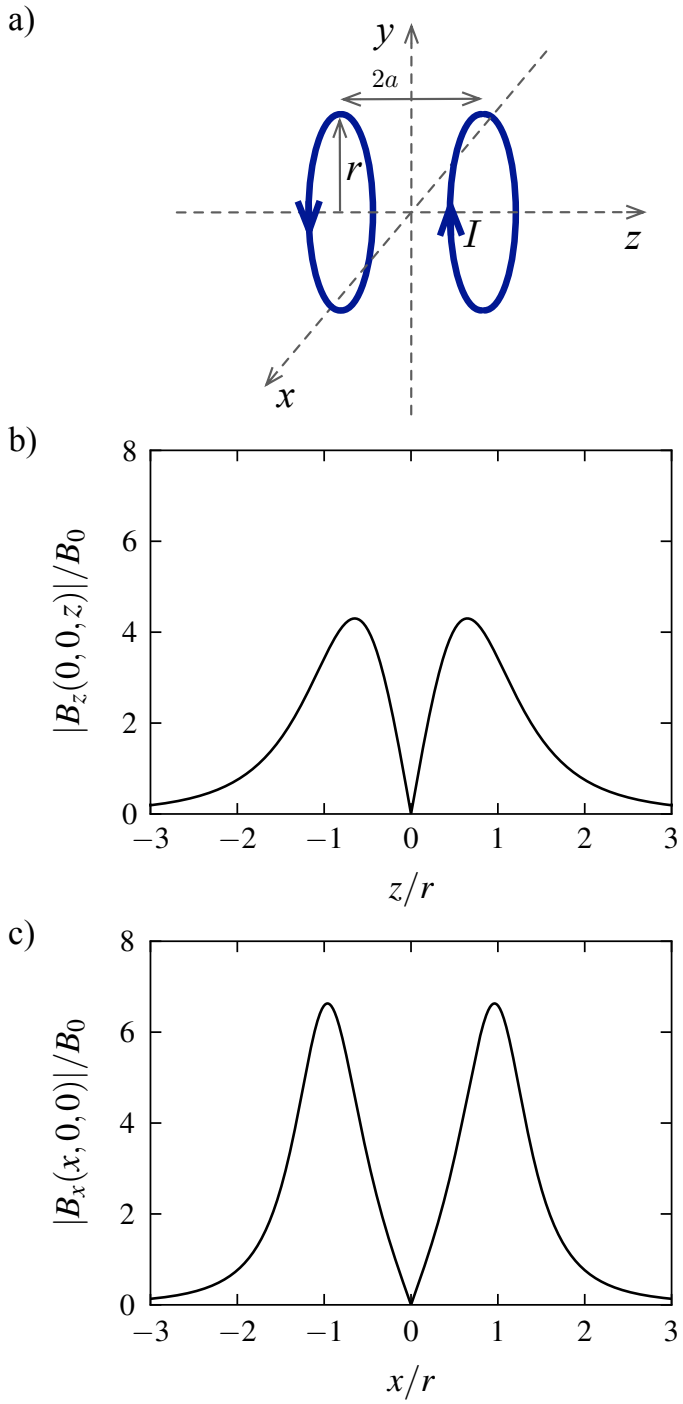

Figure 1.7: (a) Schematic of the quadrupole magnetic trap. Two coils separated by a distance $2a$ have oppositely oriented currents I. The antiHelmholtz configuration refers to the case where the coil radius equals $2a$. (b) and (c) show the magnetic fields along the z and x directions where $B_0 = \frac{\mu_0 I}{4\pi r}$.

$$\omega_L = g_F \mu_B B/\hbar. \tag{1.23}$$

The atom's spin may undergo a so called Majorana spin flip to an untrapped state if the change in Larmor frequency experienced by the atom as it moves in the trap is comparable to the Larmor frequency [61]. Spin flips do not occur if the so called adiabatic condition

$$\frac{d\omega_L}{dt} \ll \omega_L^2, \tag{1.24}$$

is satisfied [36]. A variety of traps have been demonstrated to either prevent atoms approaching the zero magnetic field using additional time dependent magnetic fields such as the TOP trap [18, 61] or adding coils to generate magnetic field configurations having nonzero minima such as the Ioffe-Pritchard trap [32] and QUIC traps [31, 60].

1.7 Magnetic microtraps

Magnetic microtraps utilize microwires as small as tens of microns to generate magnetic fields to trap atoms. This is a factor of 10,000 times smaller than the size of the macroscopic coils typically used in quadrupole traps. The magnetic field of a microwire circuit having a characteristic size d scales as $1/d$. Hence, microtraps require orders of magnitude less current to operate. Figure 1.8 shows two of the most commonly used microtraps, named the "U" and "Z" types on account of their microwire configuration. These results as well as other numerical simulations in this thesis, were computed using Mathematica. A magnetic field minimum is generated by passing a current through the microwires plus adding a uniform external bias magnetic field B_{zbias}. The "Z" trap has a finite field at the trap center which suppresses Majorana spin flips [27].

Atoms are typically loaded into microtraps from a MOT. Mirror MOTs are particularly useful for positioning the atom cloud close to the atom chip surface near the

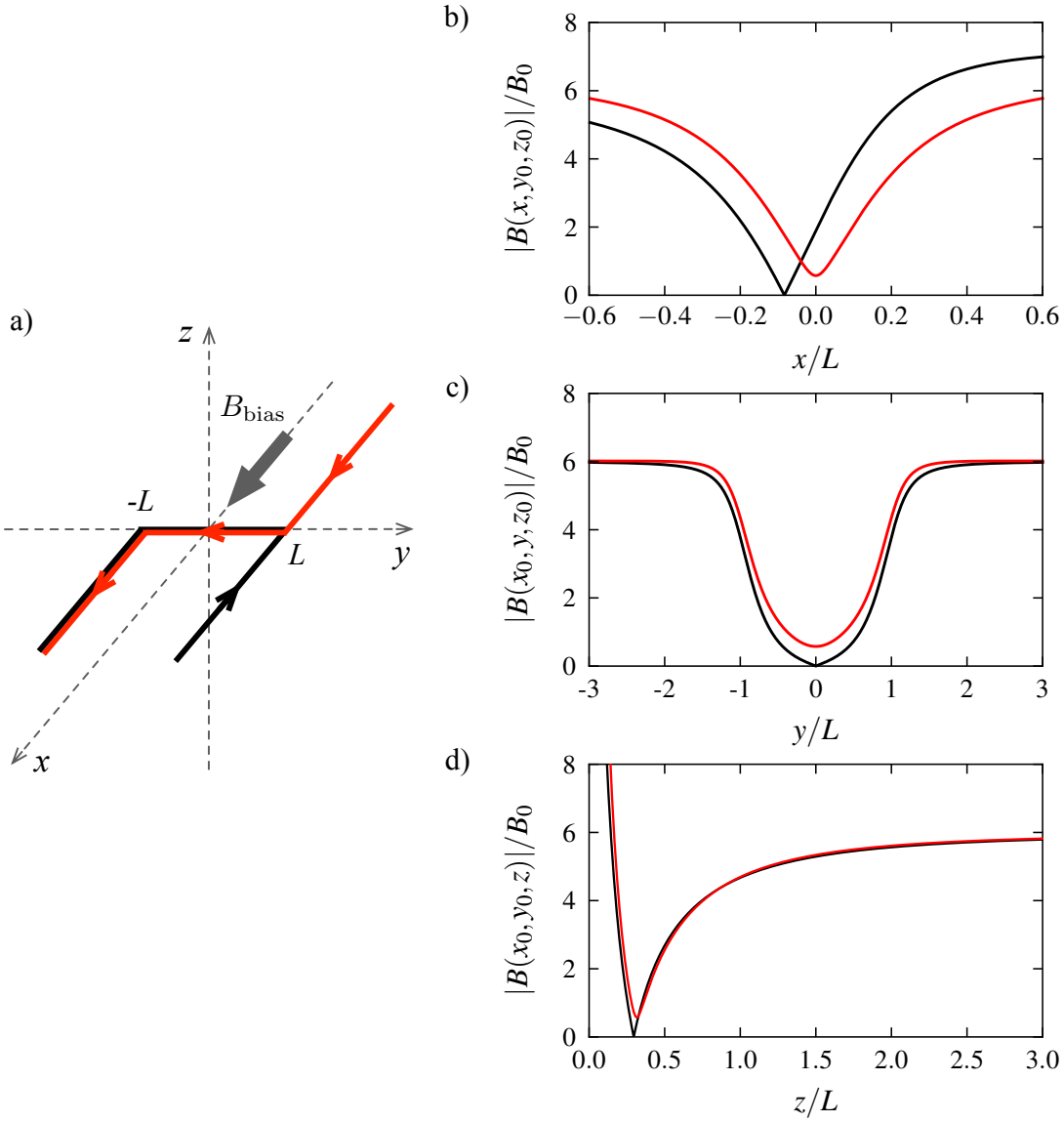

Figure 1.8: (a) Schematic of the "U" and "Z" shaped microtraps along with bias field B_{bias}. (b), (c) and (d) show the magnetic field plotted for the "U" (black) and "Z" (red) shaped microtraps along the x, y and z directions through the trap center located at (x_0, y_0, z_0) and $B_0 = \frac{\mu_0}{4\pi}\frac{I}{L}$. The field was computed using $B_{\text{bias}} = 6B_0$. The trap centers of the "U" and "Z" traps are $(-0.08, 0, 0.30)L$ and $(0, 0, 0.32)L$, respectively.

microtrap position. The atoms are then loaded into the "U" trap whose potential resembles a conventional quadrupole trap. Subsequently, the atoms can be transferred into the "Z" trap [62]. The efficiency of transferring atoms from the MOT to the "Z" trap can be as high as 80% [34].

1.8 Far off resonant optical dipole trap

Far off resonance optical dipole traps (FORT) have been widely used for trapping and manipulating cold atoms [23, 24, 25]. One application of the FORT is its capability to store and transport the cold atoms to load a secondary trap [63, 64, 65, 66]. FORTs have also been used to perform so called forced evaporative cooling [67] leading to the successful demonstration of BEC [68] and degenerate Fermi gases [69].

The optical dipole potential arises as a result of the atomic dipole moment induced by the light electric field $E(\omega)$

$$p = \alpha(\omega)E \tag{1.25}$$

where ω is the light angular frequency and $\alpha(\omega)$ is the complex polarizability. This is found by solving the damped oscillating equation of the electron using Lorentz's oscillator model of the atom [25] to be

$$\alpha(\omega) = 6\pi\epsilon_0 c^3 \frac{\gamma/\omega_0^2}{\omega_0^2 - \omega^2 - i(\omega^3/\omega_0^2)\gamma}, \tag{1.26}$$

where ϵ_0 is the electric permittivity of vacuum, ω_0 is the resonance angular frequency of the oscillator and γ was defined in Equation 1.3. The interaction between the induced atomic dipole moment and the light field is given by

$$\begin{aligned} U_{\text{dip}} &= -\frac{1}{2}\langle \vec{p} \cdot \vec{E} \rangle \\ &= -\frac{1}{2\epsilon_0 c}\text{Re}(\alpha) I \end{aligned} \tag{1.27}$$

where the angular brackets indicate the time average over the rapid oscillating terms. The light intensity is defined by

$$I = 2\epsilon_0 c |E|^2. \tag{1.28}$$

The atoms scatter light at a rate given by

$$\begin{aligned} \Gamma_{\text{sc}} &= \frac{1}{\hbar\omega}\langle \frac{d\vec{p}}{dt} \cdot \vec{E} \rangle \\ &= \frac{1}{\hbar\epsilon_0 c}\text{Im}(\alpha) I. \end{aligned} \tag{1.29}$$

For the case where the magnitude of the laser detuning from the atomic resonance is much less than the resonant frequency i.e. $|\delta| = |\omega - \omega_0| \ll \omega_0$, the potential and scattering rate are given as follows.

$$U_{\text{dip}}(\vec{r}) = \frac{3\pi c^2}{2\omega_0^3}\frac{\gamma}{\delta} I(\vec{r}), \tag{1.30}$$

and

$$\Gamma_{\text{sc}}(\vec{r}) = \frac{3\pi c^2}{2\hbar\omega_0^3}\left(\frac{\gamma}{\delta}\right)^2 I(\vec{r}). \tag{1.31}$$

For the case of a red detuned laser i.e. $\delta < 0$, $U_{\text{dip}} < 0$ and the atoms are attracted to the region of maximum light intensity. Similarly, when $\delta > 0$, atoms are repelled from intensity maxima. The largest potential depth is achieved at small detunings. However, the scattering rate increases sharply as $\frac{1}{\delta^2}$ which can heat the trapped atoms.

For ^{87}Rb, the D1 and D2 lines consist of multiple transitions between the ground and excited state hyperfine levels. The excited state hyperfine intervals are more than

an order of magnitude smaller than the ground state hyperfine splitting. Hence, the optical dipole potential experienced by a ^{87}Rb in the ground state hyperfine level F can be expressed as a sum of two terms [25]

$$U_{\rm dip}(\vec{r}) = \frac{\pi c^2 \gamma}{2\omega_0^3}\left(\frac{2+\mathcal{P}g_F m_F}{\delta_2} + \frac{1-\mathcal{P}g_F m_F}{\delta_1}\right) I(\vec{r}). \tag{1.32}$$

where δ_1 and δ_2 are the detunings of the laser from the D1 and D2 transitions respectively. The light polarization is described by $\mathcal{P}$ which equals 0 for linear and ± 1 for $\sigma^{\pm}$ polarized light, respectively.

The typical arrangement to generate a FORT is to focus an infrared laser beam as shown in Figure 1.9. The atoms are then trapped at the laser focus. For a Gaussian shaped laser beam, the laser intensity is given by [70, 71]

$$I(r,z) = \frac{2P}{\pi \mathrm{w}^2(z)} \exp\left[-2\frac{r^2}{\mathrm{w}^2(z)}\right], \tag{1.33}$$

where P is the laser power and the beam radius along the laser propagation direction z is given by

$$\mathrm{w}(z) = \mathrm{w}_0\sqrt{1+(z/z_R)^2} \tag{1.34}$$

w_0 is the minimum beam radius and z_R is the Rayleigh length

$$z_R = \pi \mathrm{w}_0^2/\lambda \tag{1.35}$$

for light at a wavelength λ. The trap potential near the laser focal spot can be approximated by

$$U_{\rm dip}(r,z) = -U_0 + \frac{1}{2}M\omega_r^2 r^2 + \frac{1}{2}M\omega_z^2 z^2. \tag{1.36}$$

The trap depth U_0 is given by

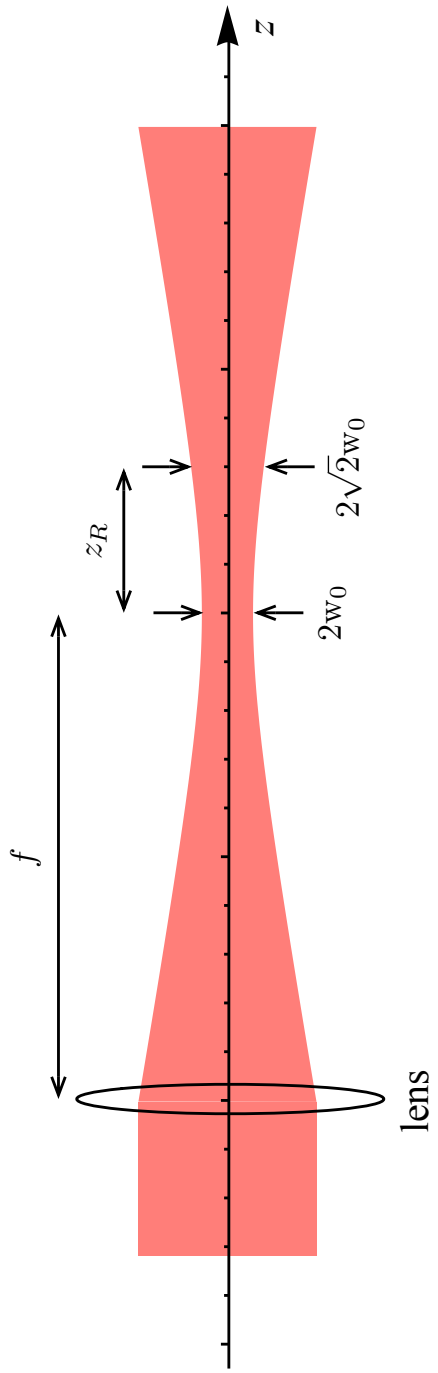

Figure 1.9: Schematic of a Gaussian laser beam propagating in the z direction.

$$U_0 = \left| \frac{\pi c^2 \gamma}{2\omega_0^3} \frac{2P}{\pi \mathrm{w}_0^2} \left(\frac{2 + \mathcal{P} g_F m_F}{\delta_2} + \frac{1 - \mathcal{P} g_F m_F}{\delta_1} \right) \right| \tag{1.37}$$

and the radial and axial trap angular frequencies are defined as follows

$$\omega_r = \sqrt{4U_0/M\mathrm{w}_0^2}, \tag{1.38}$$

$$\omega_z = \sqrt{2U_0/Mz_R^2}. \tag{1.39}$$

Many FORTs have been generated using infrared lasers operating at 1064 nm which produce tens of watts of power and are relatively inexpensive. The trap depth for ^{87}Rb atoms created by focussing such a linearly polarized laser beam is

$$U_0(\mu\mathrm{K}) = 8.92 \times 10^4 \frac{P(\mathrm{W})}{\mathrm{w}_0(\mu\mathrm{m})^2}. \tag{1.40}$$

A 20 W laser beam focussed to a 35 μm beam waist radius gives a trap depth of 1.5 mK. The corresponding photon scattered rate $\Gamma_{sc} = 10$ s^{-1} and the trap angular frequencies are $\omega_r = 2\pi \times 3.4$ kHz and $\omega_z = 2\pi \times 23$ Hz. Alternatively, ^{87}Rb atoms can be trapped in a FORT using a lower power beam if the detuning is smaller. For example, our group has created a FORT to trap ^{87}Rb atoms using a 100 mW laser operating at 852 nm focussed to a beam waist radius of 20 μm [72]. However, such a FORT experiences a much larger photon scattering rate that limits the temperature of the trapped atoms.

2 Double-loop microtrap array

This chapter describes the principle of the double-loop microtrap array starting from a single double-loop microtrap [48, 73, 74].

2.1 Double-loop microtrap

A schematic diagram of a single double-loop microtrap is shown in Figure 2.1. The microtrap is generated by oppositely oriented currents flowing in two concentric circular wire loops located in the x-y plane having radii r_1 and $r_2 = \alpha r_1$ (α>1) as well as an external bias field B_{zbias} in the direction perpendicular to the x-y plane. For convenience, we first consider the case without B_{zbias}. The magnetic field along the z-axis generated by infinitely thin wires comprising the double-loop is given by

$$\vec{B}(0,0,z) = 2\pi r_1 B_0 \left[\frac{\alpha^2 r_1^2}{(\alpha^2 r_1^2 + z^2)^{3/2}} - \frac{r_1^2}{(r_1^2 + z^2)^{3/2}} \right] \hat{\mathbf{z}}, \tag{2.1}$$

where $\hat{\mathbf{z}}$ is the unit vector along the z-axis and

$$B_0 = \frac{\mu_0 I}{4\pi r_1}, \tag{2.2}$$

where μ_0 is the permeability of free space. The magnetic field is zero at position

$$z_0 = \frac{\alpha^{2/3}}{\sqrt{1+\alpha^{2/3}}}\, r_1. \tag{2.3}$$

The interaction of an atom having a magnetic dipole $\vec{\mu}$ with a magnetic field $\vec{B}$ was described in Section 1.6. Atoms trapped in a magnetic trap experience a force

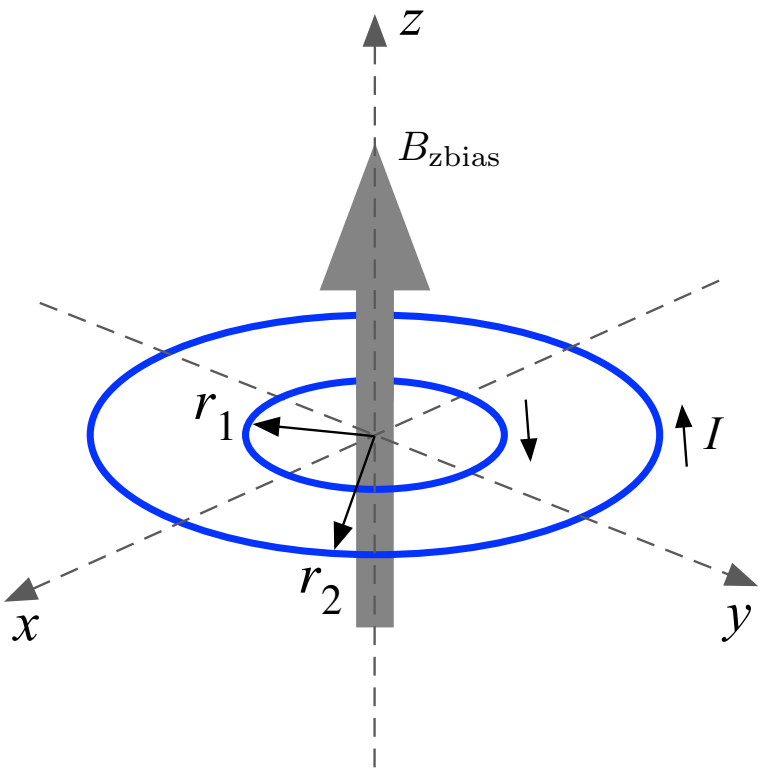

Figure 2.1: Schematic of a single double-loop wire pattern for generating a microtrap showing oppositely oriented currents I and a bias field B_{zbias}.

toward the location where the magnetic field has a minimum magnitude.

$$\vec{\mathcal{F}} = \nabla(\vec{\mu} \cdot \vec{B}) = g_F m_F \mu_B \left(\hat{\rho} \frac{\partial B}{\partial \rho} + \hat{\mathbf{z}} \frac{\partial B}{\partial z} \right) \tag{2.4}$$

The two terms on the right side of this equation give the force along the radial ρ and axial z directions. For points on the z-axis, the radial force is zero due to the loop symmetry and the atoms experience a force proportional to $\frac{dB_z}{dz}$ given by

$$\frac{dB_z}{dz}(0,0,z_0) = 6\pi \left[\frac{(\alpha^{2/3}-1)(\alpha^{2/3}+1)^3}{\alpha^{2/3}(\alpha^{4/3}+\alpha^{2/3}+1)^{5/2}} \right] \frac{B_0}{r_1}. \tag{2.5}$$

The field gradient given by Equation 2.5 is plotted as a function of α in Figure 2.2. The maximum value, occurring when $\alpha = 2.195$, is

$$\frac{dB_z}{dz}(0,0,z_0)_{\max} = 2.068 \frac{B_0}{r_1}. \tag{2.6}$$

For atoms to be trapped, the magnetic field gradient force must be much larger than the gravitational force.

$$g_F m_F \mu_B \frac{dB_z}{dz} \gg Mg, \tag{2.7}$$

The field gradient on the left side of this equation is evaluated at the trap center. g is the gravitational acceleration. Using Equation 2.6 and the definition of B_0 given by Equation 2.2 the requirement for a trap is that

$$\frac{I(\mathrm{A})}{r_1(\mathrm{meter})^2} \gg 0.85 \frac{M(\mathrm{amu})}{g_F m_F}, \tag{2.8}$$

where amu denotes atomic mass number. For a macroscopic coil ($r_1 \geq 1$ cm) the current satisfying Equation 2.8 must exceed hundreds of amps to trap the heavy alkali atoms as is shown in Table 2.1 for the case when the magnetic trapping force is ten times larger than the gravitational force. Hence, macroscopic magnetic traps require coils having a large number of turns. For the case shown in Figure 2.1 of a trap generated by a single double-loop, such currents are not practical because

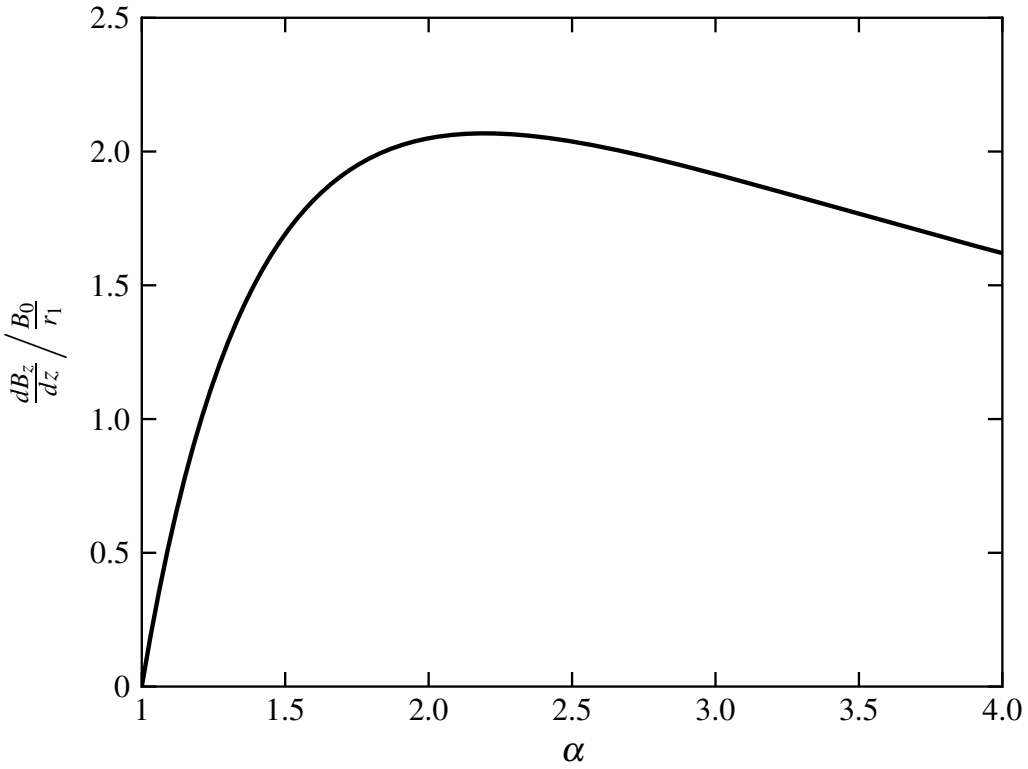

Figure 2.2: Plot of $\frac{dB_z}{dz}$ evaluated at the trap center (0, 0, z_0) as a function of α.

Table 2.1: Magnetic field gradient required to trap the stable alkali atom isotopes. The field gradient was found such that the magnetic trapping force exceeds the gravitational force by a factor of 10 as is discussed in the text.

Atom	Abundance	I	F	$\frac{dB_z}{dz}$ (G/cm)
^{6}Li	7.5%	1	1/2	32
			3/2	11
^{7}Li	92.5%	3/2	1	25
			2	12
^{23}Na	100%	3/2	1	81
			2	40
^{39}K	93.3%	3/2	1	137
			2	68
^{40}K	0.01%	4	7/2	90
			9/2	70
^{41}K	6.7%	3/2	1	144
			2	72
^{85}Rb	72.2%	5/2	2	223
			3	149
^{87}Rb	27.8%	3/2	1	305
			2	153
^{133}Cs	100%	7/2	3	311
			4	233

resistive heating would destroy the thin microwires. However, the required currents are reduced by orders of magnitude if the loop size is suitably small. For the case of an inner loop radius $r_1 = 300$ μm, alkali atoms can be trapped using currents of only about 1 A. Considering the copper microwire having a length of 2 cm and a cross section of 50 μm $\times$ 10 μm at the center of an atom chip, the microwire resistance is about 1 Ω. A current of 2 A then generates a resistive power of 4 W. This heat can be readily dissipated by mounting the atom chip on a copper heat sink.

2.2 Magnetic field of microtrap

The magnetic field generated at an arbitrary point above the x-y plane is given by

$$\vec{B} = B_z(\rho, z)\hat{\mathbf{z}} + B_\rho(\rho, z)\hat{\rho}. \tag{2.9}$$

The azimuthal field component B_ϕ is 0 because of the cylindrical symmetry of the trap about the z-axis. The axial and radial field components generated by a single loop of radius R is given by [27]

$$B_z(\rho, z) = \frac{\mu_0 I}{2\pi} \frac{1}{\sqrt{(R+\rho)^2 + z^2}} \left[K(k^2) + \frac{R^2 - \rho^2 - z^2}{(R-\rho)^2 + z^2} E(k^2) \right], \tag{2.10}$$

$$B_\rho(\rho, z) = \frac{\mu_0 I}{2\pi\rho} \frac{z}{\sqrt{(R+\rho)^2 + z^2}} \left[-K(k^2) + \frac{R^2 + \rho^2 + z^2}{(R-\rho)^2 + z^2} E(k^2) \right], \tag{2.11}$$

where

$$k^2 = \frac{4R\rho}{(R+\rho)^2 + z^2}. \tag{2.12}$$

K and E are the complete elliptic integrals defined as

$$K(x) = \int_0^1 \frac{dt}{\sqrt{(1-t^2)(1-x^2t^2)}}, \tag{2.13}$$

$$E(x) = \int_0^1 \frac{\sqrt{1-x^2t^2}}{\sqrt{1-t^2}} dt. \tag{2.14}$$

Figure 2.3 shows the magnetic field magnitude along the axial and radial directions. It increases approximately linearly near the trap center where the field is zero, resulting in a trap that tightly confines the atoms. Figure 2.3(a) shows the maximum magnetic field occurs when $z = 0$. The field then decreases until z_0 and increases to a maximum value of $0.61B_0$ at $z = 1.83r_1$. Figure 2.3(b) shows the radial dependence of the magnetic field magnitude has a maximum of $1.82B_0$ that occurs when $\rho = 1.74r_1$. The increase of the field along the radial direction is half that along the axial direction because $\nabla \cdot \vec{B} = 0$. The trap depth is determined by the smaller of the maxima surrounding the point where the magnetic field is zero. Figure 2.4 shows plots of the magnetic field magnitude in the y-z plane at $x = 0$ and in the x-y plane at $z = z_0$. For the case of trapping ^{87}Rb atoms in the $5S_{1/2}$ $|F = 2, m_F = 2\rangle$ level for a microtrap having $r_1 = 300$ μm and $I = 1$ A, the trap depth is 1.70×10^{-27} Joules. Dividing this by Boltzmann's constant, gives a corresponding temperature of 123 μK.

2.3 Effect of B_{zbias}

The trap can be made approximately symmetric along the z-axis by applying a bias field along the z-direction, B_{zbias}, as is shown in Figure 2.3. The bias field decreases the magnetic field magnitude maximum at $z = 0$ and increases the maximum at $z = 1.83r_1$. This significantly increases the trap depth as is shown in Figure 2.5. The maximum trap depth occurs when $B_z = 1.43B_0$ which was used when calculating the magnetic field plotted in Figure 2.3. At higher values of the bias field, magnetic field maximum at $z = 0$ is smaller than the maximum at $z = 1.83r_1$ resulting in a decrease in the trap depth as shown in Figure 2.5. For the case of trapping ^{87}Rb atoms in the $|2, 2\rangle$ ground state Zeeman sublevel when $r_1 = 300$ μm and $I = 1$ A, the maximum trap depth is 407 μK. Increasing the chip current to 2.5 A, results in

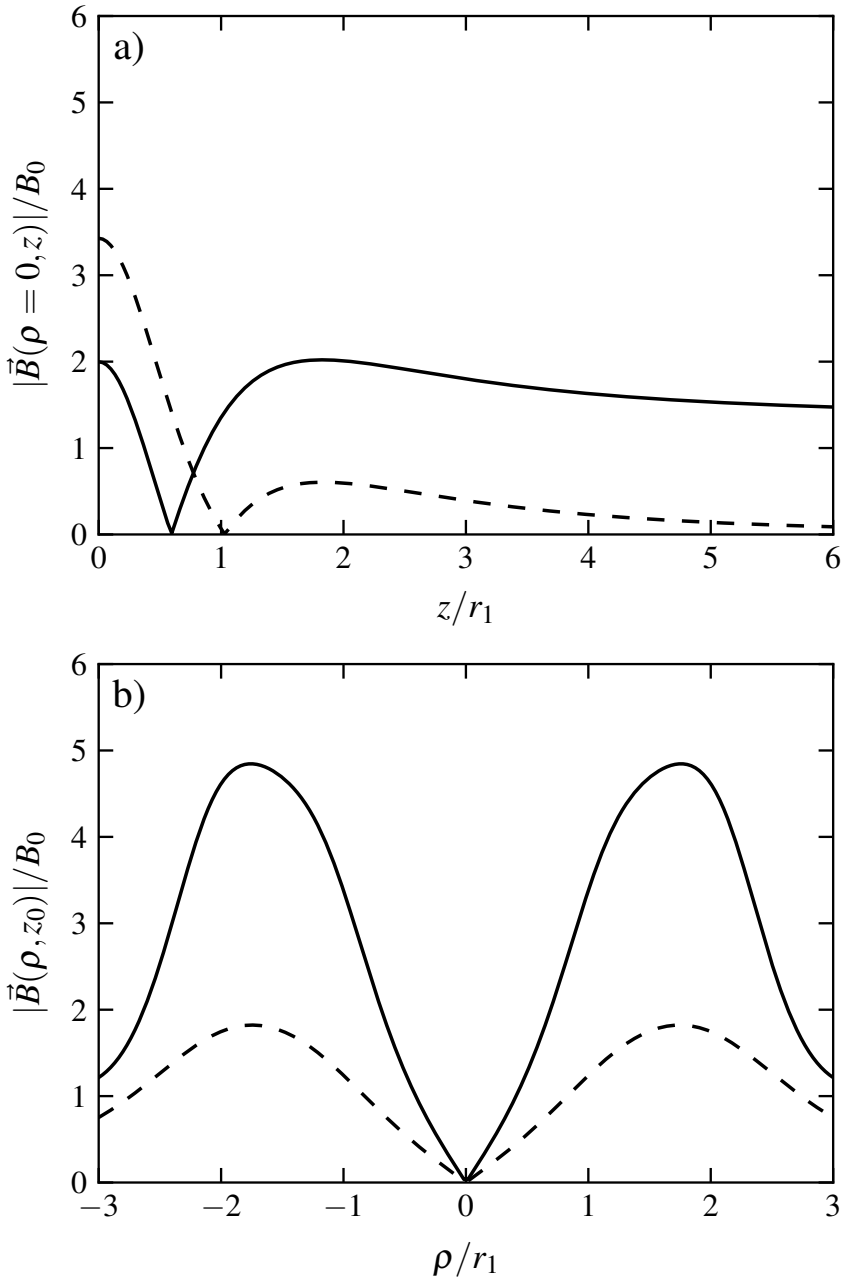

Figure 2.3: Magnetic field generated by a double-loop (a) along the z-axis and (b) in the radial direction through the trap center. The origin of the coordinate system is at the center of the double-loop as is illustrated in Figure 2.1. The field minimum is at $z_0 = 1.03r_1$ when there is no bias field (dashed curve) and at $z_0 = 0.59r_1$ for a bias field of $B_{\text{zbias}} = 1.43B_0$ (solid curve). Each curve in (b) is evaluated at its respective value of z_0.

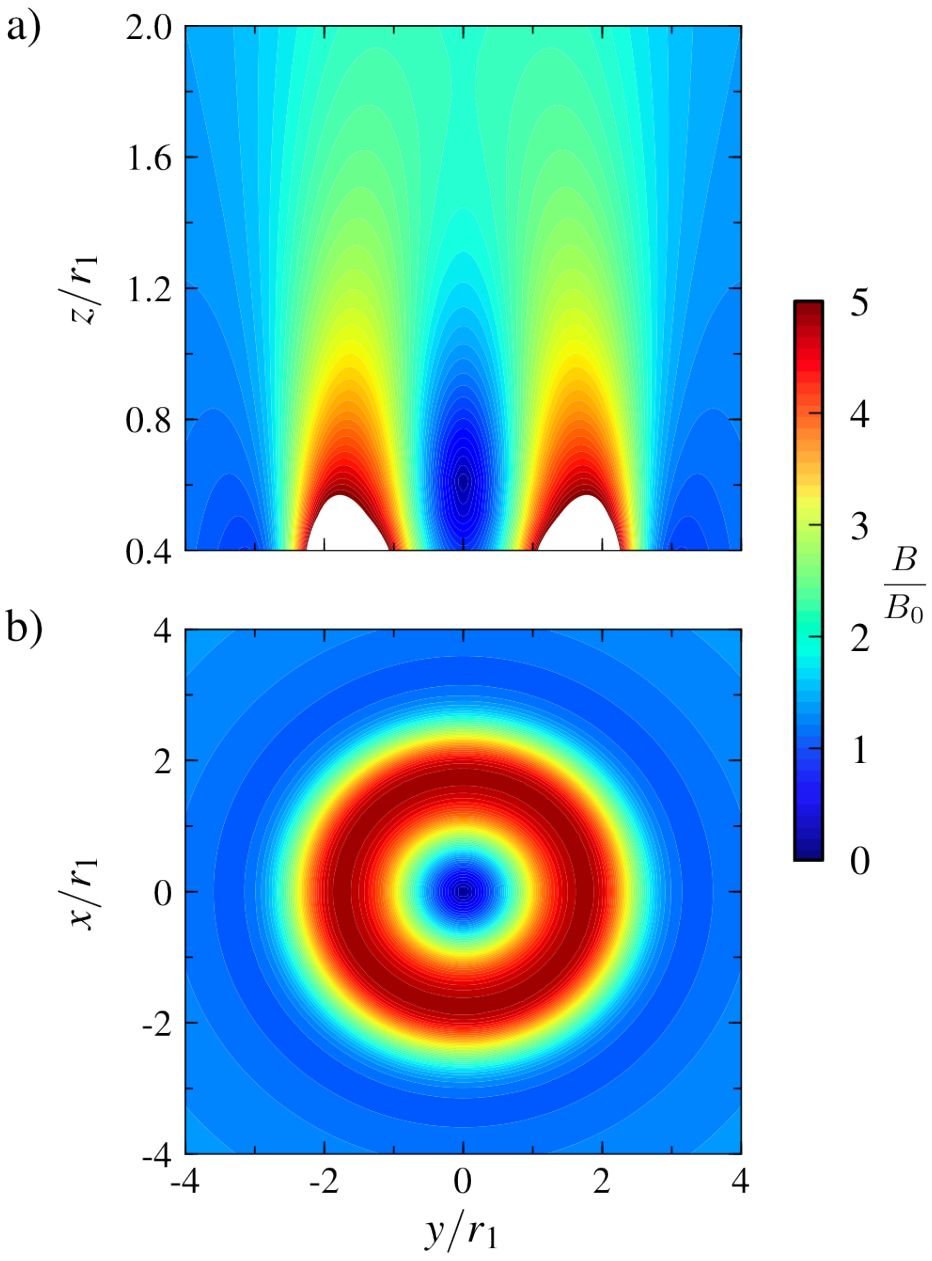

Figure 2.4: Magnetic field magnitude divided by B_0 generated by a single double-loop microtrap and a bias field $B_{\text{zbias}} = 1.43B_0$ in (a) the y-z plane at $x = 0$ and (b) x-y plane at $z = z_0$. The magnetic field becomes very large close to the wires which is indicated by the white color.

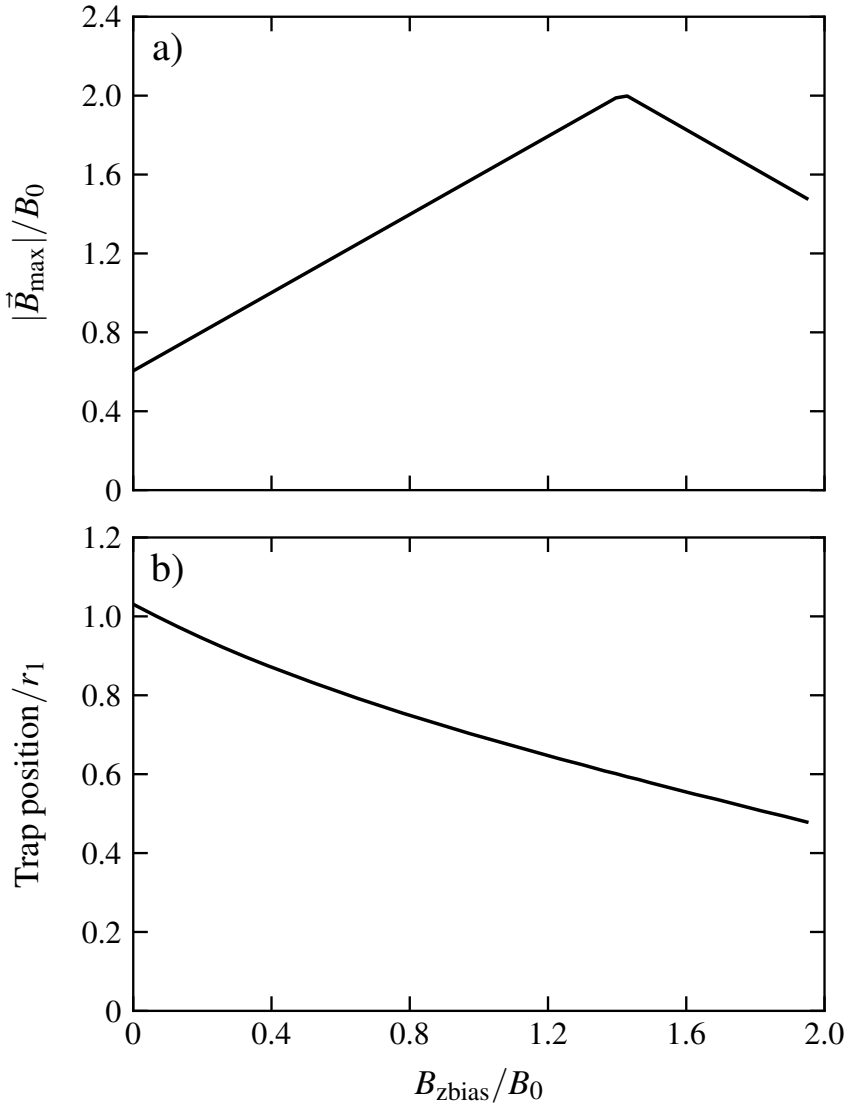

Figure 2.5: Effect of the bias field on (a) the magnetic field magnitude that determines the trap depth and (b) the microtrap position above the double-loop located in the x-y plane. See text for additional details.

a trap depth exceeding 1 mK which is comparable to temperatures achieved using a standard MOT. This is important as it facilitates loading the microtrap from atoms initially prepared in a MOT.

The bias field also shifts the trap position toward the x-y plane as is shown in Figure 2.3(a). This distance between the trap position and the x-y plane as a function of B_{zbias} is plotted in Figure 2.5(b). This is important as it gives the experimentalist the ability to control the distance of the ultracold atoms from the atom chip. This is of interest for studying surface interactions such as the Casimer Polder force [75, 76].

2.4 Linear array of double-loop microtraps

A one or two dimensional array of microtraps can be generated by linking individual double-loop microtraps. An example of a linear array is illustrated in Figure 2.6. It shows three microtraps aligned along the y-axis that are separated by a distance of $5r_1$. The double-loops are linked so that the current in the outer loops of adjacent traps flows in the same direction and opposite to that in the inner loops. This has the advantage of requiring only one power supply to generate the current for the entire microtrap array. Figure 2.6(b) and (c) show the plots of the magnetic field magnitude in the y-z and x-y planes through the center of the middle microtrap. The magnetic field from the connecting wire segments is not considered here. The trap was created with a bias field $B_{\text{zbias}} = 1.43B_0$. The location of the trap minima are readily apparent. Figure 2.7 shows the magnetic field magnitude along the x, y and z directions for linear arrays consisting of a single, three and five microtraps. Neighbouring microtraps are separated by a distance of $5r_1$. Each microtrap experiences negligible perturbation due to neighbouring microtraps particularly near the trap center.

An actual array of double-loop microtraps requires straight wire segments connecting neighbouring microtraps as shown in Figure 2.8. The question arises how these straight wire currents and incomplete circular loops perturb the microtrap. A comparison of the magnetic field generated by an ideal double-loop microtrap with

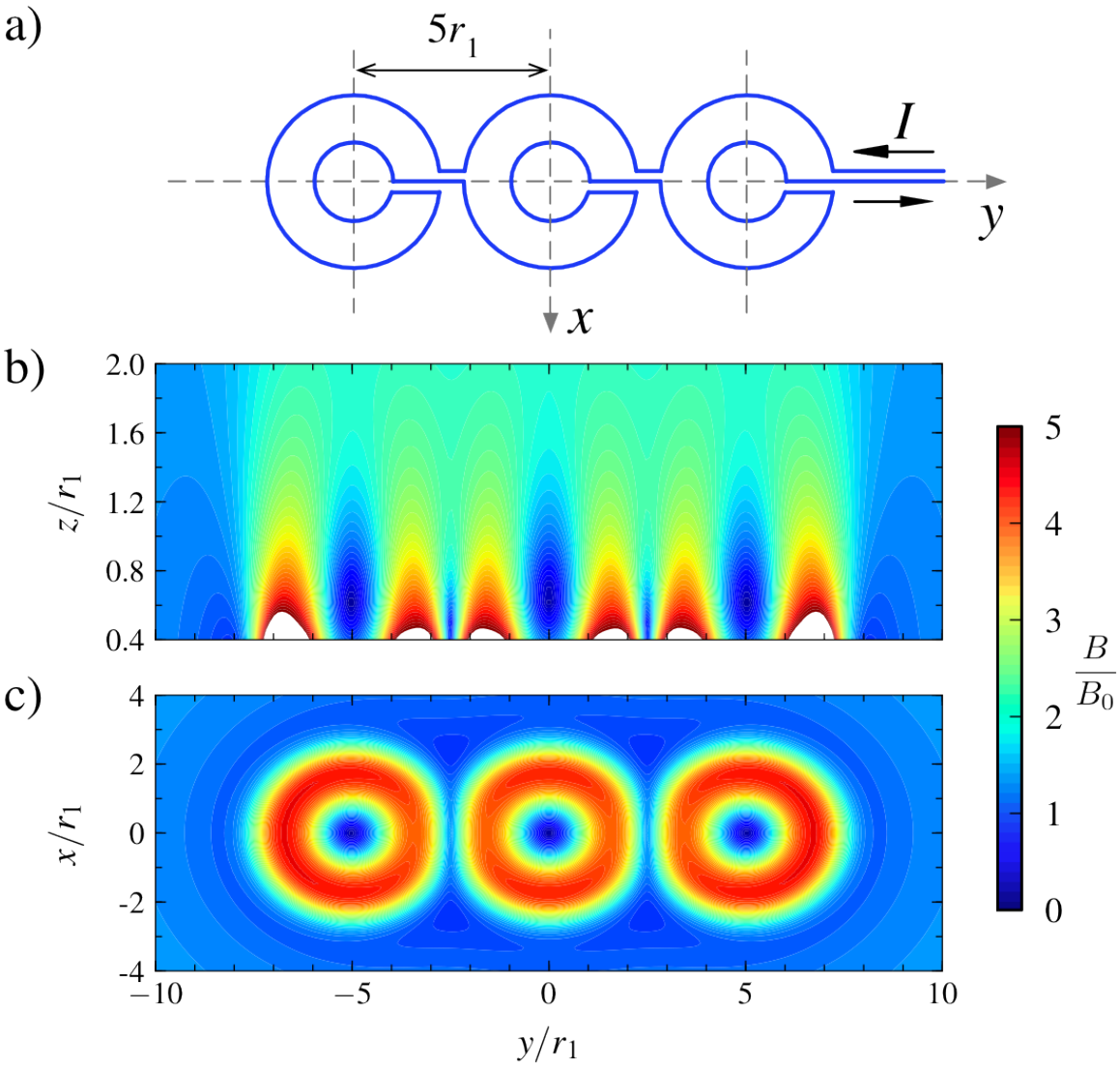

Figure 2.6: (a) Schematic layout of a linear array of three microtraps. The magnetic field was computed for the case of the current distribution shown in (a) combined with a bias field of $B_{\text{zbias}} = 1.43B_0$. The magnitude of the total magnetic field divided by B_0 is shown in (b) for the y-z plane at $x = 0$ and (c) for the x-y plane at $z = 0.646r_1$, the veritcal position of the middle microtrap. The magnetic field becomes very large close to the wires which is indicated by the white color.

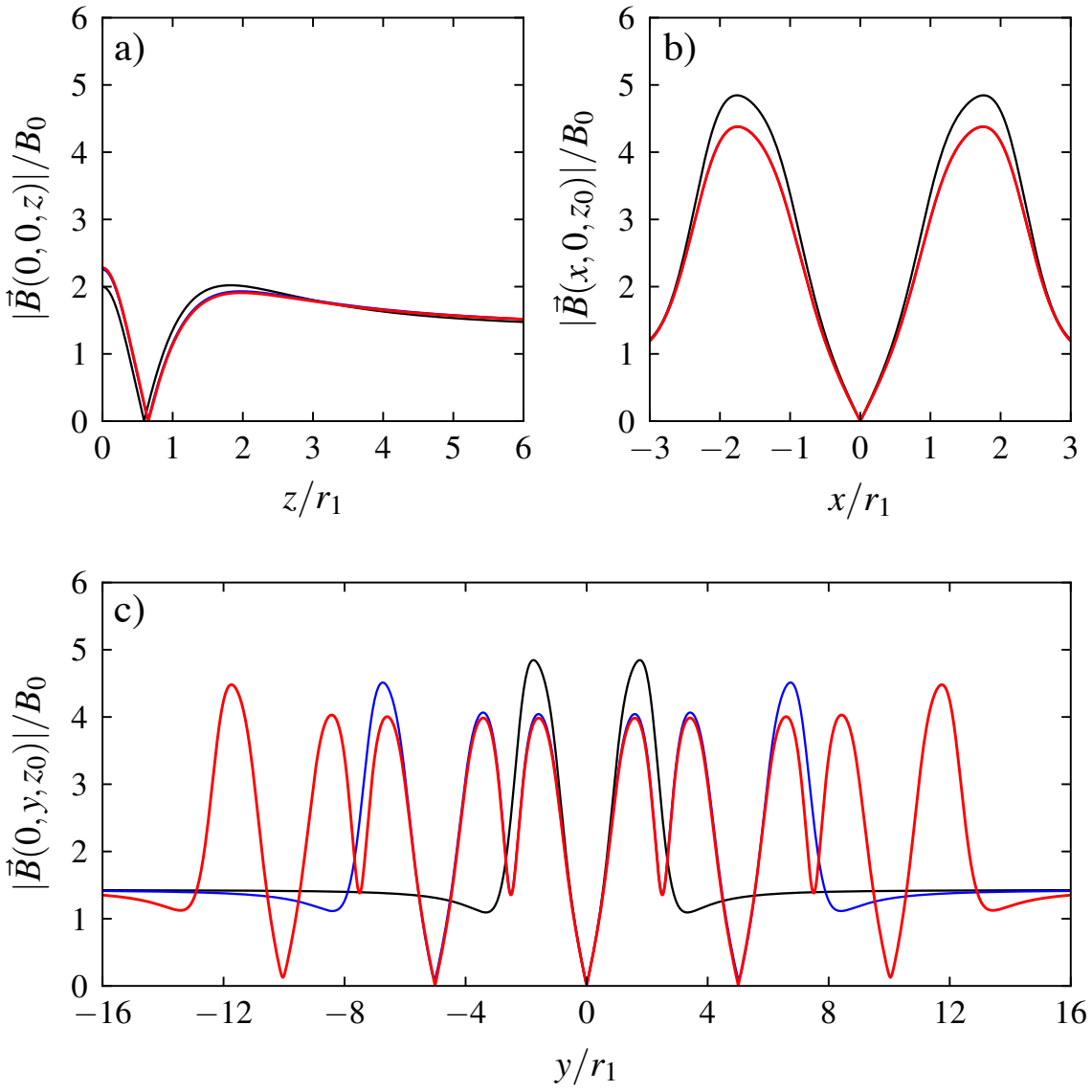

Figure 2.7: Effect of the side microtraps on the magnetic field of the middle microtrap in a linear array consisting of a single (black), three (blue) and five (red) microtraps. The magnetic field was found using a bias field of $B_{\text{zbias}} = 1.43B_0$. The magnitude of the total magnetic field divided by B_0 is given in (a) along the z-axis. The position of the middle microtrap in the vertical direction is at $z_0 = 0.593r_1$, $0.646r_1$ and $0.653r_1$ for the cases of an array consisting of a single, three and five microtraps, respectively. (b) shows the magnetic field along the x-direction when $y = 0$ and $z = z_0$ and (c) along the y-direction when $x = 0$ and $z = z_0$. The blue and red lines are overlapped in (a) and (b).

$r_1 = 300$ μm and that by the wire configuration shown in Figure 2.8 is given in Figure 2.9. Figure 2.8 shows the actual design of a single microtrap in the linear array of the microtraps. The magnetic field of the incomplete circular loops in the double loops was approximated by overlapping straight wire segments over the broken arcs carrying oppositely directed current. Neither the trap position nor the trap depth changed. The only discernible difference was found for the magnetic field along the y direction at ± 0.5 mm. This is not surprising because that is where the straight connecting wire segments and the broken arcs are located.

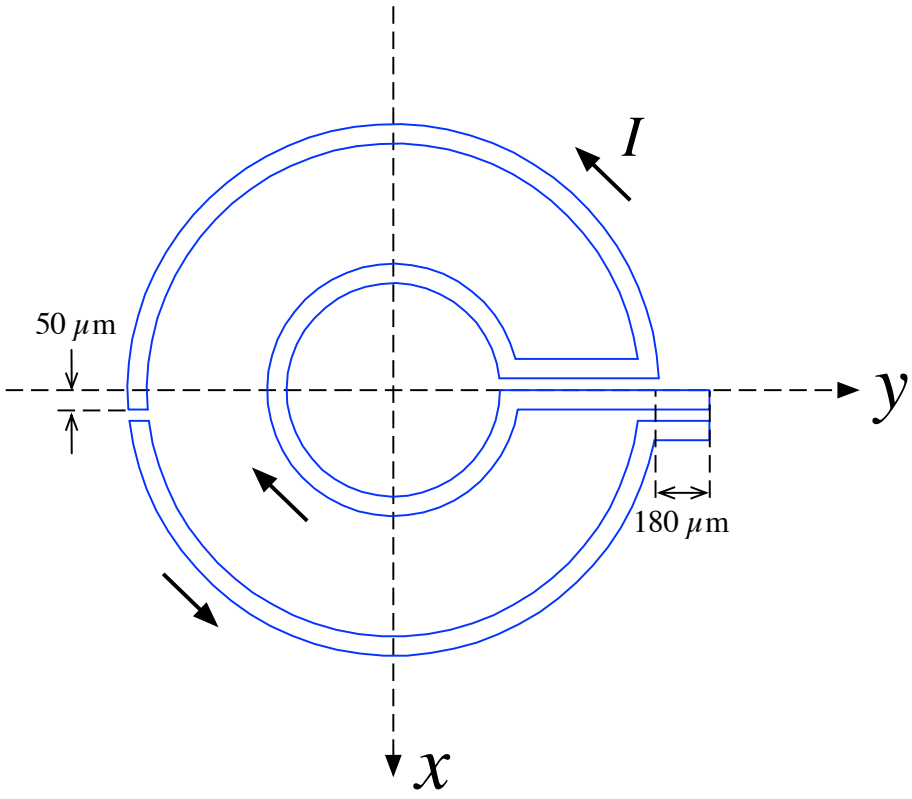

Figure 2.8: Schematic layout of a single double-loop with wire segments on one side for constructing a linear array of 3 microtraps used in the experiment. The radius of the inner (outer) loop, i.e. distance from the loop center to the middle of the microwire is 300 (660) μm. The wire width was 50 μm and the insulating gap separating the wires was 10 μm.

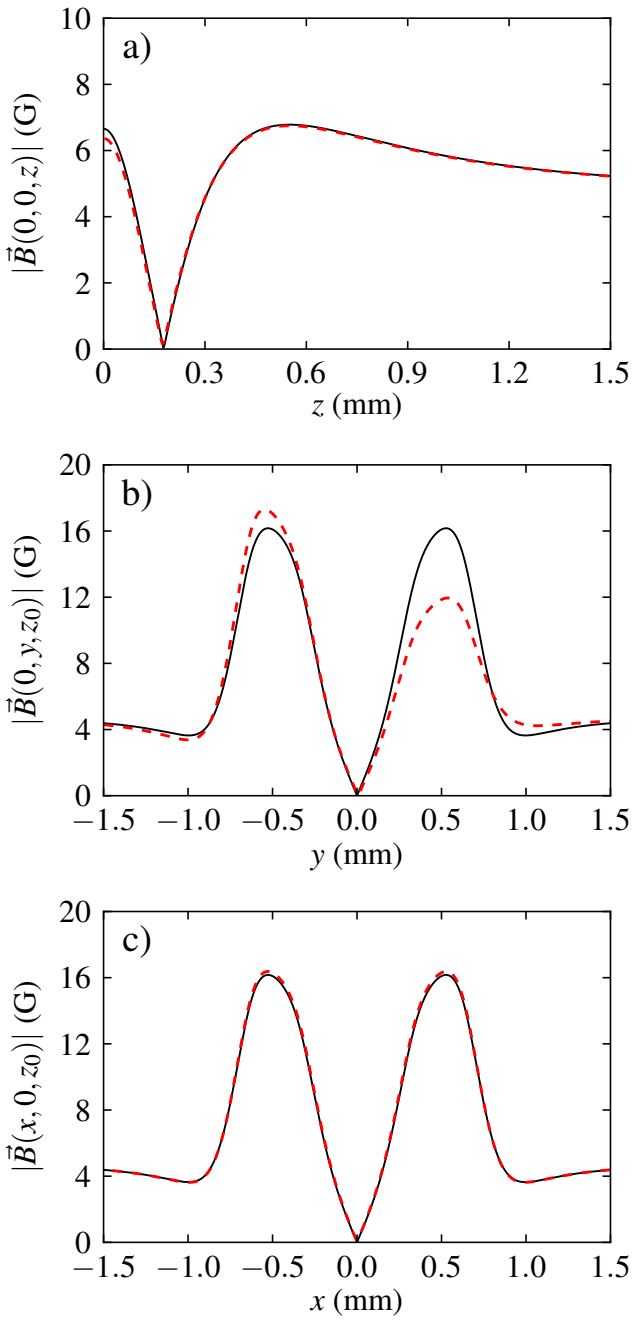

Figure 2.9: Comparison of the magnetic field generated by a single ideal double-loop microtrap and the trap shown in Figure 2.8. The trap was created using a current of 1 A and a bias field of $B_{\text{zbias}} = 1.43B_0 = 3.33$ G. The black curves show the magnetic field magnitudes of an ideal double-loop in (a), (b) and (c) along the z, y, and x directions through the trap center, respectively. The red dashed lines indicates the magnetic field magnitude generated by the double-loop microtrap shown in Figure 2.8.

3 Apparatus

This chapter describes the key parts of the apparatus: the atom chip, vacuum chamber, lasers, imaging system and the interface to the computer of the various components.

3.1 The atom chip and its mounting system

The double-loop wire pattern was fabricated using lithographic techniques [37, 77] onto an atom chip by ColdQuanta located in Boulder, Colorado. The chip is shown in Figures 3.1 and 3.2. It consists of a 10 μm thick copper layer covering a 0.4 mm thick SiO_2 substrate. The microwires have a width of 50 μm. On either side of the wires are 10 μm wide gaps in the copper layer that serve as insulators. The wire width increases as it nears the corners of the chip where it joins 3 mm square surfaces which are connected to macroscopic wires.

The reflectivity of the atom chip surface was measured to be $\geq$ 90% for light having a wavelength of 780 nm incident at an angle of 45°. This facilitated reflecting laser beams off the surface to generate a mirror MOT as is described in Chapters 5 and 6. The resistance of the atom chip wire pattern was measured to be 1.08 Ω which was in good agreement with the calculated value of 0.98 Ω. This generates a power of less than 10 W for currents below 3 A. The actual heat generated was reduced because the current only passed through the chip for short periods of time during the experiments. The copper block onto which the atom chip was attached acted as a heat sink. This block consisted of oxygen free high conductive copper which

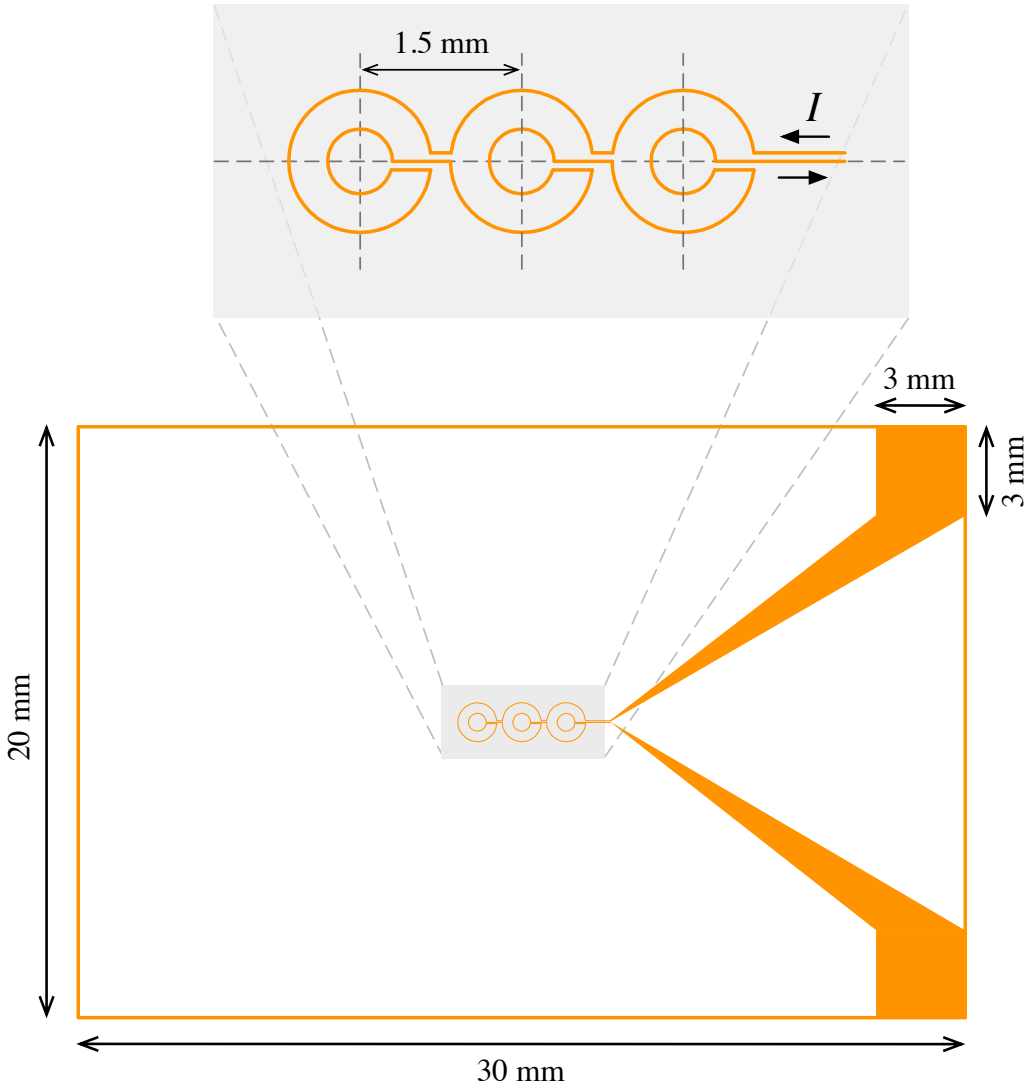

Figure 3.1: Diagram of the atom chip. The radii of the inner and outer loops of the double-loop pattern are 300 μm and 660 μm, respectively. The orange regions indicate the microwires which are physically separated from the remainder of the copper covered surface by 10 μm wide insulating gaps.

has a high thermal conductivity. No increase in background pressure associated with chip heating was observed. The atom chip assembly included a Rb dispenser (model RB/NF/3.4/12 FT10+10) from SAES which generated a rubidium vapour when a current of up to 4.2 A was applied.

The atom chip was mechanically clamped to the copper heat sink using four 2-56 screws as shown in Figure 3.2(a). Titanium as opposed to stainless steel screws were used to minimize the perturbation of the magnetic field near the microtrap. Two of these clamps also provided electrical connection to the power supply that generated the current for the atom chip. These two clamps were attached to an insulating Macor bar. Macor has a low vapor pressure and is machinable making it ideal for vacuum use. The entire atom chip assembly was attached to the top flange of the main vacuum chamber.

A serious problem was that the atom chip vibrated causing the mirror MOT to be unstable. Hence, the alternative method of using epoxy to attach the atom chip to the heat sink was developed as shown in Figure 3.2(b). Two different UHV compatible epoxies were employed. First, thermally conductive epoxy EpoTek H77 was used to mount the atom chip to the copper heat sink. The epoxy was cured by heating it to a temperature of 100 °C for one hour followed by two hours at 120 °C as specified by the manufacturer. Next, electrically conductive epoxy EpoTek H21D connected the atom chip at its two corners to two small copper blocks. It was cured in a single step by heating the chip assembly to a temperature of 120 °C for 15 minutes. The heating was done in a vacuum chamber pumped to a pressure of 10^{-4} torr to avoid oxidation of the atom chip surface which could degrade its reflectivity.

All UHV components were carefully cleaned to avoid contamination. This is essential as residual oils and grease may outgas limiting the attainable vacuum. Parts were initially cleaned using hot water and Sparkleen detergent. Next, they were rinsed with warm water. Items were then placed in an ultrasonic cleaner for 20 minutes. This last step was repeated using three solvents: trichloroethylene, acetone and methanol.

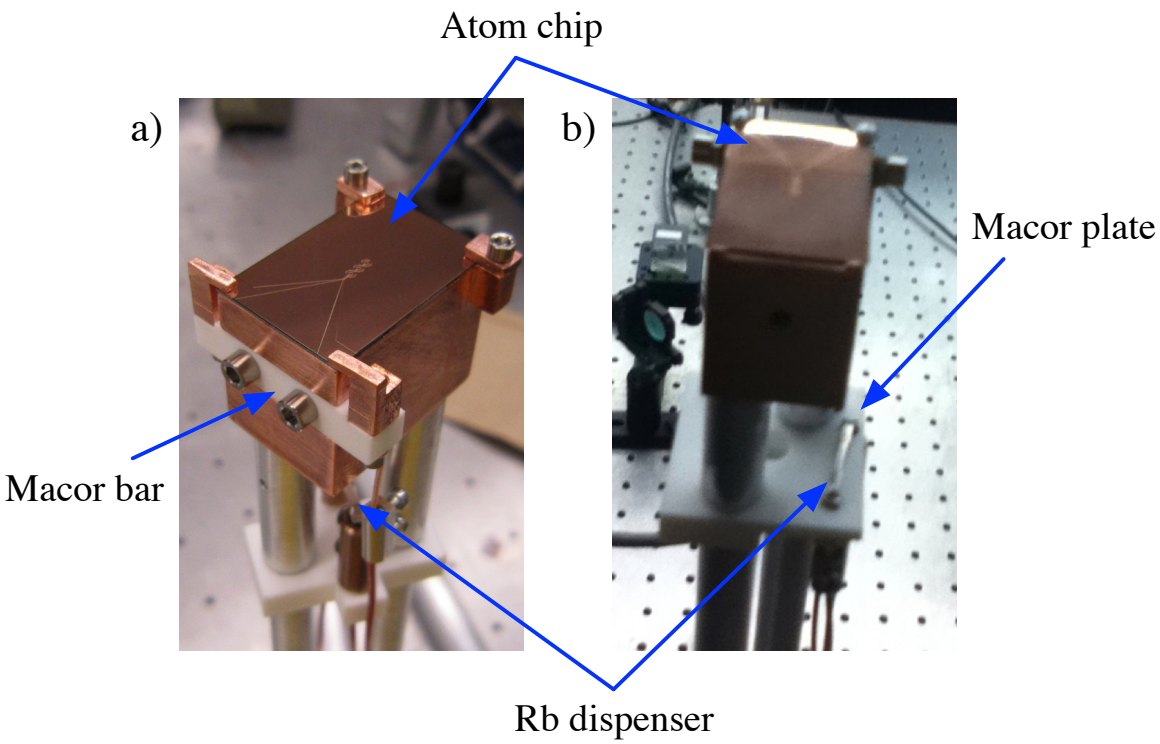

Figure 3.2: Atom chip assembly showing (a) the atom chip mechanically clamped and (b) epoxied to the copper heat sink.

3.2 Vacuum system

The vacuum system is illustrated in Figure 3.3. It was built to achieve a UHV vacuum of less than 1×10^{-9} torr. The central part is the glass cell encapsulating the atom chip assembly. The rectangular borosilicate glass cell was made by Precision Glass Blowing located in Boulder, Colorado. The cell has dimensions of 4.6 cm $\times$ 4.6 cm $\times$ 10.2 cm and a wall thickness of 4 mm. The outer wall was coated to reduce the reflectivity at the wavelength of 780 nm to less than 0.5%. The glass cell gave excellent optical access to a number of laser beams used to cool and probe the microtrapped atoms. A further advantage is that glass is not magnetic unlike stainless steel and therefore does not perturb the magnetic fields of the microtraps. Finally, magnetic coils could be placed very close to the glass cell which facilitated generating magnetic fields of the requisite strength using a minimum of electric current.

The glass was mated to a UHV flange that was attached to the main chamber. The latter was made from S340 stainless steel by Johnsen Ultrahigh Vacuum located in Burlington, Ontario. This chamber had two 6" diameter flanges, two 4.5" diameter flanges, and six 2.75" diameter flanges as shown in Figure 3.3. One 6" flange was attached to the glass cell while the other one supported the flange onto which the atom chip assembly was connected along with its electrical feedthroughs. One of the 2.75" flanges was connected to an all metal UHV valve (VLVE-5027, Duniway Stockroom, California). This was connected to a 200 l/s turbo pump (Varian Turbo-V 250 MacroTorr) which was backed up by a roughing pump (Edwards RV8, 3 l/s). A second 2.75" flange was connected to a residual gas analyzer (RGA, Model: 200, Stanford Research Systems, California). A 125 l/s ion pump (Varian Vacion plus 150 Starcell) that also contained a titanium sublimation pump (TSP) located inside a cylindrical liquid nitrogen trap, was connected to the main chamber by a 4.50" to 6.00" conical reducer nipple and a 6.00" straight nipple. The relatively large separation of 0.75 meters between the ion pump and the main chamber reduced the stray magnetic field of the ion pump at the atom chip to less than 0.5 G as measured

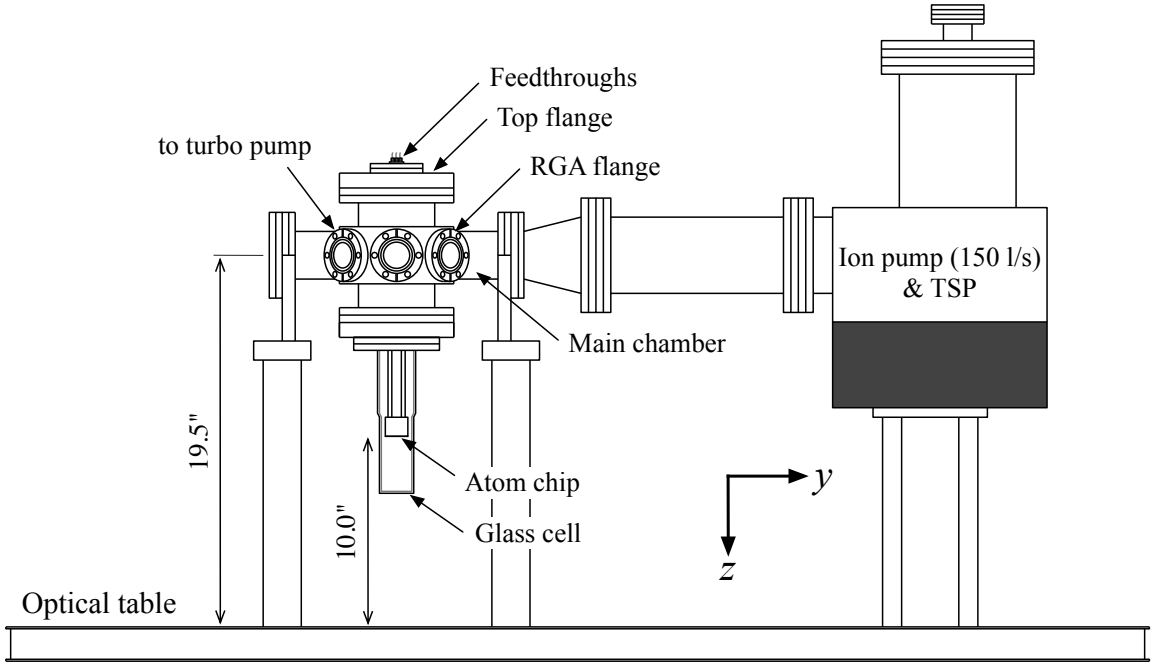

Figure 3.3: Schematic of the vacuum system.

using a Hall effect gaussmeter (Model 5180, F.W. Bell). This somewhat distant location of the ion pump also freed space around the glass cell which facilitated laser alignment.

The vacuum system was first pumped by the roughing and turbo molecular pumps for several hours to a level of 10^{-6} torr. Next, resistive heating tapes were wrapped around the vacuum system. The heating tapes were covered by two layers of aluminium foil to reflect the infrared radiation. Several thermometers measured the temperature of the glass cell and the main chamber. The temperature of the glass cell was not allowed to exceed 120 °C to avoid thermal stress which could crack the glass as well as possibly damage the antireflection coating. The main chamber was heated to a maximum of 160 °C.

The vacuum system was typically baked out for up to two weeks. During this period, a moderate current of 3 A was sent to the Rb dispenser to elevate its temperature and so avoid condensation of water vapour. Similarly, a current of 30 A was applied to the TSP. The pressure throughout the bakeout period was monitored using the RGA. The RGA gave a scan of the vapour pressure as a function of the mass of the residual gas. Before commencement of baking, notable peaks in units of amu were found at 2 (H_2), 18 (H_2O), 28 (N_2), 29 (Ar), 32 (O_2) and 44 (CO_2). At the end of the bakeout, the peaks due to H_2O, N_2, Ar, O_2 and CO_2 were nearly absent. The residual gas pressure of less than 10^{-9} torr was due nearly entirely to hydrogen. Finally, the TSP was turned on with the liquid nitrogen filled trap and the pressure was reduced to about 1×10^{-10} torr. This was an estimate because the reading was off the low end of the ion pump scale.

3.3 Laser systems

Two diode lasers, a trap laser and a repump laser, were used to generate ultracold atoms. A third infrared laser created the FORT. Finally, an imaging diode laser probed the atom clouds.

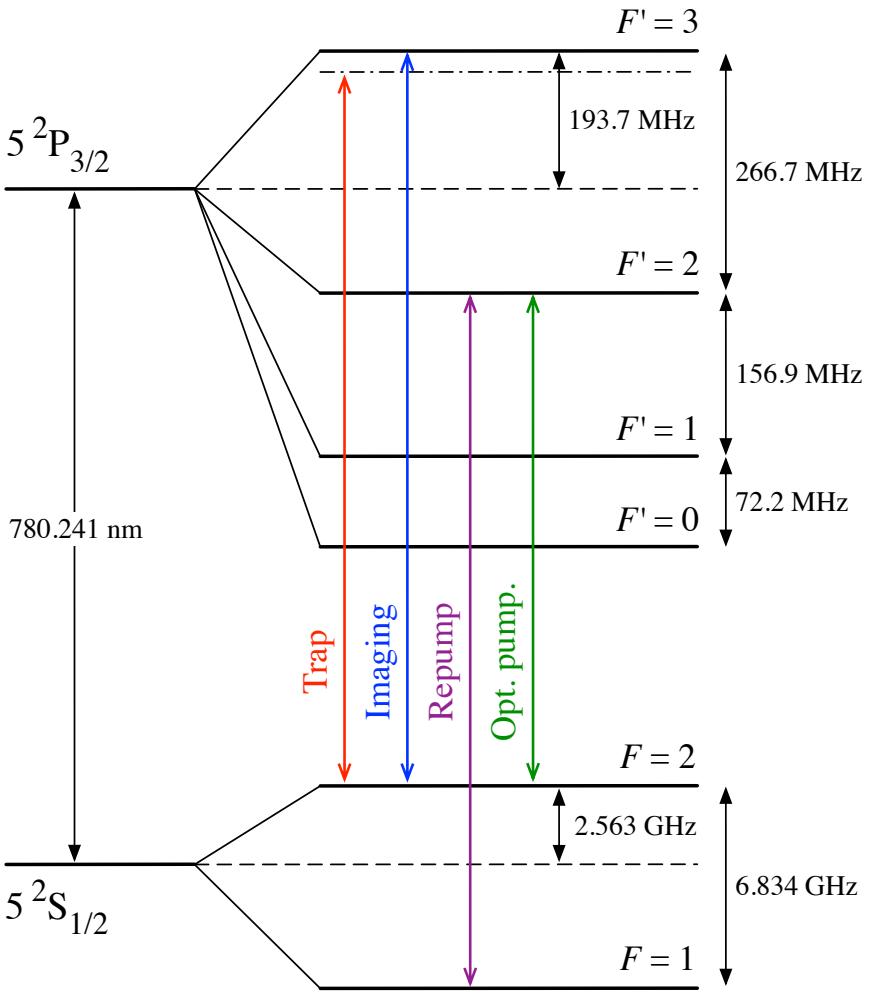

Figure 3.4: D2 hyperfine structure of ^{87}Rb with the laser transitions indicated.

3.3.1 Frequency locking

It was essential that the laser frequencies be stable relative to the rubidium transitions as shown in Figure 3.4. Each diode laser frequency was locked to a saturation absorption spectroscopy signal obtained using the apparatus illustrated in Figure 3.5 [78, 79]. Part of the laser beam produced by the diode laser was split off using a thin glass plate beamsplitter. This beam which had a power of about 1 mW then passed through a 1 cm thick glass plate that reflected part of the laser beam at each of its two surfaces. The two resulting laser beams, each having a power of about 10 μW, were called the reference and probe beams. They passed through the Rb vapour cell and were detected by photodiodes PD1 and PD2, respectively. The laser beam transmitted through the thick glass plate was called the pump beam and had a power of about 0.7 mW. It was directed through the vapour cell in the opposite direction as the probe beam which it intersected.

The laser intensity transmitted through the rubidium vapour cell decreased as the laser frequency was tuned across a resonance. The signal detected by photodiode PD1 had a broad dip corresponding to the Doppler absorption profile. Photodiode PD2 also showed this broad dip but in addition exhibited upward spikes when the laser frequencies corresponded to a transition to an excited state hyperfine level. These spikes were more clearly visible when the two photodiode signals were subtracted from each other to remove the broad Doppler background, as is shown in Figure 3.6(a). This figure shows a laser scan across the $5S_{1/2}\,(F=2) \rightarrow 5S_{3/2}\,(F')$ transition where F (F') denotes the ground (excited) state hyperfine level. Each peak is labelled by the excited state hyperfine level quantum number or the crossover peak [80].

The laser frequency was locked to a given peak as shown in Figure 3.6(a) by dithering the laser diode current so that the laser's frequency was modulated about the peak resonance at frequency ν_0 . The laser frequency was described by

$$\nu = \nu_0 + \Delta\nu \sin 2\pi\nu_{\mathrm{mod}} t. \tag{3.1}$$

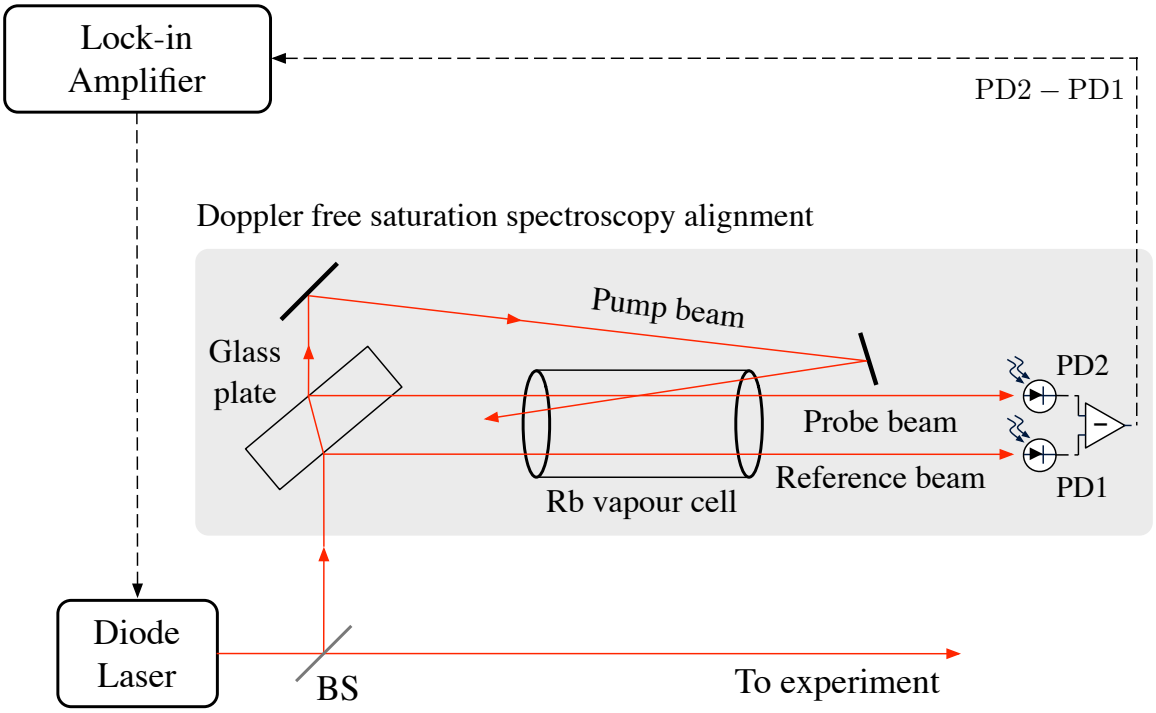

Figure 3.5: Laser alignment for the Doppler-free saturation absorption spectroscopy and the frequency locking circuit. BS denotes beam splitter while PD represents photodiode.

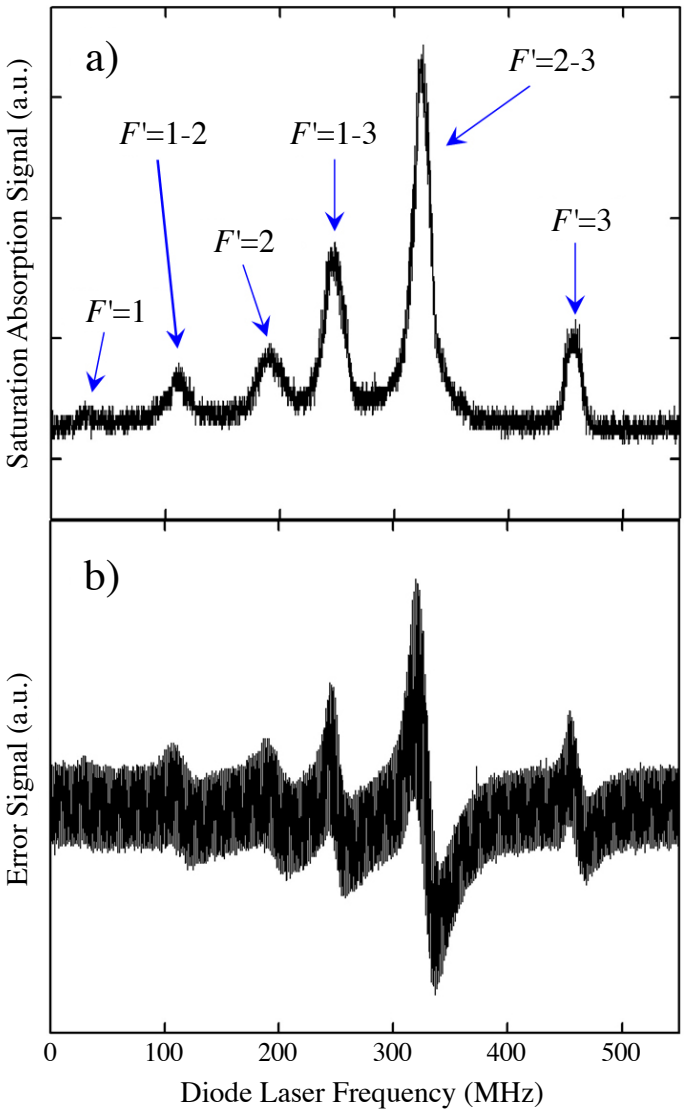

Figure 3.6: (a) Doppler free saturation spectroscopy signal generated by scanning the laser across the $5S_{1/2}\ F = 2 \rightarrow 5P_{3/2}\ F'$ resonance; (b) The error signal was obtained by taking the derivative of the signal in (a) which was used to lock the laser frequency as is described in the text. These signals are taken from the PhD. thesis of B. Schultz.

where $\Delta\nu$ describes the frequency range and $\nu_{\rm mod}$ is the modulation frequency which for the trap and repump lasers was 10 kHz. The photodiode signal, PD2-PD1, was given by

$$\begin{aligned} S(\nu) &= S(\nu_0 + \Delta\nu \sin 2\pi\nu_{\rm mod} t) \\ &\approx S(\nu_0) + S'(\nu_0)\Delta\nu \sin 2\pi\nu_{\rm mod} t \end{aligned} \tag{3.2}$$

where a Taylor expansion has been made of the right side. The signal was sent to a lock-in amplifier which mixed S with the reference signal used to dither the laser current.

$$\begin{aligned} L_1 &= S \cdot \sin 2\pi\nu_{\rm mod} t \\ &= \frac{1}{2}S'(\nu_0)\Delta\nu + S(\nu_0)\sin 2\pi\nu_{\rm mod} t - \frac{1}{2}S'(\nu_0)\Delta\nu \cos 4\pi\nu_{\rm mod} t. \end{aligned} \tag{3.3}$$

This signal then passed through a low pass filter such that only the DC component remained.

$$L_2 = \frac{1}{2}S'(\nu_0)\Delta\nu. \tag{3.4}$$

This was called the error signal. It is proportional to the first derivative of the signal S and is shown in Figure 3.6(b). The error signal equalled zero when the laser frequency coincided with the transition frequency ν_0. This error signal was fed into a Proportional-Integral-Derivative (PID) controller that modified the laser diode current to maintain $L_2 = 0$.

The laser frequencies were also strongly affected by temperature. Hence, the procedure was to turn the lasers on for several hours to allow the temperature to equilibrate. The laser frequency could then be locked to a transition for several hours. The resulting frequency jitter was less than 1 MHz which is smaller than the 6 MHz natural linewidth of the ^{87}Rb D2 transition.

3.3.2 Trap, optical pumping and repump lasers

All lasers along with their associated optics were positioned on a single optical table. The trap laser beam was generated by a TA 780 diode laser from TuiOptics. It consisted of an oscillator that generated a low power beam that passed through a tapered amplifier generating a beam having a power of 150 mW. A 60 dB optical isolator prevented optical feedback into the laser diode. This laser beam was horizontally polarized and had a manufacturer specified linewidth of 1 MHz. The laser frequency was locked to the $F' = 1 - 3$ crossover peak shown in Figure 3.6 (a). The trap laser then passed through a series of optics illustrated in Figure 3.7. The laser was directed back and forth through the small aperture of an acousto-optic modulator (AOM1, IntraAction ATE-1001A2) using two 50 cm focal length lenses. Acousto-optic modulators generate frequency shifted beams that are deflected through a small angle that depends on the modulation frequency. In our experiment, all AOMs were operated to maximize the intensity of the first diffracted laser beam. The advantage of using a double pass AOM1 is that the frequency shifted trap laser was not spatially deflected. This simplified laser beam alignment through subsequent optical elements. The AOM1 modulation frequency could be varied from 76 to 100 MHz, resulting in a trap laser beam that could be tuned from 60 to 12 MHz below the cycling transition. The modulation frequency was measured using a frequency counter (Optoelectronics, Cub MiniCounter). The resulting trap laser beam had a power of 110 mW and was directed to the "experimental table".

About 5 mW of the trap laser beam was split off using a half waveplate and a polarizing beam splitter to generate the optical pumping beam. This laser beam optically pumped the atoms to the magnetically trapped $|2, 2\rangle$ ground state Zeeman sublevel. The laser beam was focussed through acousto-optic modulator (AOM2, IntraAction ATE-2101A2), using two lenses having focal lengths of 15 and 12 cm. AOM2 operated at a modulation frequency of 237 MHz, which shifted the laser into resonance with the $F = 2 \rightarrow F' = 2$ transition as shown in Figure 3.4 when AOM1

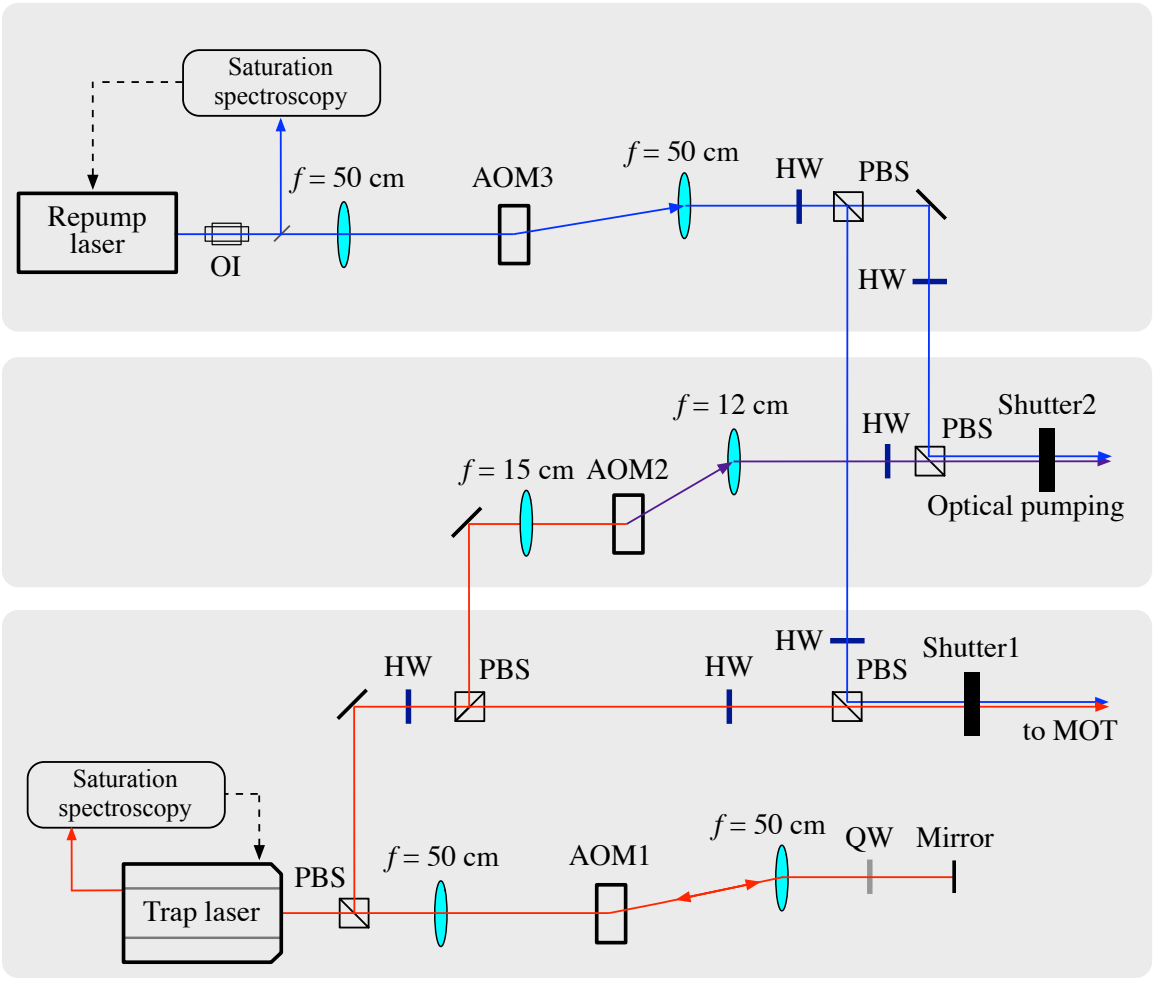

Figure 3.7: Layout of the trap, optical pumping and repump laser beams on the optical table. The abbreviations are acousto-optic modulator (AOM), polarizing beam splitter (PBS), optical isolator (OI), half waveplate (HW), quarter waveplate (QW) and photodiode (PD).

operated at a modulation frequency of 91 MHz. AOM2 operated using a low rf power as a laser power of 200 μW was sufficient to optically pump the atoms. The optical pumping laser beam was circularly polarized using a quarter waveplate.

The repump laser was generated by a DL 100 diode laser from TuiOptics. A 38.5 dB optical isolator (OFR IO-5-780-LP) protected the laser from optical feedback. The typical output power was 25 mW and the laser beam was vertically polarized. The laser frequency was locked to the $5S_{1/2}(F = 1) \rightarrow 5P_{3/2}\, F' = 1 - 2$ cross over peak. The laser frequency was shifted to the $5S_{1/2}(F = 1) \rightarrow 5P_{3/2}(F' = 2)$ transition using a single pass acousto-optic modulator (AOM3, IntraAction ATE-1001A2). AOM3 was supplied by a modulation frequency of 78.5 MHz. The repump beam was combined separately with both the trap laser and the optical pumping beams as shown in Figure 3.7 using half waveplates and polarizing beam splitters. The repump laser beam combined with the trap laser beam had a power of 5 mW while that combined with the optical pumping laser was about 100 μW. The repump laser intensity was controlled by varying the rf power of the modulation signal sent to AOM3. Finally, three mechanical shutters (Uniblitz Associates Model LS2 T20) with a manufacturer specified response time of 1.7 ms allowed temporal control of the trap, optical pumping and repump laser beams.

3.3.3 FORT laser

The FORT was generated using an infrared fiber laser (IPG Photonics YLR-30-1064-LP) operating at 1064 nm. This laser produced a maximum power of 30 W with a linear polarization. The optical layout diagram of the FORT laser and its associated optics is shown in Figure 3.8. The laser beam was first focussed using a 2 meter focal length lens through an acousto-optic modulator (AOM4, IntraAction ATM-803DA68). The purpose of AOM4 was to control the FORT laser temporally as well as to generate a frequency shifted laser beam of variable power from 0 to a maximum of 14 W by adjusting the amplitude of the modulation signal. AOM4 was operated

at a fixed modulation frequency of 40 MHz.

An important parameter in creating the FORT was the focal spot size. This was examined by using a removable mirror to direct the FORT laser beam toward a razor blade mounted on a translation stage as shown in Figure 3.8. The distance from the 20 cm focal length plano-convex lens to the translation stage equalled the distance from the lens to the middle of the glass cell. For a Gaussian beam having a beam waist radius a incident on a lens having a focal length f, the beam waist radius at the focus is given by

$$\mathrm{w}_0 = \frac{\lambda f}{\pi a} \tag{3.5}$$

In our experiment, the beam exiting the fiber laser had a Gaussian intensity distribution. However, the beam became asymmetric after the laser passed through AOM4. The FORT laser intensity was therefore described by

$$I(x,y) = I_0 \exp\left[-2\left(\frac{x^2}{\mathrm{w}_x^2} + \frac{y^2}{\mathrm{w}_y^2}\right)\right] \tag{3.6}$$

where w_x and w_y are the beam waists in the x and y directions, respectively. These parameters were determined by measuring the power as the razor blade was translated into the laser beam as is illustrated in Figure 3.9. The power found by integrating the intensity is given by

$$\begin{aligned} P(x) &= \int_{-\infty}^{x}\int_{-\infty}^{\infty} I(x',y')dx'dy' \\ &= \frac{P_0}{2}\left(1 - \mathrm{erf}\frac{\sqrt{2}\,x}{\mathrm{w}_x}\right) \end{aligned} \tag{3.7}$$

where the total laser power $P_0 = \frac{\pi}{2} I_0 \mathrm{w}_x \mathrm{w}_y$ and erf is the mathematical error function. Here, the origin of the x axis was selected to be at the center of the laser beam waist. Figure 3.9(a) shows a fit of Equation 3.7 obtained when the razor blade was translated in the x direction. The beam waist was determined at different positions z along the

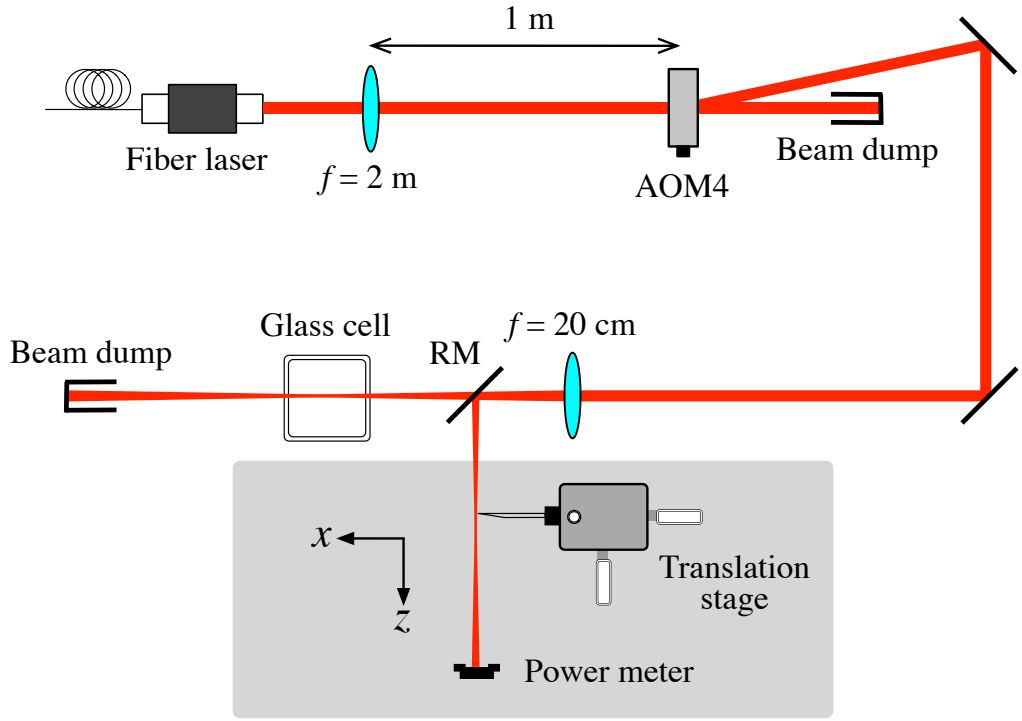

Figure 3.8: FORT laser and associated optics. A removable mirror (RM) was inserted to direct the laser beam toward a razor blade mounted on a translation stage to determine the beam waist as is described in the text.

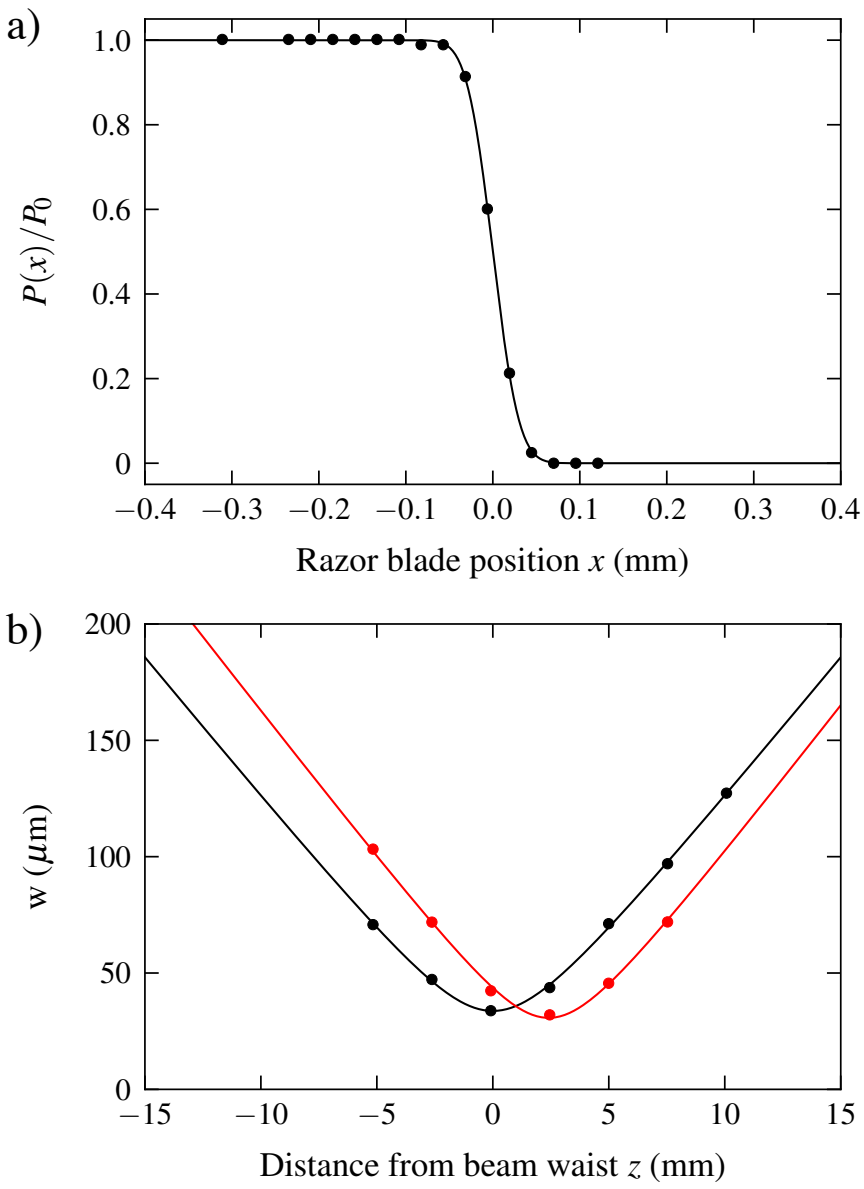

Figure 3.9: FORT laser beam waist measurement. (a) Measurement of the power as the razor blade was translated along the x direction at $z = -2.6$ mm. The fitted curve yielded a value of w $= 47.2 \pm 0.5$ μm. (b) Measurement of the beam waist along the laser propagation direction z. The fitted black (red) curve corresponds to translation of the razor blade along the x (y) direction as is discussed in the text.

laser propagation direction and was fitted to the following formula.

$$\mathrm{w}(z) = \mathrm{w}_0\sqrt{1 + \left(\frac{z - z_0}{z_R}\right)^2}. \tag{3.8}$$

Here, w_0 is the minimum beam waist that occurs at $z = z_0$. The origin of the z axis was chosen so that $z_0 = 0$ for the measurements made translating the razor blade in the x direction. The fit of Equation 3.8 shown in Figure 3.9(b) yielded a value of $\mathrm{w}_x = 34 \pm 1$ μm and a Rayleigh length of 2.8 ± 0.1 mm. The latter value was within 10% of the theoretical prediction. The measurements were repeated for the translation stage moving the razor blade along the y direction yielding $\mathrm{w}_y = 31 \pm 1$ μm. Figure 3.9(b) shows the laser beam was astigmatic having foci in the x and y directions at positions along the laser propagation direction that differ by 2.4 mm. The values of w_x and w_y at the point midway between these two foci were 37 and 34 μm, respectively. Hence, the average beam waist radius was estimated to be 35.5 ± 2 μm.

3.4 Imaging system

A third diode laser (New Focus, Vortex 6013) served as the imaging laser. The output of this laser was 6 mW. The layout diagram of this laser and its associated optical components and electronic instruments is shown in Figure 3.10. The laser frequency was locked to the same transition as the trap laser. The laser beam then passed though an acousto-optic modulator (AOM5, IntraAction ATE-1001A2) that shifted the imaging laser frequency to coincide with the $5S_{1/2}(F = 2) \rightarrow 5P_{3/2}(F' = 3)$ transition. AOM5 was operated at a fixed modulation frequency of 105.9 MHz. A function generator (Stanford Research System DS345) supplied a square pulse to the AOM5 driver to generate imaging pulses of 50 μs in duration. This instrument was in turn controlled by the computer.

The imaging laser passed through the ultracold atom cloud and was detected us-

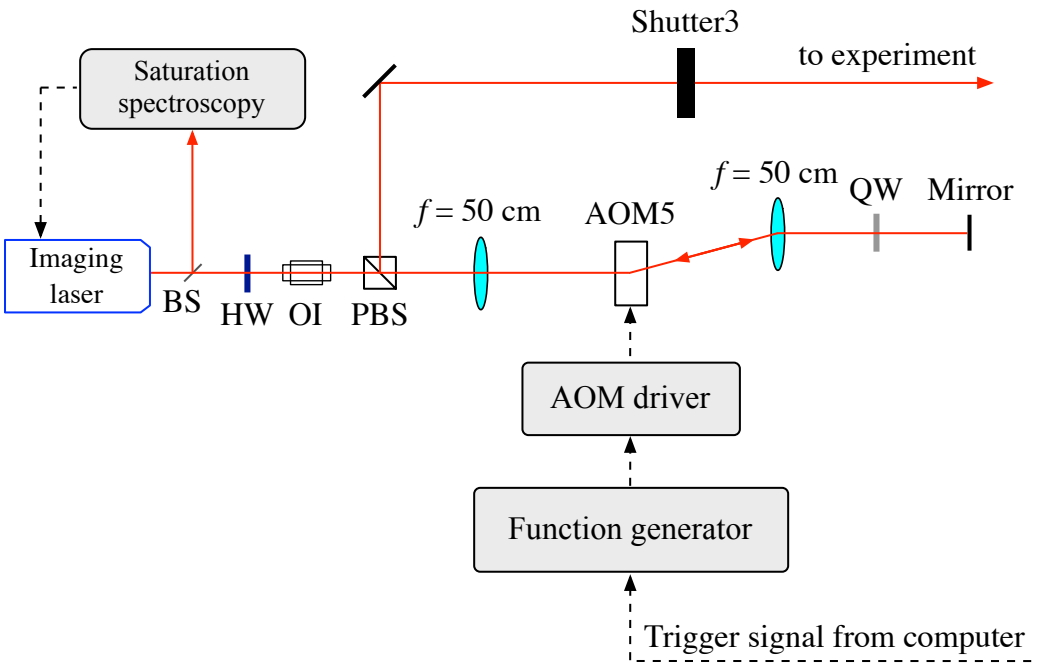

Figure 3.10: Layout of the imaging laser and associated optics as well as electronic instruments controlling AOM5.

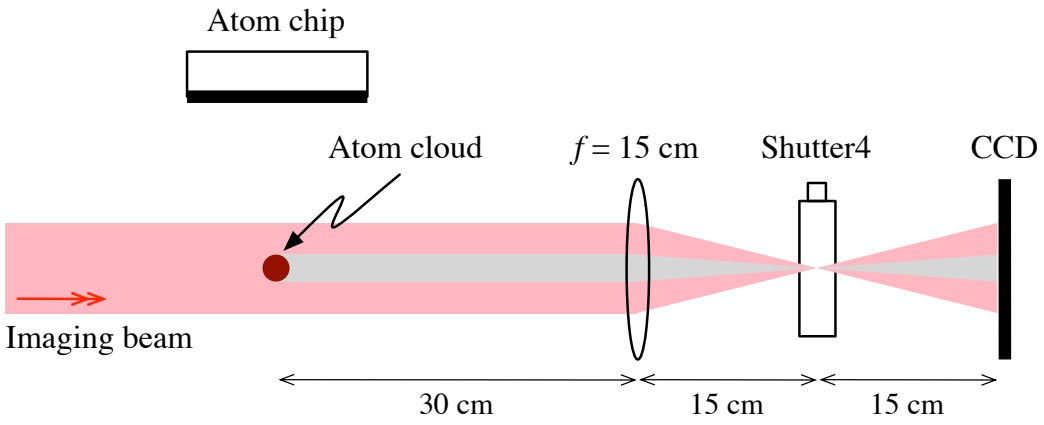

Figure 3.11: Absorption imaging system. The imaging laser passed through the atom cloud and was imaged onto a CCD camera as is discussed in the text.

ing a CCD camera (Santa Barbara Instrument Group ST-10XME) as illustrated in Figure 3.11. The atoms absorbed radiation producing a dark spot in the intensity of the transmitted laser beam. The atom cloud was imaged by a lens onto the CCD camera. The 15 cm focal length lens and the CCD camera were positioned so that the inverted image would have the same size as the object. The CCD consisted of an array of 2184 $\times$ 1472 pixels each with a size of 6.8 $\times$ 6.8 μm^2. The manufacturer specified quantum efficiency at 780 nm was 57%. It was cooled to -6.5°C by a Peltier cooler to reduce background noise. The CCD camera was interfaced to the experiment computer using a software (CCDOps version 5) from the CCD camera's manufacturer. A LabVIEW software program described in Appendix B synchronized the CCD camera with Shutter 4 (Uniblitz Associates Model LS2 T20). It was open for only 1 ms and was synchronized with the 50 μs imaging laser pulse to minimize the detection of scattered laser light. The minimum CCD exposure time was 50 ms. The CCD software uploaded the image to the computer.

3.5 Magnetic coils

The Earth's magnetic field was cancelled using three pairs of rectangular coils described in Table 3.1. Each of these coils contained 18 turns and was wound using AWG 18 magnetic wire. The currents were generated by a four-channel power supply (Agilent N6700B). The residual magnetic field at the location of the UHV glass cell was measured using the Hall effect gaussmeter to be less than 3 mG in the x, y and z directions.

The magnetic fields used to trap the atoms in a MOT as well as the magnetic quadrupole trap were generated using two quadrupole coils that were positioned along the x axis as shown in Figure 3.12. Each of the two circular coils are described in Table 3.2. The currents in the two coils were oppositely oriented to generate the quadrupole field. A current of 2 A was used to create a field gradient of 14 G/cm to operate the MOT while a higher current of up to 20A generated a field gradient

Table 3.1: Characteristics of the rectangular coils used to cancel stray magnetic fields.

Coil axis	x	y	z
Dimensions	80 cm × 53.3 cm	67.3 cm × 53.3 cm	67.3 cm × 80 cm
Coil separation	67.3 cm	80 cm	53.3 cm

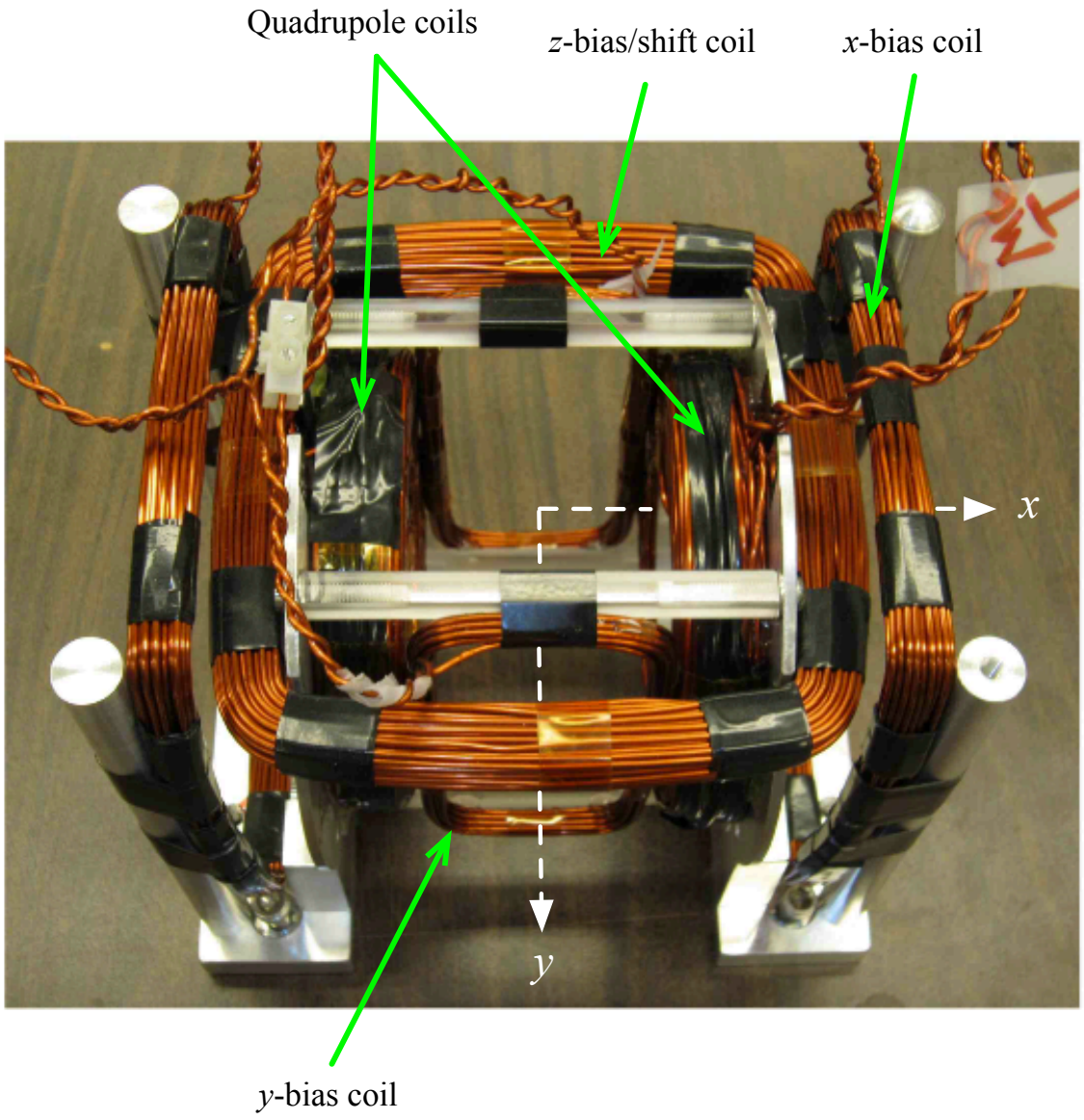

Figure 3.12: Coil assembly centered about the UHV glass cell used to generate magnetic fields.

Table 3.2: Description of the coils used to generate various magnetic fields. All dimensions are in cm and the resistance is given in ohms for a single coil. ICC stands for current control circuit which is described in Appendix A.

	Quadrupole	z-shift/bias	x-bias	y-bias
Coil shape	Circular	Rectangular	Rectangular	Rectangular
Inner size	5.1	9.4×9.4	9.7×12.7	4.1×10.2
Outer size	10.7	12.7×12.7	11.2×14.2	5.3×11.4
Coil separation	5.3	Not applicable	12.7	6.6
# turns/coil	140	72	28	14
Coil resistance	0.35	0.40	0.20	0.10
Wire type	AWG 14	AWG 16	AWG 16	AWG 16
Power supply	Kepco BOP 20-20 ML	Lambda LK 351 FMOV	Tenma 72-705	Lambda EMSII 20-50
Max. current (A)	20	20	3	3
Current control		ICC-01	ICC-03	ICC-04

of up to 140 G/cm for the magnetic trap along the axial direction of the coils. The coils were air cooled as the maximum power dissipated was only a few hundred W. The quadrupole coils were connected to a power supply (Kepco BOP 20-20ML). This supply was interfaced to the computer and was specifically designed to switch the 20 A maximum current off in less than 0.1 ms when the supply was connected to a large inductive load.

Figure 3.12 also shows additional coils that generated small bias magnetic fields along the x, y and z directions. These fields were needed to slightly shift the positions of the magnetic field minimum relative to the atom chip. This was critical to optimize the microtrap loading as will be discussed in Chapters 4 and 5. Two pairs of coils produced the bias fields along the x and y directions. The x-bias coils also provided a 3 G magnetic field to define the quantization axis during optical pumping. Only a single coil, placed 4 cm above the midpoint of the two quadrupole coils, generated B_{zbias}. A second coil for the bias magnetic field along the z-axis was not necessary and would limit optical access to the UHV glass cell. This coil also generated the B_{zshift} magnetic field used to shift the quadrupole trapped atoms located 17 mm below the atom chip surface close to the chip surface in the experiment described in Chapter 4. The currents were supplied by various power supplies that were computer controlled using home built current control circuits (ICC) that are described in Appendix A.

The quadrupole coils were supported by two circular aluminum frames connected using four plastic posts as is pictured in Figure 3.12. The frames were cut to suppress eddy currents created when the currents were abruptly switched off. The z-bias coil was arranged on top of the quadrupole coil and was epoxied to the frame. The y-bias coils were epoxied to the plastic posts while the x-bias coils were mechanically fixed to four aluminum posts.

3.6 Computer control and data acquisition

Precise temporal control of the various instruments with a 0.1 ms time resolution was critical. A LENOVO desktop computer with a Windows 7 operating system was interfaced to the experiment using a National Instruments PCI-6733 data acquisition card (DAQ). The DAQ controlled the voltages sent to the SCB-68 connector block which had 8 analog (16 bit) and 8 digital output channels. Table 3.3 shows the connections to the various instruments. A LabVIEW program which is described in Appendix B synchronized the various instruments during the experiments.

Table 3.3: Computer interface connections of the analog and digital channels to the corresponding instruments.

Analog Channel	Function	Digital Channel	Function
AO 0	Atom chip current	DO 0	Imaging laser shutter 3
AO 1	Trap laser frequency (AOM1)	DO 1	MOT laser shutter 1
AO 2	Quadrupole coils current	DO 2	Not used
AO 3	Trap laser power (AOM1)	DO 3	Imaging laser trigger (AOM5 signal generator)
AO 4	x-bias coils current	DO 4	Optical pumping laser shutter 2
AO 5	y-bias coils current	DO 5	CCD trigger
AO 6	Repump laser power (AOM3)	DO 6	Not used
AO 7	z-shift/bias coil current	DO 7	CCD shutter 4

4 Microtrap array loading from a transported quadrupole magnetic trap

This chapter describes loading the double-loop microtrap array from a transported quadrupole magnetic trap (QMT). Ultracold atoms were first generated using a MOT and then loaded into a quadrupole trap. An additional magnetic field shifted the center of the quadrupole trap towards the atom chip [81]. Atoms were then transferred into the microtrap array.

4.1 Experimental configuration and procedure

A modified 3d MOT [82] illustrated in Figure 4.1 was used as the cold atom source to load the double-loop microtrap array. The MOT laser beams in the y-z plane were retroreflected and intersected at an angle of 45° to position the MOT atom cloud closer to the atom chip. The MOT atom cloud was located only 17 mm below the atom chip surface.

The various steps in the procedure are described in Figure 4.2. The MOT was loaded from the background ^{87}Rb vapour that was generated by sending a current through the rubidium dispenser. Each of the trap laser beams had an intensity of about 16 mW/cm^2 and a beam diameter of 18 mm. The trap laser was red detuned 2.4Γ, below the $F = 2 \rightarrow F' = 3$ cycling transition. $\Gamma = 6.1$ MHz is the FWHM natural linewidth of the D2 line. A 4 mW repump laser beam, resonant with the $F = 1 \rightarrow F' = 2$ transition of the D2 line, overlapped with each of the trap laser

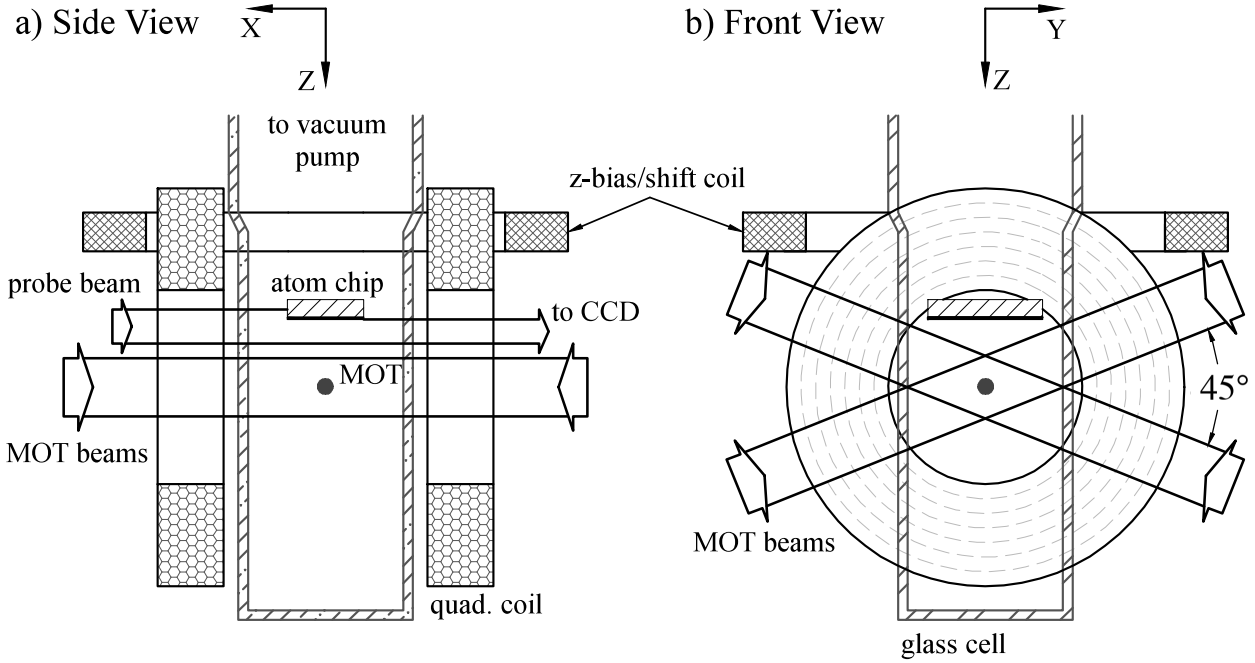

Figure 4.1: Schematic of the apparatus for loading the microtrap array from a transported quadrupole magnetic trap.

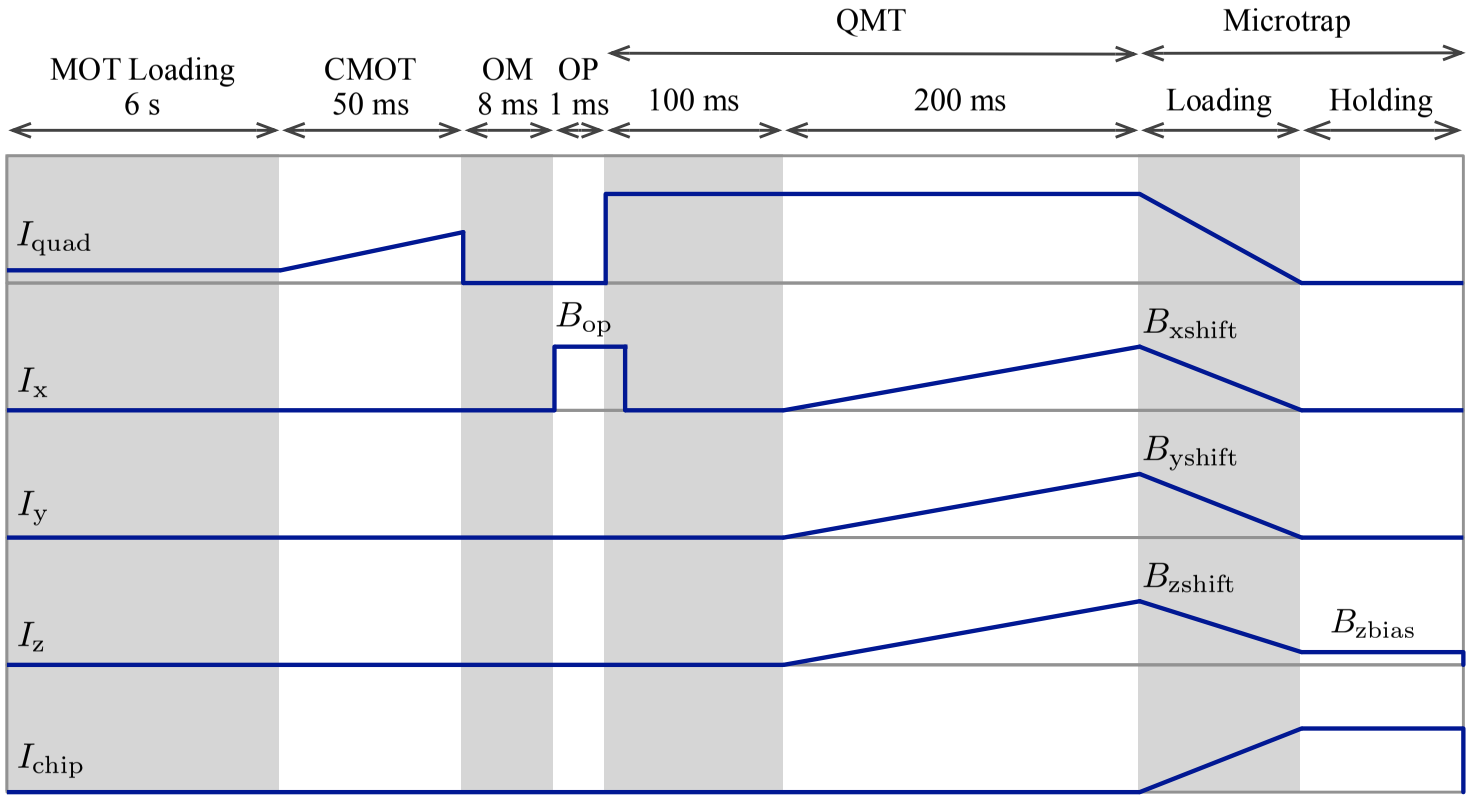

Figure 4.2: Timing sequence of the currents that generated various magnetic fields used to load the microtrap array. Ultracold atoms were first generated in a MOT which was compressed (CMOT). The atoms were then further cooled using optical molasses (OM) after which they were optically pumped (OP) to the $|2,2\rangle$ Zeeman sublevel. The atoms were then captured in a quadrupole magnetic trap (QMT). The transverse position of the QMT was adjusted using fields in the x and y directions and moved in the z direction toward the atom chip so as to overlap the microtrap array into which the atoms were transferred.

beams, preventing atoms from accumulating in the $F = 1$ ground state hyperfine level. The magnetic field gradient for the MOT was 14 G/cm along the axial (x) direction. Typically, 2.5×10^7 atoms were loaded in 6 s into the MOT which had a diameter of about 2 mm.

The next CMOT stage was to compress the MOT. This was done by linearly ramping up the current $I_{\rm quad}$ in a time of 50 ms increasing the quadrupole magnetic field gradient to 35 G/cm. Simultaneously, the trap laser red detuning was linearly increased to 5Γ. This was necessary to avoid heating the atoms. At higher magnetic fields the sublevels experienced larger Zeeman shifts and could more easily absorb the trap laser light. The resulting CMOT cloud had about the same number of atoms as the original MOT cloud but its volume was reduced by a factor of 2.

The atom temperature was reduced during the optical molasses (OM) stage. All magnetic fields were suddenly turned off at the beginning of the 8 ms optical molasses phase and the trap laser detuning jumped to 10Γ. The MOT atom cloud at the end of the optical molasses stage was examined by measuring the absorption of the imaging laser as it passed through the cloud. Typically, the atom cloud contained the same number of atoms as at the end of the MOT loading phase corresponding to a peak density of 1.5×10^{10} atoms/cm^3. The atom temperature of 40 μK was determined using the time of flight method that will be discussed later in this chapter.

The atoms were next optically pumped (OP) for 1 ms to the $|2, 2\rangle$ ground state Zeeman sublevel. This was done to maximize the number of atoms populating the Zeeman sublevels that could be captured into the quadrupole magnetic trap (QMT). The MOT laser was blocked at the end of the OM stage using Shutter 1. Optical pumping was done using a current $I_{\rm x}$ that generated a bias magnetic field of 3 G in the x direction to define the quantization axis. The optically pumping laser beam was generated by frequency shifting part of the trap laser into resonance with the $F = 2 \rightarrow F' = 2$ transition of the D2 line as described in Chapter 3. This beam was overlapped with the 0.1 mW repump laser beam and expanded to 15 mm in diameter

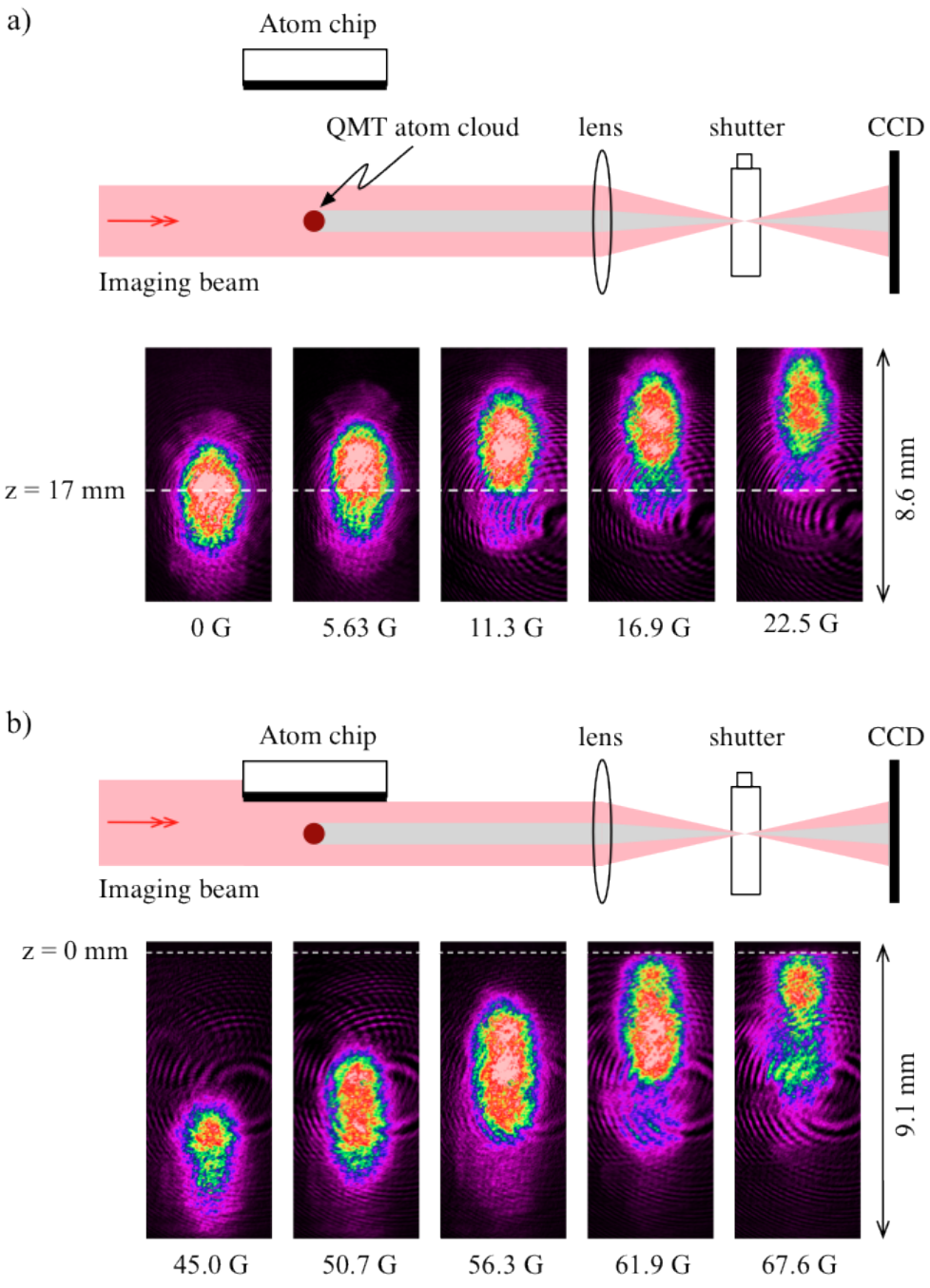

Figure 4.3: Images of the QMT atom cloud shifted upwards for various values of B_{zshift}. (a) shows images obtained beginning when the atom cloud was located 17 mm below the atom chip surface whose position is at $z = 0$. (b) shows images taken when the atom cloud was closer to the atom chip. The imaging laser and associated detection system were translated upwards as shown.

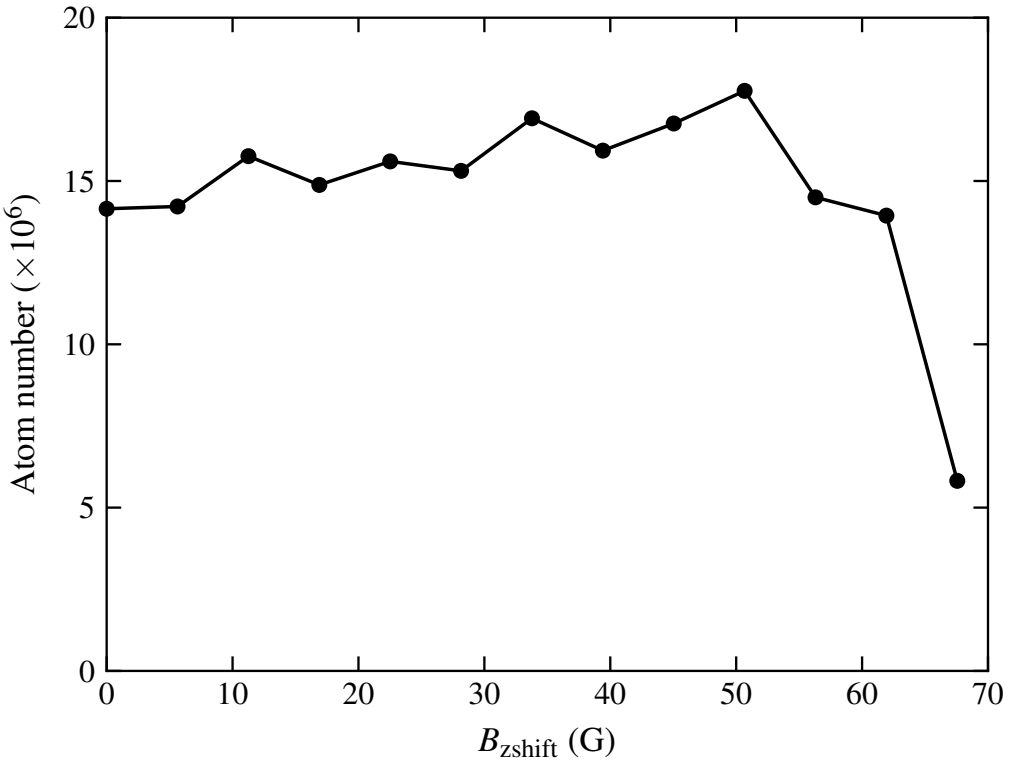

Figure 4.4: Number of atoms in the QMT after it was shifted upwards and brought back to its initial position as a function of the B_{zshift}.

using a telescope. The optical pumping laser beam was then combined with one of the MOT laser beams propagating along the x direction using a PBS cube and passed through a quarter waveplate to generate circularly polarized light. The power of the circularly polarized optically pumping laser beam before the vacuum glass cell was 0.1 mW. During the MOT operation, the optical pumping light was blocked using Shutter 2.

The atoms were captured by the QMT by switching on the current $I_{\rm quad}$ to 12 A which corresponded to a 84 G/cm field gradient in the axial (x) direction. Over 90% of the MOT atoms were transferred into the QMT. The optical pumping bias field was switched off 1 ms after $I_{\rm quad}$ was turned on to ensure that atoms remained in the magnetically trapped Zeeman sublevels. All laser beams were also blocked using various AOMs and mechanical shutters. The lifetime of the atoms in the QMT was observed to be approximately 1 s.

After 100 ms, the QMT atom cloud was transported toward the atom chip by linearly increasing the $B_{\rm zshift}$ field over a 200 ms interval [81, 83]. The shifted QMT cloud was imaged as shown in Figure 4.3. For fields $B_{\rm zshift} > 25$ G, the QMT atom cloud shift exceeded the diameter of the imaging laser beam. This beam and its associated optics were therefore translated upwards.

The transport efficiency was examined by moving the atoms upwards to the atom chip and then back down to its initial position by increasing and decreasing $B_{\rm zshift}$. The QMT cloud was then observed using the imaging laser and the number of atoms found. Figure 4.4 shows a plot of the atom number versus the maximum value of $B_{\rm zshift}$. No loss of atoms was evident for $B_{\rm zshift} < 60$ G. The number of atoms decreased sharply at higher $B_{\rm zshift}$ because the atom cloud collided with the atom chip surface as is shown in Figure 4.3(b). The QMT cloud transported near the atom trap, was elongated along the z-axis direction. This reduced the peak trapped atom density from about 1.0×10^{10} to 5.0×10^{9} atoms/cm^3. The atom temperature after transport to the atom chip was measured to be 100 μK.

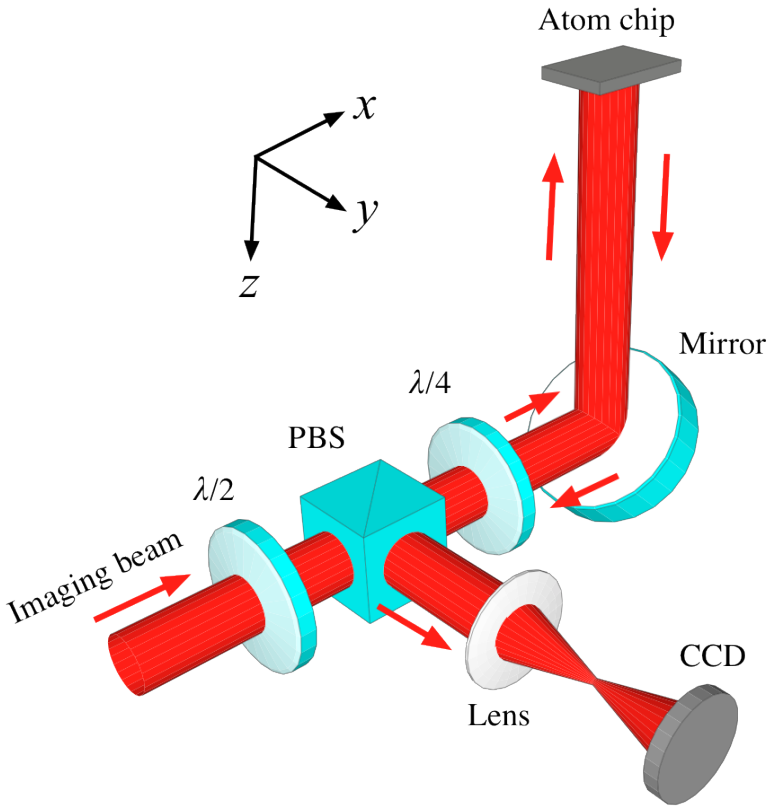

Figure 4.5: Absorption imaging system used to image the transported QMT atom cloud position relative to the double-loop wire pattern. The half waveplate ($\lambda/2$) adjusted the incoming imaging laser beam to be linearly polarized along the z direction. The laser therefore was transmitted through the polarizing beam splitter (PBS). A quarter waveplate ($\lambda/4$) converted the light to be circularly polarized. The laser beam then passed through the atom cloud and was reflected off the atom chip surface. The quarter waveplate then converted the reflected laser beam into horizontal linearly polarized light which was directed by the PBS into the CCD camera.

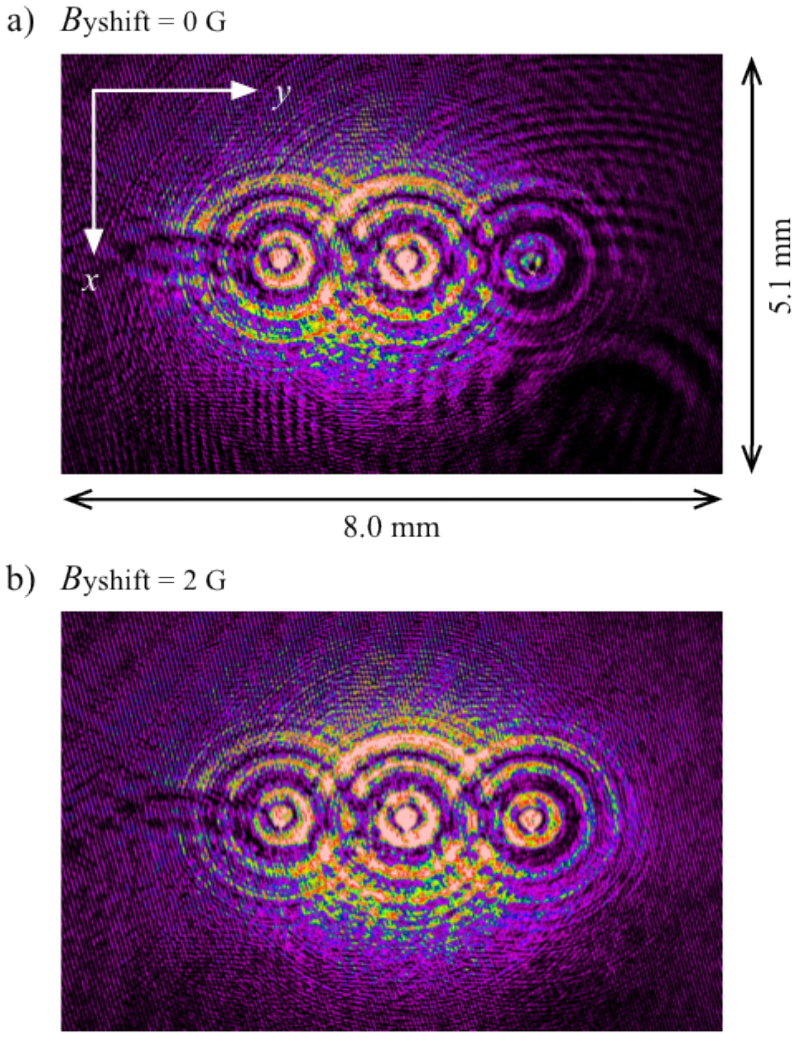

Figure 4.6: Effect of the magnetic field in the y direction on the QMT atom cloud position for (a) $B_{\text{yshift}} = 0$ G and (b) $B_{\text{yshift}} = 2$ G. The three double-loop microtraps each separated by 1.5 mm appear as three bright spots in the centers of the figures. Both of these images were taken with the QMT atom cloud shifted close to the atom chip surface using $B_{\text{zshift}} = 64.8$ G.

The alignment of the QMT atom cloud in the x and y directions was studied using the absorption imaging system illustrated in Figure 4.5. The imaging laser beam was directed in the vertical direction passing through the QMT atom cloud before being reflected off the atom chip. The transverse position of the QMT atom cloud could be adjusted by applying small shifting magnetic fields B_{xshift} and B_{yshift}. The CCD image given in Figure 4.6 showed the atom cloud overlapped very well with the microtrap array. The values of $B_{\text{xshift}} = 0.5$ and $B_{\text{yshift}} = 2$ G gave optimum overlap of the transported QMT cloud with the middle microtrap.

Atoms were transferred into the microtrap array by linearly increasing the atom chip current to 2.6 A during a loading time that was varied between 0 and 200 ms. Simultaneously, the currents that generated the QMT field, B_{xshift} and B_{yshift}, were reduced to zero as shown in Figure 4.2. The magnetic field in the z direction was ramped down from B_{zshift} to B_{zbias}. The microtrapped atoms were held for times up to 600 ms before they were imaged. The imaging laser pulse was incident on the atoms at a time varied between 0.2 and 2.5 ms after the atom chip and bias magnetic field currents were abruptly turned off. It was necessary to image the atoms without any magnetic field that can Zeeman shift the atoms out of resonance with the imaging laser beam whose frequency was fixed.

Figure 4.7 shows a typical absorption image of the atom clouds trapped in the middle and left microtraps containing 1.5 and 0.5×10^5 atoms, respectively. The absorption imaging of the atoms is discussed in Appendix C. The microtraps were loaded using values of $B_{\text{zshift}} = 64$ G, $B_{\text{zbias}} = 12.4$ G and a chip current of 2.6 A. The loading time was 40 ms and the atoms were held for 60 ms in the microtraps. The atom cloud was probed 0.6 ms after the microtrap array was turned off. Almost no atoms were loaded into the right microtrap because the QMT atom cloud was positioned between the middle and left microtraps. The microtrapped atom clouds were analyzed by fitting the optical depth (OD) in the horizontal y direction to the sum of three Gaussian functions.

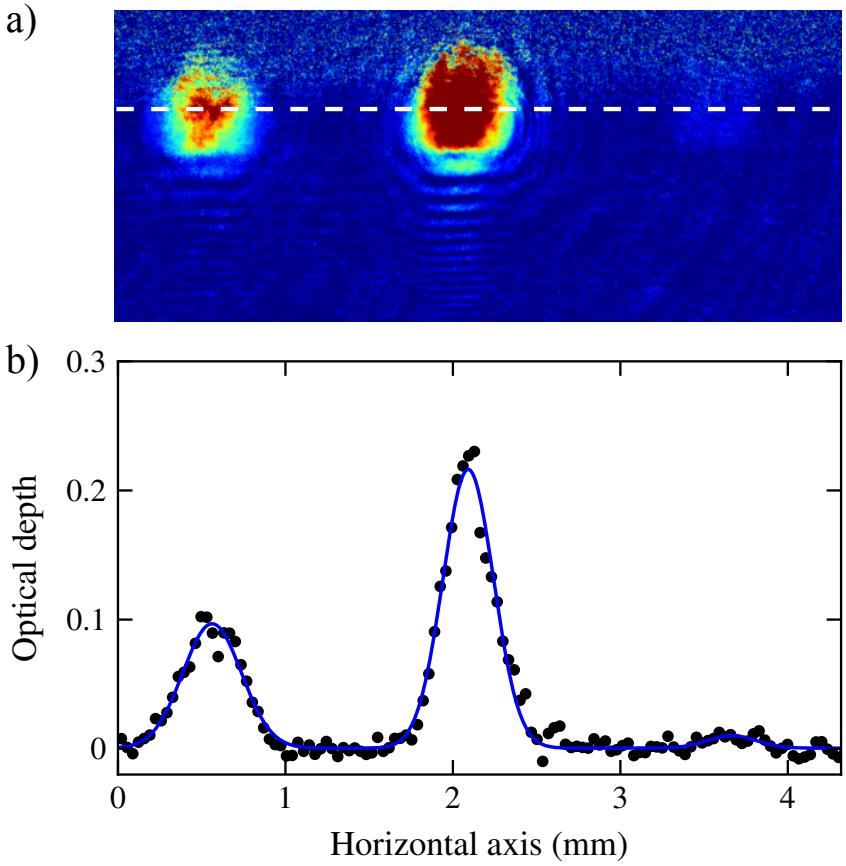

Figure 4.7: (a) Sample image of the microtrap array atom clouds; (b) The optical depth of the microtrapped atom clouds along the white dashed line in (a). Each dot represents an average of 5 neighbouring pixels. The curve in (b) is a sum of Gaussian functions fitted to the data as described in the text.

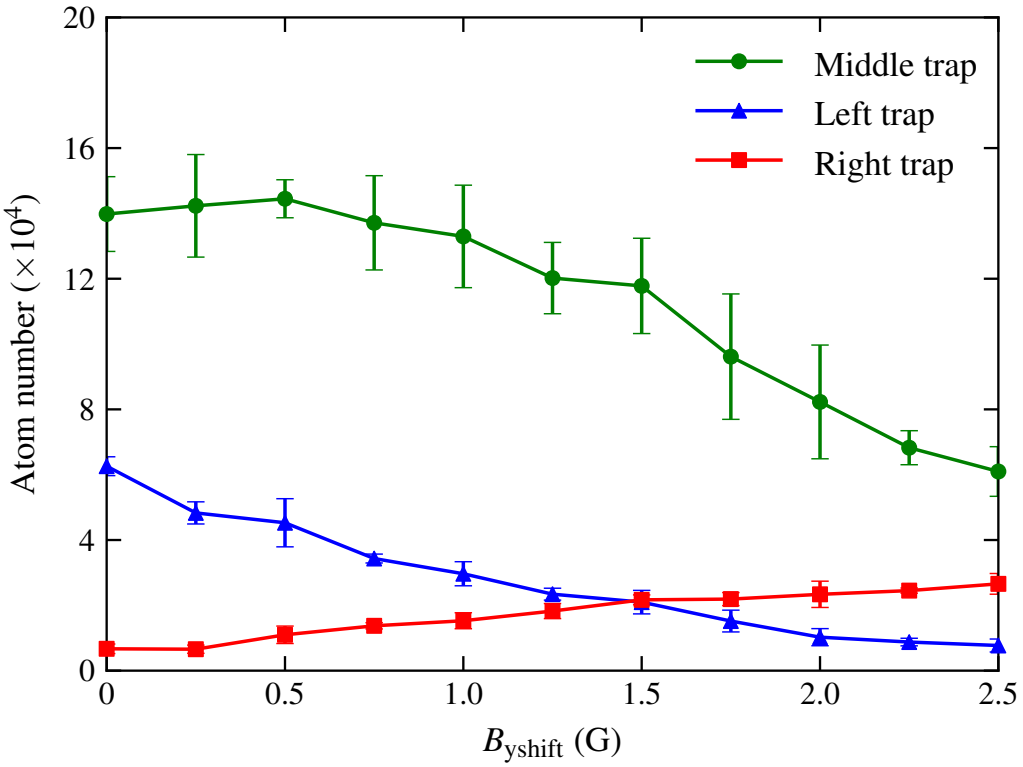

Figure 4.8: Number of atoms in the three microtraps as a function of B_{yshift}. This data was taken using $B_{\mathrm{zshift}} = 60.8$ G, $B_{\mathrm{zbias}} = 12.4$ G, a 40 ms loading time, a 60 ms holding time and a probe delay of 0.6 ms.

$$\mathrm{OD}(y) = \sum_i A_i \exp \frac{-(y - y_i)^2}{2\sigma_i^2}, \tag{4.1}$$

Here y_i is the center position of the atom cloud in the i^{th} microtrap and σ_i is the corresponding cloud radius. The left and middle microtrap radii were found to be 150 and 175 μm, respectively. The atom cloud radii in the vertical z direction were found to nearly equal σ_i.

The distribution of atoms loaded into the linear array of three microtraps could be controlled by adjusting the magnetic field in the y direction, B_{yshift}, as is shown in Figure 4.8. This field shifted the location of the QMT relative to the microtraps. The relative microtrap populations were varied using fields up to 2.5 G, which was limited by the available power supply.

4.2 Optimization of microtrap loading

The number of atoms in the microtraps was optimized by varying B_{zshift}, B_{zbias} and the loading time. Figure 4.9 shows the dependence of the number of atoms loaded into the middle microtrap on B_{zshift}. At fields below 55 G, few atoms were loaded into the microtrap because the QMT was not located close to the atom chip. For fields between 55 and 62 G, the number of atoms in the microtrap increased approximately linearly with B_{zshift}. The optimum number of atoms loaded into the microtrap occurred using B_{zshift} between 62 and 67 G. At higher fields, the QMT atoms collided with the atom chip surface and the number of atoms loaded into the microtrap decreased sharply.

The dependence of the number of atoms loaded into the middle microtrap on B_{zbias} is shown in Figure 4.10(a). About 5000 atoms could be trapped using no bias field. The number of microtrapped atoms increased approximately linearly as B_{zbias} increased. This behaviour agreed very well with the prediction in Chapter 2 that showed the maximum depth for the middle microtrap in an array occurs when $B_{\mathrm{zbias}} = 1.60 B_0 = 13.9$ G, which is about three times larger than when $B_{\mathrm{zbias}} = 0$.

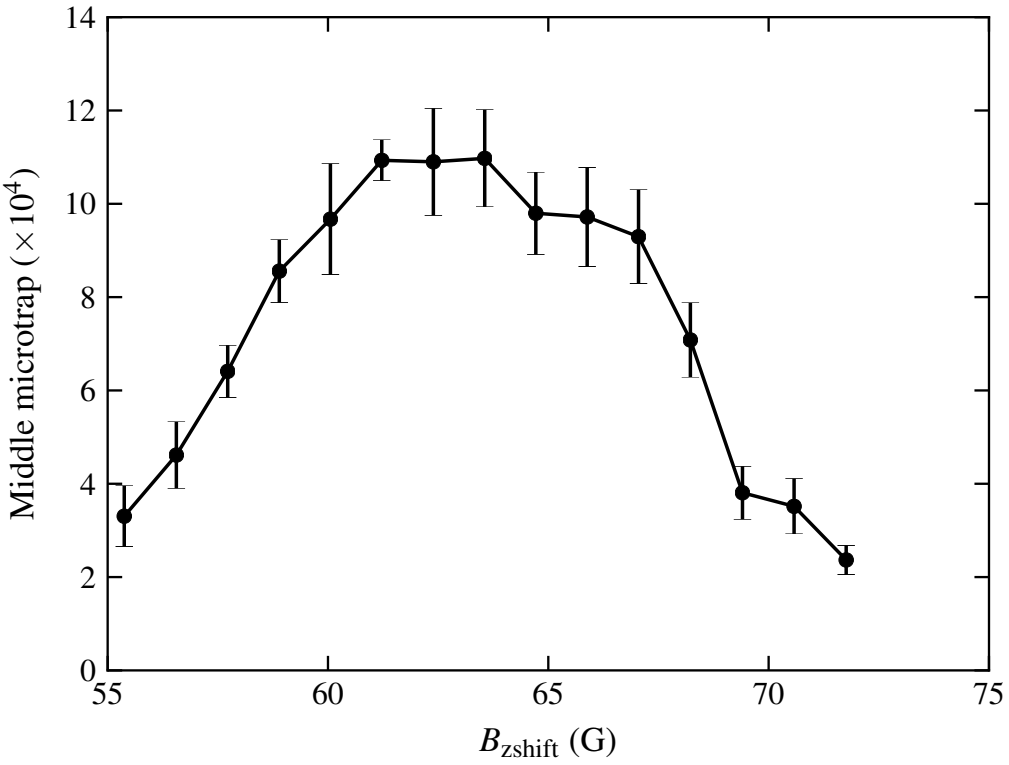

Figure 4.9: Number of atoms in the middle microtrap as a function of B_{zshift}. This data was taken using a 40 ms microtrap loading time, $B_{\mathrm{zbias}} = 12.4$ G, $B_{\mathrm{yshift}} = 1$ G, a 100 ms holding time and a probe delay of 0.6 ms. The error bars were the statistical error from the mean value of at least three measurements for each point.

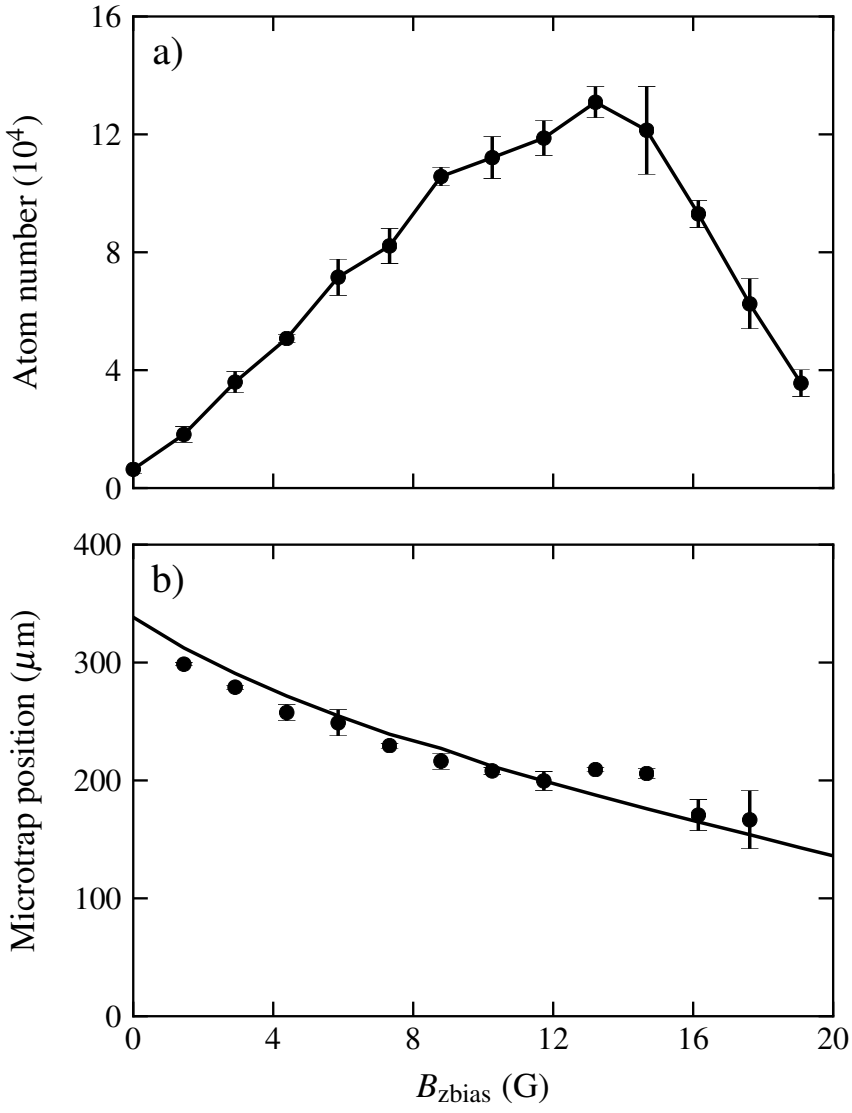

Figure 4.10: (a) Number of atoms and (b) position of the middle microtrap as functions of B_{zbias}. The curve in (b) is the microtrap position calculated as described in Chapter 2. This data was taken using a 40 ms microtrap loading time, $B_{\mathrm{zshift}} = 60.8$ G, $B_{\mathrm{yshift}} = 1$ G, a 100 ms holding time and a probe delay of 0.6 ms.

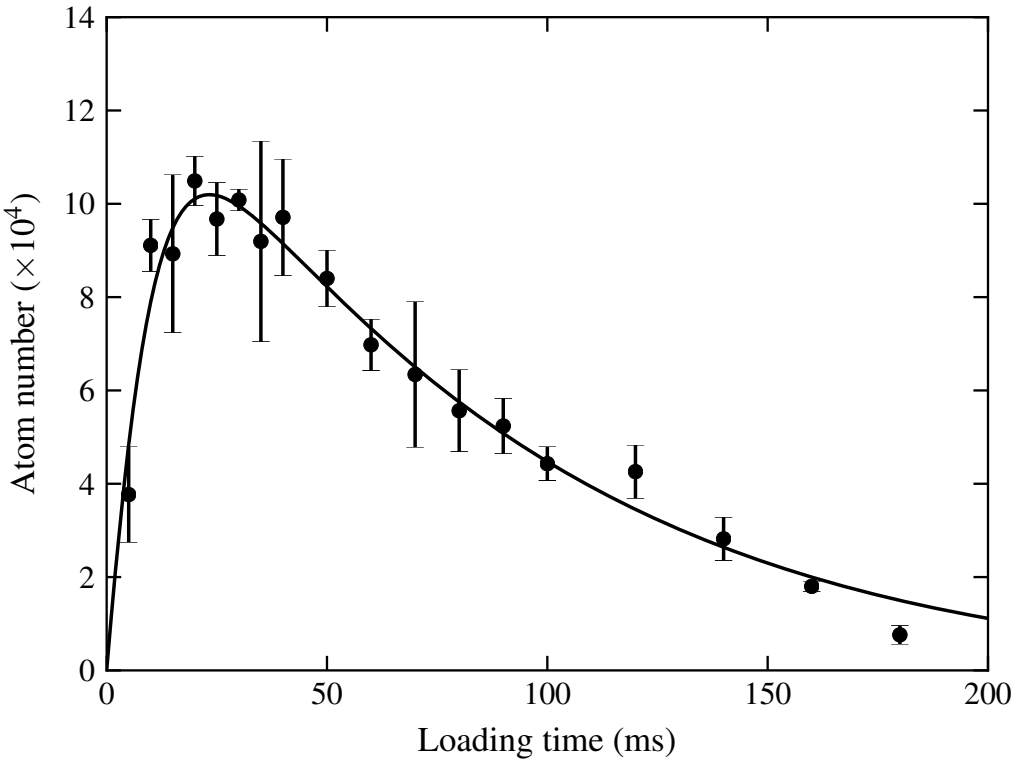

Figure 4.11: Number of atoms in the middle microtrap as a function of the loading time. The curve was fitted to the data as described in the text. This data was taken using $B_{\mathrm{zshift}} = 60.8$ G, $B_{\mathrm{yshift}} = 1$ G, $B_{\mathrm{zbias}} = 12.4$ G, a 100 ms holding time and a probe delay of 0.6 ms.

The bias field also shifted the microtrap position toward the atom chip as is shown in Figure 4.10(b). The error bars are the statistical error calculated from at least three measurements for each point. There was an additional uncertainty because diffraction of the imaging laser beam resulted in a somewhat blurred CCD image of the atom chip surface. The fitted curve therefore had an adjustable parameter that exactly specified the atom chip position when fitting the data to the numerically simulated microtrap position as discussed in Chapter 2.

The dependence of the atom number in the middle microtrap as a function of the loading time is shown in Figure 4.11. The data was modelled using

$$\frac{dN}{dt} = R\, e^{-t/\tau} - \alpha N, \tag{4.2}$$

where the first term on the right hand side describes loading N atoms into the microtrap at a rate R with a time constant τ during time t [72]. The second term takes into account the loss of atoms due to collisions with residual background gas. An additional loss term due to collisions between ultracold microtrapped atoms was not considered because of the relatively low density ($\sim 10^{10}/\mathrm{cm}^3$) of the microtrapped atom cloud. The best fit of Equation 4.2 to the data gave values of $R = 1.27 \times 10^8$ s^{-1}, $\tau = 75$ ms and $\alpha = 89$ s^{-1}.

4.3 Characterization of the microtrap

The temporal dependence of the atom number in the middle microtrap is shown in Figure 4.12. The data were very well fitted to an exponential function having a lifetime of 336 $\pm$ 16 ms. This lifetime was mainly limited by collisions with background gas atoms. The background pressure of the vacuum was measured to be 5×10^{-10} torr by the ion pump gauge. The ion pump was located 0.75 meters from the atom chip near which the rubidium dispenser is mounted. Hence, the vacuum pressure at the atom chip will be somewhat higher on the order of 1×10^{-9} torr.

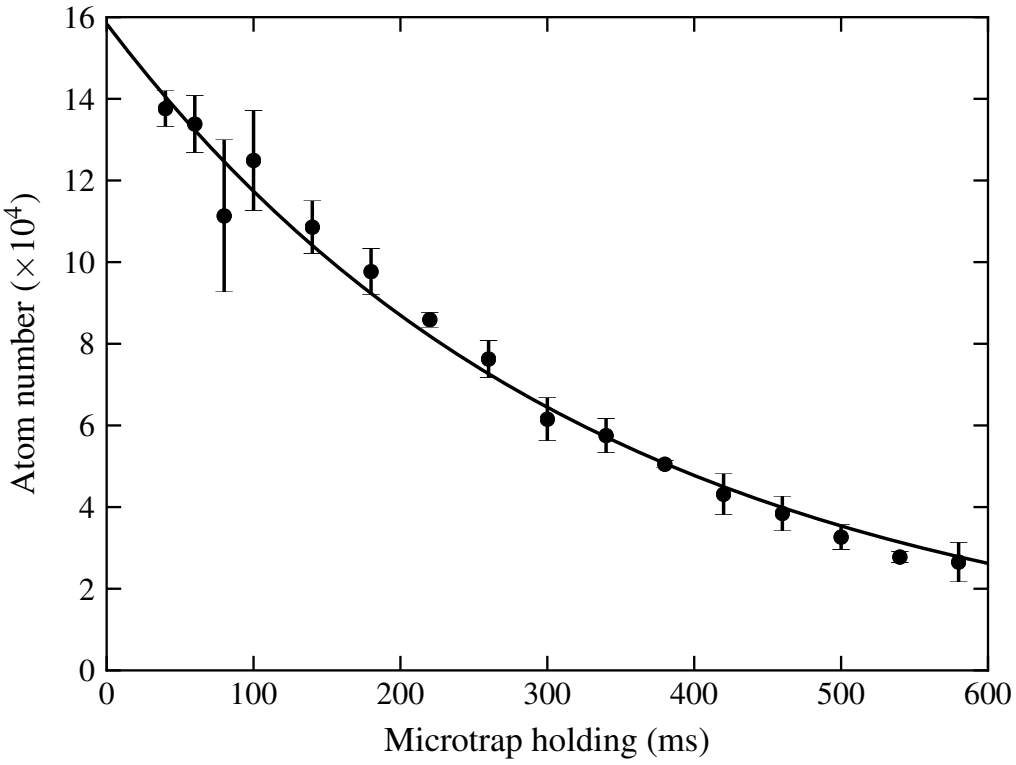

Figure 4.12: Number of atoms in the middle microtrap as a function of the holding time. The exponential decay function fit to the data has a decay time of 336 $\pm$ 16 ms. This data was taken using $B_{\mathrm{zshift}} = 60.8$ G, $B_{\mathrm{yshift}} = 1$ G, $B_{\mathrm{zbias}} = 12.4$ G, a 40 ms loading time and a probe delay of 0.4 ms.

The possibility of atom loss due to Majorana spin flips occurring near the trap center where the magnetic field vanishes was considered [61]. This occurs if Equation 1.24 is violated. For an atom travelling with a velocity v near a trap center where the magnetic field is given by $B = B'y$, spin flips can occur in a sphere centered about the trap minima having a radius

$$b_0 \approx \sqrt{\frac{v\hbar}{\mu_B B'}}. \tag{4.3}$$

For atoms in the microtrap at a temperature of 150 μK, $b_0 \approx 0.5$ μm which is more than two orders of magnitude smaller than the trapped atom cloud. The atom loss rate can be estimated by multiplying the atom cloud density n with the surface area of the sphere of radius b_0 and the atom velocity.

$$\left.\frac{dN}{dt}\right|_{\text{Majorana}} = -n \cdot 4\pi b_0^2 \cdot v \tag{4.4}$$

This expression can be rewritten using Equation 4.3 and estimating the density by dividing the number of trapped atoms N by the volume of the approximately spherical atom cloud having radius σ.

$$\left.\frac{dN}{dt}\right|_{\text{Majorana}} \approx -\frac{N}{\sigma^3}\frac{\hbar v^2}{\mu_B B'} \tag{4.5}$$

The square of the atom velocity can be estimated using the Virial theorem which states that the average kinetic energy equals one half of the average potential energy. For the atom in the trap this yields

$$\frac{1}{2}Mv^2 = \frac{1}{2}\mu_B B'\sigma \tag{4.6}$$

Substituting this result into Equation 4.5 yields

$$\left.\frac{dN}{dt}\right|_{\text{Majorana}} \approx -\frac{\hbar}{M\sigma^2}N \tag{4.7}$$

Thus, the Majorana loss rate equals $\frac{\hbar}{M\sigma^2}$. For an atom cloud having a radius of 150 μm, this loss rate is 3×10^{-2} s^{-1} corresponding to a trap lifetime of over 30 seconds. This is much larger than observed. Majorana transitions were therefore concluded to be negligible.

The atom temperature must be less than the trap depth for the atoms to be trapped. The microtrapped atom cloud shown in Figure 4.7 was created using an atom chip current of 2.6 A which corresponded to a maximum trap depth of over 1 mK. Smaller numbers of trapped atoms were observed using currents as low as 1 A. This indicated the atom temperature is less than a few hundred μK.

Two methods were employed to estimate the atom temperature. The standard technique in the field of ultracold atom research is to suddenly turn off the atom trap and measure the subsequent expansion of the atom cloud as is shown in Figure 4.13. The radius of the expanding cloud as a function of time t is given by the following expression [60].

$$\sigma_y(t) = \sqrt{\sigma_{y0}^2 + \frac{k_{\mathrm{B}} T_y}{M} t^2} \tag{4.8}$$

Here $\sigma_y(t)$ is the radius of the microtrap atom cloud in the y direction, σ_{y0} is the initial radius of the atom cloud and T_y is the temperature which was found to be 160 $\pm$ 6 μK. The temperature could also be estimated by measuring the cloud expansion in the vertical direction. This gave a temperature of 124 ± 29 μK. This result has a larger uncertainty because a number of atoms of the expanding cloud bounced off the atom chip complicating the determination of the cloud radius.

The second method to estimate the temperature was to calculate the average kinetic and potential energies of the microtrapped atom clouds and use the Virial Theorem to find the temperature [84]. Figure 2.3 shows the microtrap potential near the trap center along the y direction was well approximated by a linear function $U(y) = g_F m_F \mu_B B' y$, where y is the position relative to the trap minimum. The density of atoms in one dimension was shown in Figure 4.7 to be well described by a

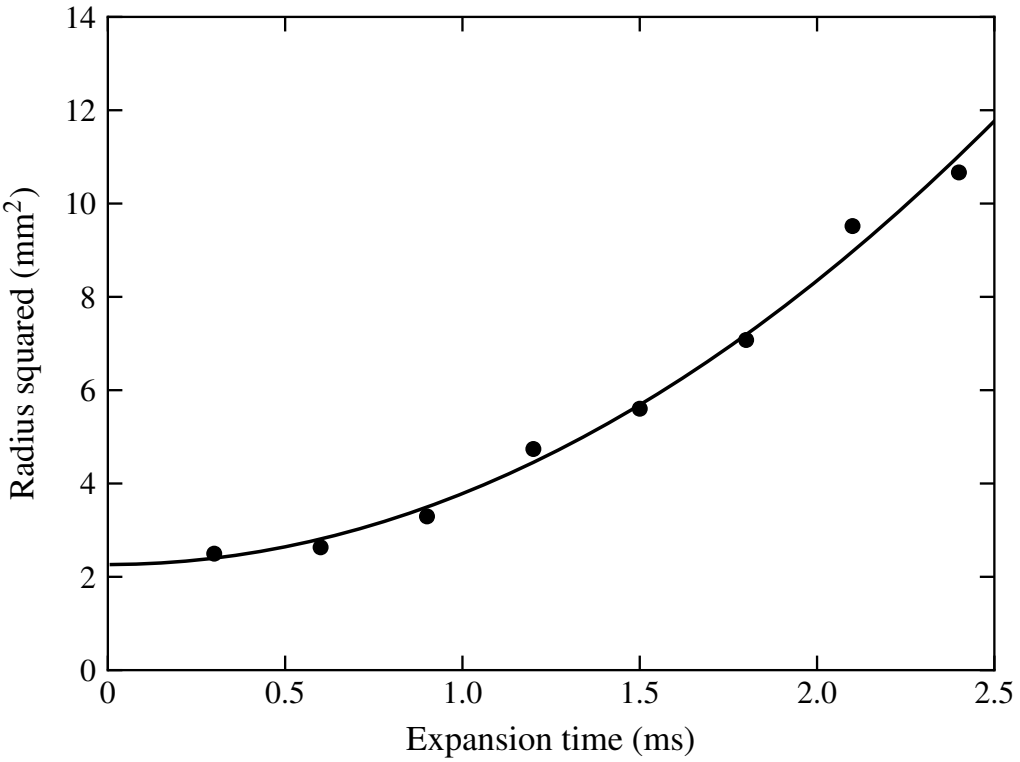

Figure 4.13: Expansion of the atom cloud in the horizontal direction as a function of time after the middle microtrap was turned off. The curve fitted to the data corresponded to an atom temperature of 160 ± 6 μK as described in the text. This data was taken using $B_{\mathrm{zshift}} = 60.8$ G, $B_{\mathrm{yshift}} = 1$ G, $B_{\mathrm{zbias}} = 12.4$ G, a 40 ms loading time and a holding time of 100 ms.

Gaussian function.

$$n(y) = \frac{N_{\text{Tot}}}{\sqrt{2\pi}\sigma} e^{-\frac{y^2}{2\sigma^2}} \tag{4.9}$$

where N_{Tot} is the total number of microtrapped atoms. The average potential energy is given by

$$\begin{aligned} \langle E_{\text{P.E.}} \rangle &= \int_{-\infty}^{\infty} U(y) n(y) d\, y \\ &= 2 g_F m_F \mu_B B' \sigma^2 \end{aligned} \tag{4.10}$$

while the mean kinetic energy is given by

$$\langle E_{\text{K.E.}} \rangle = \frac{1}{2} k_B T N_{\text{Tot}}. \tag{4.11}$$

Using the Virial Theorem result $\langle E_{\text{K.E.}} \rangle = \frac{1}{2} \langle E_{\text{P.E.}} \rangle$ gives an atom temperature

$$T = \sqrt{\frac{2}{\pi}} \frac{g_F m_F \mu_B B' \sigma}{k_B}. \tag{4.12}$$

Substituting the observed atom cloud size in the horizontal direction gave a temperature of 400 μK. This was more than a factor of 2 larger than found using the time of flight technique. This was likely caused by an overestimation of the cloud radius σ. The imaging laser frequency was fixed to be resonant with the $F = 2 \rightarrow F' = 3$ transition of the D2 line. Microtrapped atoms experience magnetic fields and therefore did not absorb the imaging laser. All imaging in this thesis was therefore done by turning off the magnetic traps and waiting typically 0.4 ms before the imaging laser passed through the ultracold atom cloud. The atom cloud size was likely to experience forces when the magnetic fields are abruptly turned off causing the cloud to expand. This will result in an overestimate of the cloud size resulting in a temperature that was too high.

5 Microtrap loading from a mirror MOT

This chapter describes loading the double-loop microtrap from a mirror MOT.

5.1 Experimental configuration and procedure

The apparatus is illustrated in Figure 5.1. It is very similar to Figure 4.1 except the coil assembly was moved upwards so that the point midway between the quadrupole coils was located only 2 mm beneath the atom chip surface. This was done to facilitate creating a mirror MOT from which the atoms could be directly transferred into the microtrap. The quadrupole coils were aligned along the x-axis direction, parallel to the atom chip surface in contrast to the traditional 45° arrangement [34]. The MOT laser beams were incident at 45° in the y-z plane on the atom chip surface as well as along the $\pm x$-axis as shown in Figure 5.1.

In this experiment and the one described in Chapter 6, the atom chip was mounted onto a copper block using thermally conductive epoxy, Epo-Tek H77, instead of being mechanically clamped as in Chapter 4. It was found that the mirror MOT intensity was unstable when the atom chip was clamped onto the copper block.

The timing sequence diagram of the experiment is given in Figure 5.2. Atoms were first collected into the mirror MOT from the background rubidium vapour [34, 38]. This was done using a magnetic field gradient along the x-axis of 14 G/cm. The trap laser beam had an intensity of 47 mW/cm^2 and a beam diameter of about 18 mm. It

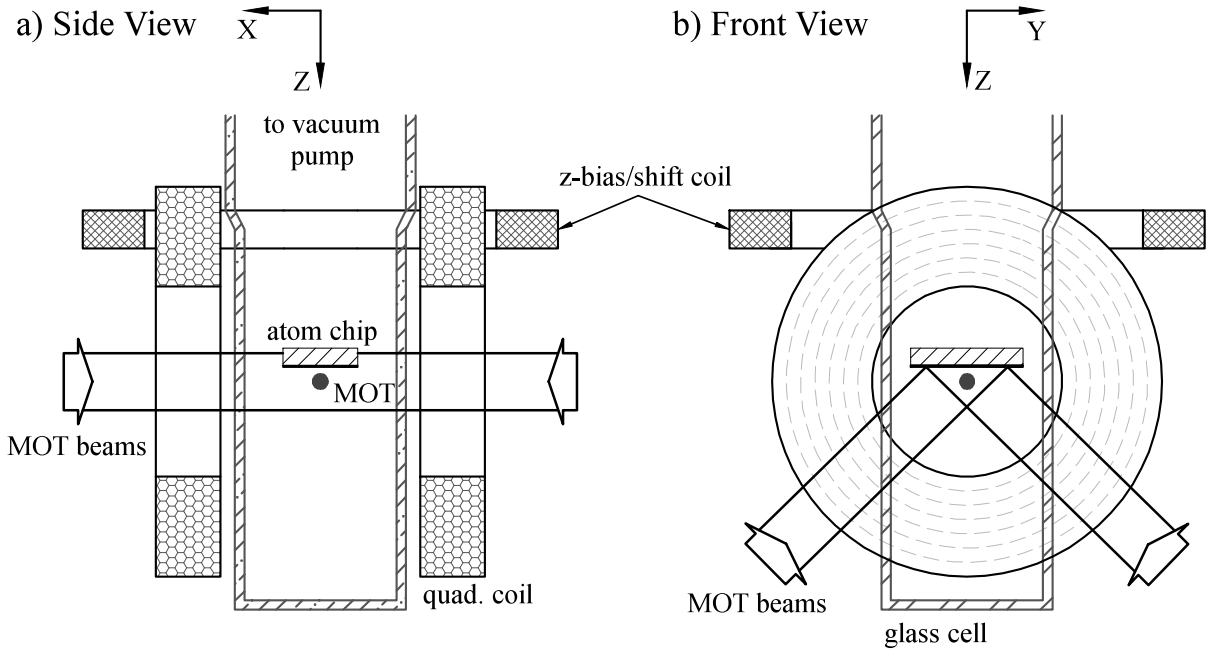

Figure 5.1: Schematic of the apparatus for loading the microtrap from a mirror MOT. The atom chip surface was 2 mm above the point midway between the quadrupole coils. The transverse (x and y) bias coils are not shown for simplicity.

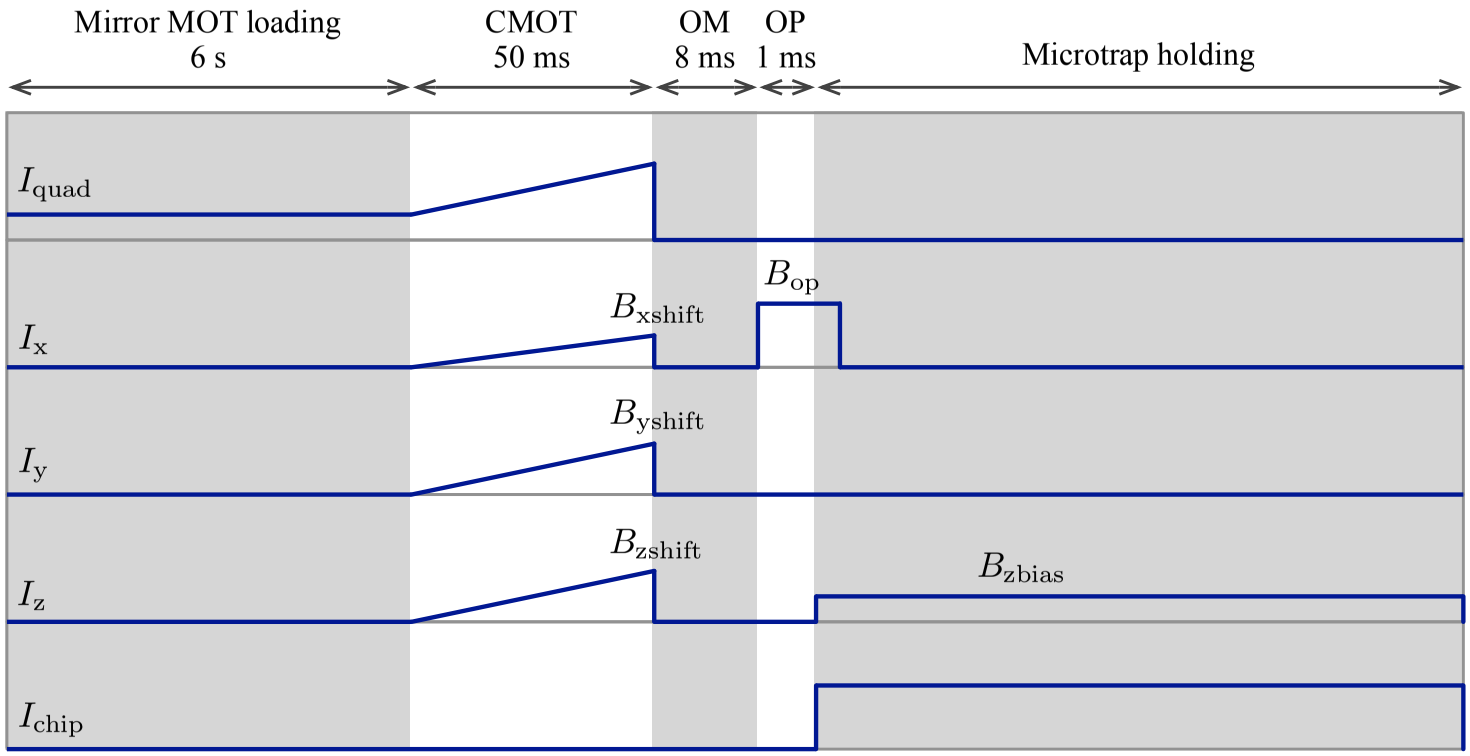

Figure 5.2: Timing sequence of the currents that generate various magnetic fields used to load the microtrap from a mirror MOT. Atoms were first collected in the mirror MOT which was then compressed (CMOT). Next, the atoms were cooled using optical molasses (OM) after which they were optically pumped (OP) to the $|2, 2\rangle$ Zeeman sublevel. The transverse position of the atom cloud was adjusted using fields in the x and y directions and moved in the z direction toward the atom chip so as to overlap the microtrap into which the atoms were transferred.

was divided into two horizontal beams travelling along the x-axis and two angled beams reflected off the atom chip surface as illustrated in Figure 5.1. The power of the trap laser beams incident on the atom chip at 45° was 22.5 mW per beam while that of the beams directed along the $\pm x$ axis was 17 mW per beam. These powers were found to optimize the number of atoms in the mirror MOT [77]. The trap laser beams were circularly polarized and the frequency was red shifted 14 MHz from the D2 cycling transition. The repump laser intensity was 2.4 mW/cm^2. About 3×10^7 atoms were loaded into the mirror MOT in 6 s. The mirror MOT atom cloud had an ellipsoidal shape elongated in the vertical direction. The cloud radii measured in the vertical and horizontal directions were 0.7 and 1 mm, respectively.

The mirror MOT cloud was next compressed (CMOT) by increasing the field gradient to 35 G/cm during a time of 50 ms. At the beginning of the CMOT stage, the trap laser detuning was increased to 30 MHz while the repump laser intensity was reduced to 0.2 mW/cm^2. The alignment of the mirror MOT cloud in the x and y directions with the microtrap array was checked by observing the imaging laser beam reflected off the atom chip surface as was illustrated in Figure 4.5. The atom cloud was positioned directly beneath the middle microtrap by applying fields B_{xshift} and B_{yshift} as is shown in Figure 5.3. The number of atoms was 1.1×10^7 and the CMOT atom cloud was approximately spherical having a radius of 0.5 mm. An additional field $B_{\text{zshift}} = 3.0$ G was applied to position the atom cloud 0.58 mm below the atom chip. Larger B_{zshift} values shifted the CMOT atom cloud closer to the chip surface but many atoms were lost because the distance to the chip surface was less than the cloud radius.

The compressed MOT was next further cooled using optical molasses (OM) and optical pumping (OP) as described in Chapter 4. More than 90% of the atoms could be optically pumped into the $|2, 2\rangle$ Zeeman sublevel. The atom temperature after optical pumping was 60 μK. This was higher than that observed after optical molasses (35 μK) due to heating caused by absorption of the optical pumping light.

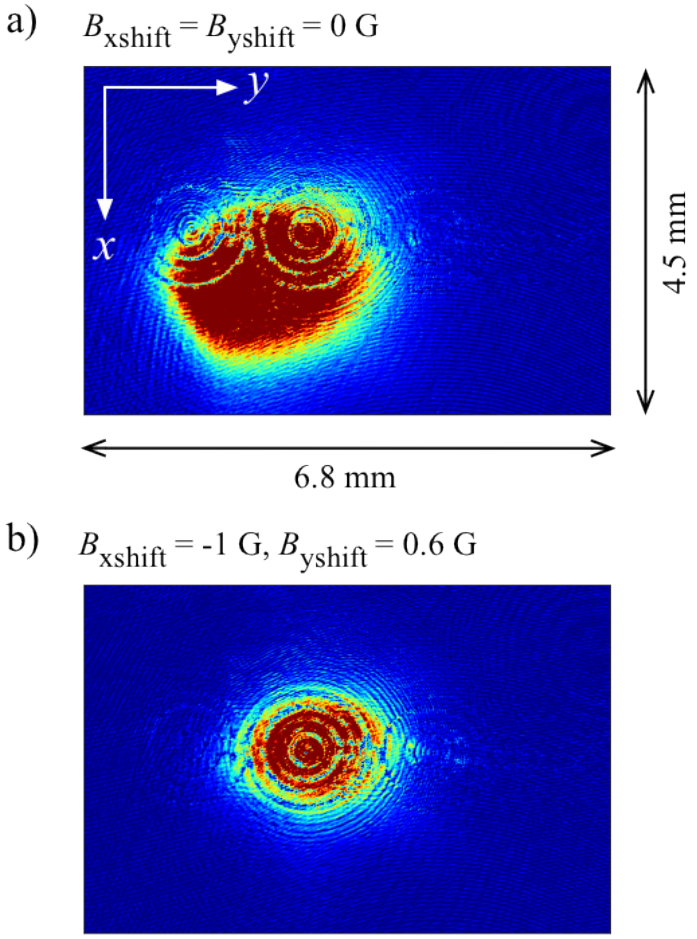

Figure 5.3: Position of the atom cloud after the optical molasses stage (a) without and (b) with small shifting fields B_{xshift} and B_{yshift}. The microwires comprising the left and middle microtraps whose centers are separated by 1.5 mm are clearly visible in (a).

Atoms were transferred into the microtrap by suddenly turning on the atom chip and z-bias currents. The imaging laser probed the microtrap for times between 30 and 600 ms after atoms were loaded into it. The minimum time of 30 ms allowed atoms not loaded into the microtrap to disperse. The number of trapped atoms was unlikely to be reduced significantly during this initial 30 ms due to evaporative cooling since the trap depth which exceeded 1 mK was an order of magnitude greater than the atom's thermal energy $k_{\mathrm{B}}T$ [85].

5.2 Characterization of the microtrap

Only the middle microtrap was loaded in this experiment because the size of the atom cloud was less than the distance between two adjacent microtraps as is shown in Figure 5.3. A sample absorption image of the microtrapped atom cloud is shown in Figure 5.4 corresponding to 1.3×10^5 atoms. A Gaussian function was fit to the optical density as is discussed in Chapter 4. The radii of the atom cloud were found to be 107 ± 1 and 91.5 ± 1.3 μm, in the horizontal and vertical directions, respectively. The peak density of the microtrapped atom cloud was calculated to be 7.8×10^9 atoms/cm^3. The atom temperature was measured to be 107 ± 18 μK using the time of flight method. The lifetime of the microtrapped atoms was observed to be 330 ± 27 ms which agrees with that measured in Chapter 4.

The dependence of the microtrapped atom cloud on B_{zbias} is shown in Figure 5.5. A maximum of 1.5×10^5 atoms could be loaded into the microtrap using a bias field of about 9 G. This number was a factor of 3 higher than that obtained without optical pumping. This is reasonable as only two of the five $F = 2$ Zeeman sublevels were magnetically trapped. Hence, optical pumping should increase the number of trapped atoms by a factor of 5/2. This crude estimate assumes all Zeeman sublevels were equally populated after the optical molasses which was unlikely to be the case. A reduction of the atom number of about 30% occurred when $B_{\mathrm{zbias}} \approx 7$ G. This is believed to arise due to Majorana spin flips from the magnetically trapped Zeeman

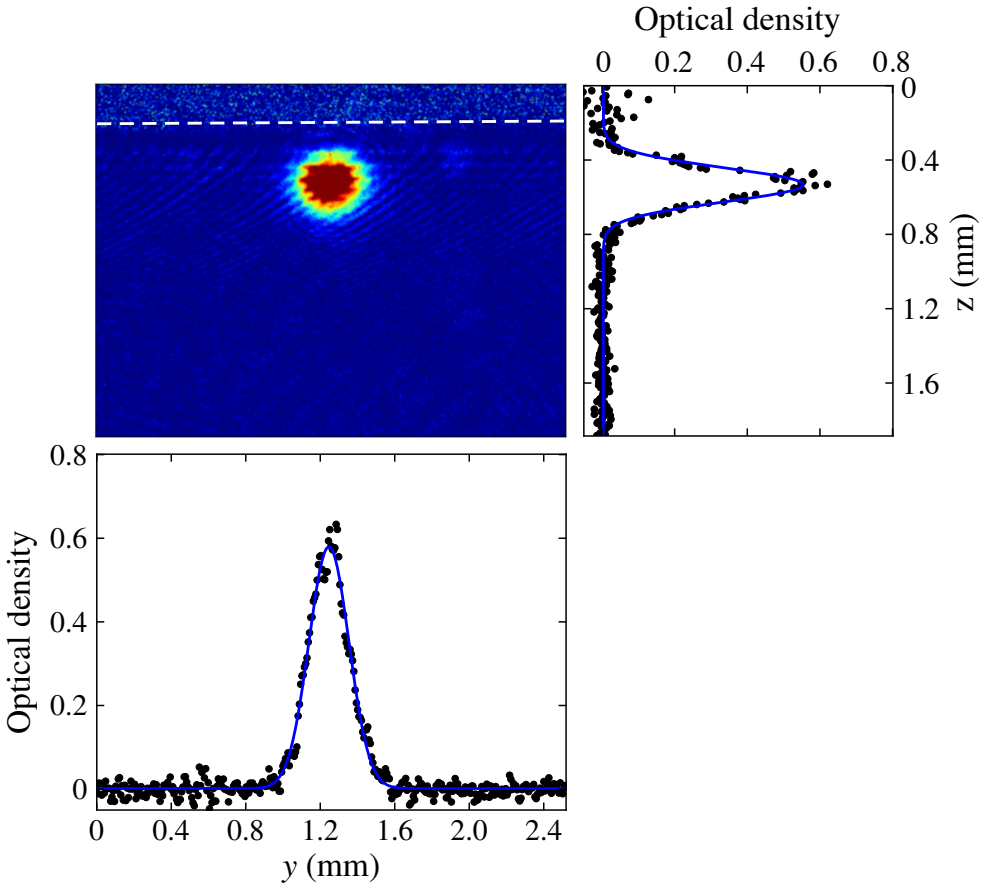

Figure 5.4: Sample absorption image of the microtrapped atom cloud with the optical density plotted along the y and z directions through the center of the atom cloud. This data was taken using a chip current of 2.6 A and a bias field $B_{\mathrm{zbias}} = 3$ G. The white dashed line indicates the atom chip surface. The blue curves are Gaussian functions fit to the data. This image was observed 40 ms after the microtrap was turned on with a probe delay of 0.4 ms.

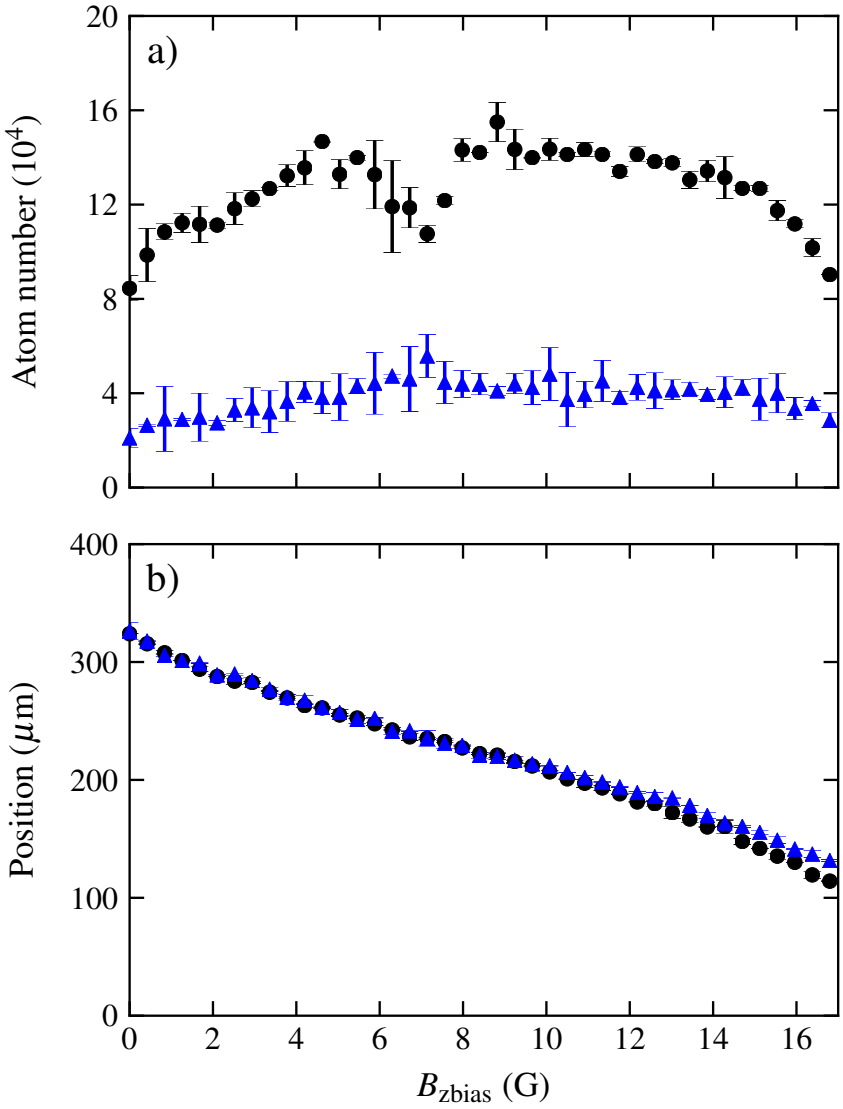

Figure 5.5: Dependence of (a) the number of atoms and (b) the position of the middle microtrapped atom cloud as functions of B_{zbias}. Solid black dots and blue triangles are the data with and without optical pumping applied after the optical molasses, respectively. All the data was taken using an atom chip current of 2.6 A. The atom cloud was probed 40 ms after the microtrap was turned on using a probe delay of 0.4 ms.

sublevels to non-trapped sublevels. The Majorana spin flips can occur near the center of the microtrap where the magnetic field was zero as was discussed in Chapter 4. The atom number also decreased for $B_{\mathrm{zbias}} > 13$ G which agreed with the numerical simulation results of Chapter 2.

Figure 5.5(b) shows the microtrapped atom cloud position as a function of B_{zbias}. The position of the atom cloud was nearly independent of optical pumping. The bias field could control the position of the microtrapped atom cloud over a range of 100 to 300 μm. The numerical simulation of the microtrapped cloud center was not shown as it agreed very closely with the observations as was the case in Chapter 4.

Figure 5.6 shows the number of atoms loaded into the middle microtrap as a function of the atom chip current, I_{chip}. Each of these points was taken using a B_{zbias} field generated by a current $I_{\mathrm{zbias}} = 0.3\ I_{\mathrm{chip}}$ ($B_{\mathrm{zbias}}(\mathrm{G}) = 4.2\ I_{\mathrm{zbias}}(\mathrm{A})$). The largest number of microtrapped atoms occurred when $I_{\mathrm{chip}} = 2.6$ A. Fewer atoms were trapped at lower currents which is not surprising since the trap depth is proportional to the chip current. For currents $I_{\mathrm{chip}} > 2.6$ A, the number of trapped atoms decreased. This occurred because the trap volume gets smaller. From Figure 2.3, one finds the size of the microtrapped cloud for atoms of a given energy is approximately inversely proportional to the trap depth. Hence, a doubling of the chip current from 2.6 to 5.2 A will reduce the trap volume by about a factor of 8. This in turn reduced the number of atoms that could be loaded into the microtrap.

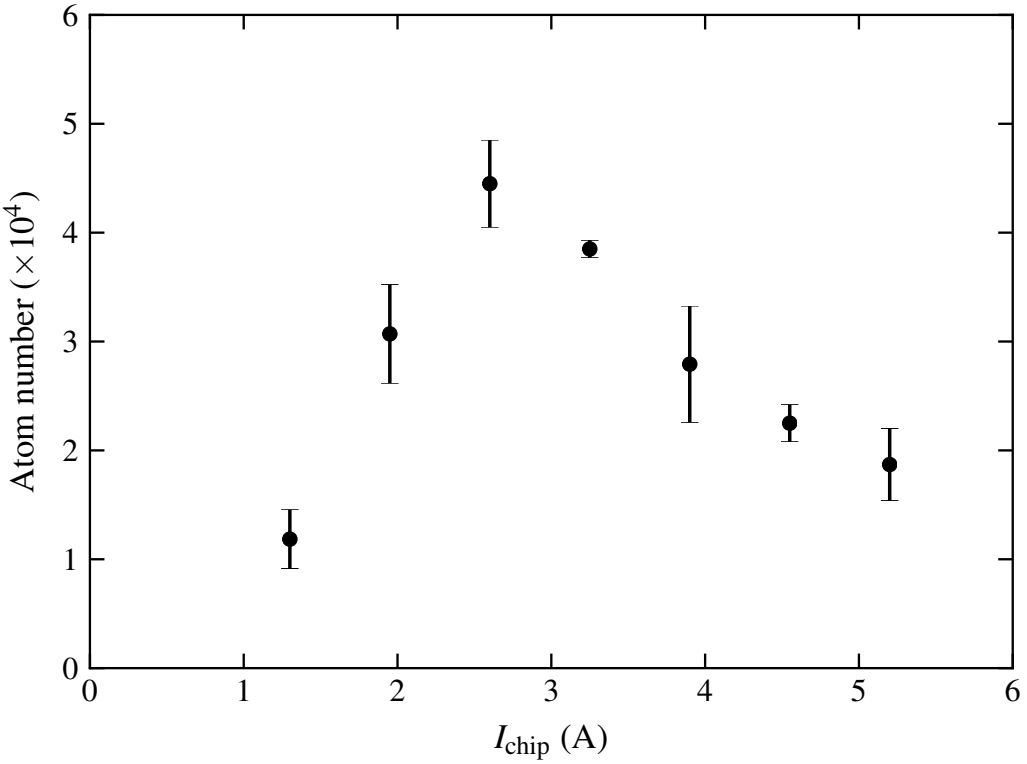

Figure 5.6: Dependence of the number of atoms in the middle microtrap on the atom chip current I_{chip}. The data were taken using $I_{\mathrm{zbias}} = 0.3 I_{\mathrm{chip}}$. The maximum number of trapped atoms was about 1/3 of that shown in Figure 5.5 because the mirror MOT was not optimal. The atom cloud was probed 40 ms after the microtrap was turned on using a probe delay of 0.4 ms.

6 Microtrap array loading from a far off resonant optical dipole trap

This chapter describes loading the microtrap array from a FORT. Atoms were initially loaded into the FORT from a mirror MOT.

6.1 Experimental configuration and procedure

The apparatus and procedure to load atoms into the microtrap array are shown in Figures 6.1 and 6.2. Ultracold atoms were first generated using a mirror MOT as described in Chapter 5. Next, an infrared laser was used to generate a FORT. The FORT laser beam travelled beneath the atom chip surface along the axis of the microtrap array. The distance between the FORT laser and the atom chip surface could be adjusted from 150 to 350 μm by slightly varying the vertical position of the lens used to focus the FORT laser beam. The laser focus was positioned under the middle microtrap. This was checked using the vertical imaging system described in Chapter 4. The FORT laser beam had a maximum power P of 14 W that could be focussed to give a focal spot having a radius w_0 measured to be 35 μm. The trap depth at the FORT focus for the linearly polarized laser is given by

$$U_0 = \frac{\hbar\gamma^2}{24 I_s} \frac{P}{\pi \mathrm{w}_0^2} \left(\frac{1}{\delta_{1/2}} + \frac{2}{\delta_{3/2}} \right) \tag{6.1}$$

where $\gamma = 2\pi \times 6.1$ MHz for the D2 line, $I_s = 1.6$ mW/cm^2 is the saturation intensity and $\delta_{1/2}$ and $\delta_{3/2}$ are the detunings of the 1064 nm laser from the D1 and D2

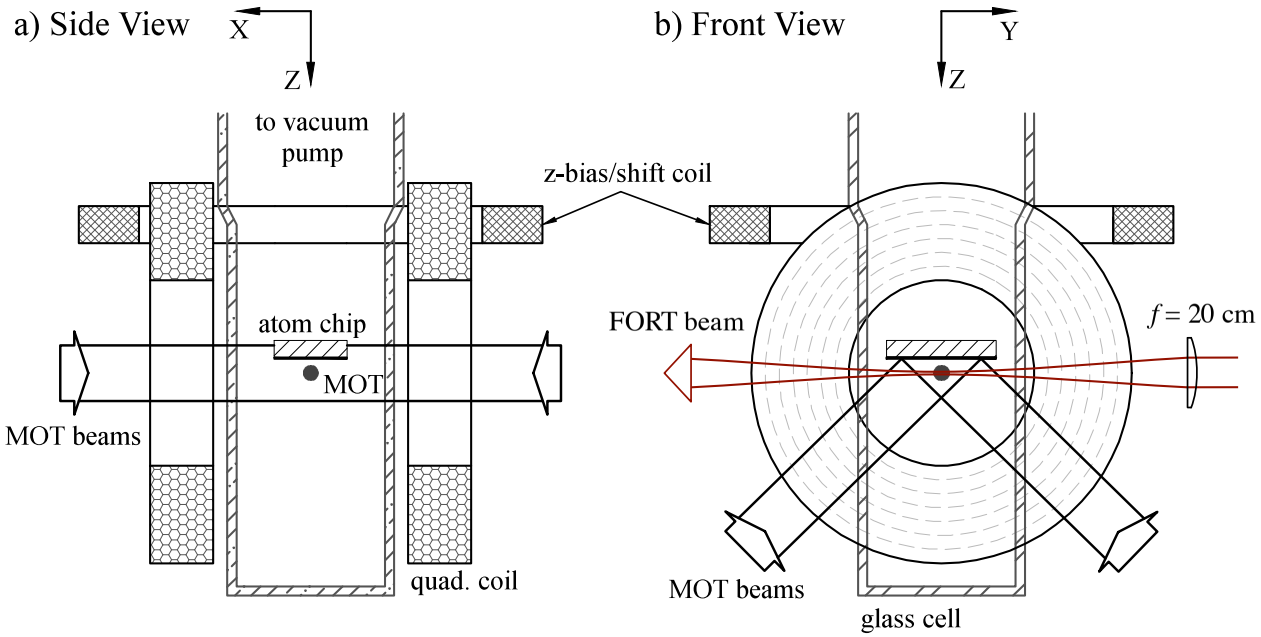

Figure 6.1: Schematic of the apparatus for loading the microtrap array from a FORT. The FORT laser beam travelled along the microtrap array axis. Its position below the atom chip could be adjusted between 150 and 350 μm.

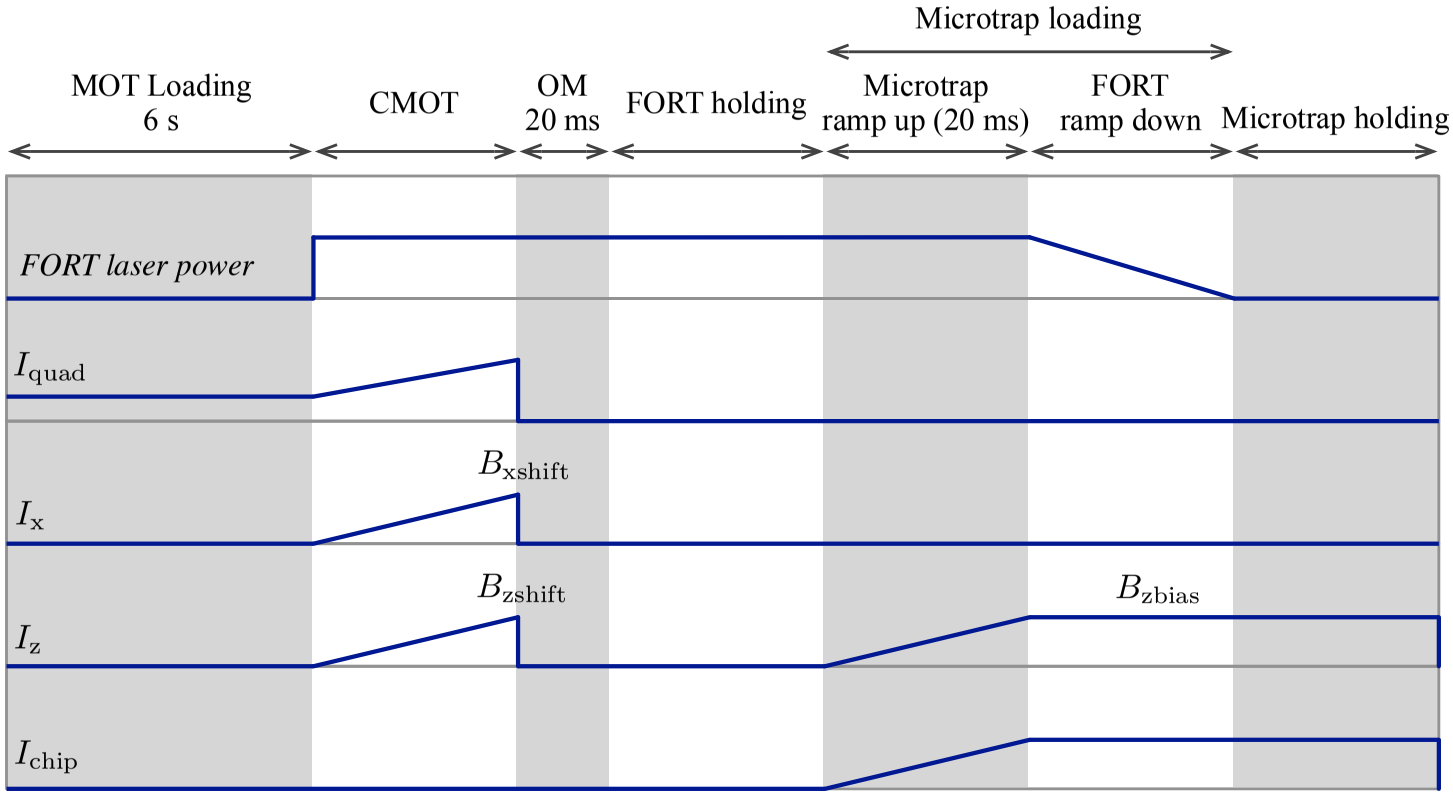

Figure 6.2: Timing sequence of the FORT laser power and the currents used to generate various magnetic fields for loading the microtrap array from a FORT. Atoms were first collected in the mirror MOT which was then compressed (CMOT). Next, the atoms were cooled using optical molasses (OM). The FORT laser power was ramped down after the atom chip current used to create the microtrap had been turned on.

transitions, respectively. The maximum trap depth was just over 1 mK.

6.2 FORT loading results

After atoms were loaded for 6 s in the mirror MOT, the MOT was compressed and the FORT laser was turned on. The parameters of the CMOT were the same as described in Chapters 4 and 5. The only difference was that the repump laser intensity was reduced to 27 μW/cm^2. This has been found to optimize the transfer of atoms from a MOT into a FORT [25, 86, 87, 88]. For example, the lower repump laser intensity increased (reduced) the number of atoms in the lower $F = 1$ ($F = 2$) ground state hyperfine level. Collisions between atoms in the different ground state hyperfine levels were therefore reduced. Such collisions can change the hyperfine level which increases the atom's kinetic energy by an amount equal to the difference of the $F = 1$ and $F = 2$ ground state hyperfine level energies [86].

FORT loading was also optimized by applying magnetic fields, B_{xshift} and B_{zshift}, in the x and z directions respectively, to overlap the mirror MOT with the FORT laser beam that was directed along the microtrap array oriented along the y-axis. A shifting field in the y direction was not necessary because the size of the FORT along the y direction is comparable to the distance between the left and right microtraps. After the CMOT phase, atoms were cooled for 20 ms using optical molasses.

The low repump laser intensity ensured that atoms loaded into the FORT occupied the $F = 1$ ground state hyperfine level. Alternatively, atoms could be prepared in the $F = 2$ hyperfine level by turning off the trap laser 1 ms before the end of the optical molasses and simultaneously increasing the repump laser intensity to 0.5 mW/cm^2. Atoms in the FORT occupying the $F = 2$ ground state hyperfine level were resonant with the imaging laser. Atoms occupying the $F = 1$ ground state hyperfine level were detected by overlapping the imaging laser beam with part of the repump laser beam. Figure 6.3 shows a typical FORT having 8.5×10^5 atoms in the $F = 1$ ground state hyperfine level. This signal was reduced by nearly two orders of magnitude when the

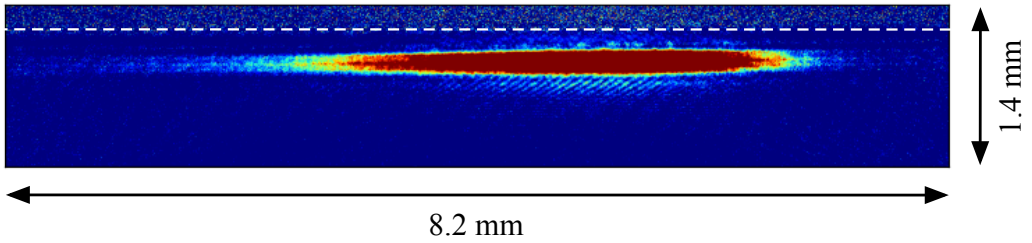

Figure 6.3: Typical FORT having 8.5×10^5 atoms occupying the $F = 1$ ground state hyperfine level. The FORT had an ellipsoidal shape extending a distance of 1.96 $\pm$ 0.01 mm in the horizontal y direction and had a diameter of 128 $\pm$ 6 μm along the vertical axis. The distance between the FORT and the atom chip surface indicated by the white dashed line, was 300 $\pm$ 15 μm. The FORT was probed 40 ms after the optical molasses phase with a probe delay of 0.2 ms.

repump laser that was combined with the imaging laser, was blocked. Hence, it could be concluded that greater than 98% of the FORT atoms were in the $F = 1$ ground state hyperfine level after the optical molasses phase. Similarly, a FORT could be generated having nearly one million atoms with over 98% in the $F = 2$ ground state hyperfine level.

Figure 6.4 shows the temporal dependence of the number of atoms loaded into the FORT in the $F = 1$ ground state hyperfine level. The loading rate is described by [86]

$$\frac{dN}{dt} = R_0 \exp\left(-\gamma_{\mathrm{MOT}} t\right) - \Gamma_{\mathrm{L}} N - \beta_{\mathrm{L}} N^2. \tag{6.2}$$

where R_0 is the loading rate at time $t = 0$, γ_{MOT} is the rate at which the MOT loses atoms that depends on the trap laser detuning and repump intensity, Γ_{L} describes loss due to collisions with background gas atoms and β_{L} describes loss due collisions between ultracold atoms. The numerical solution of the above equation was fitted to the data yielding $R_0 = 1.95 \times 10^7$ s^{-1}, $\gamma_{\mathrm{L}} = 2.79$ s^{-1}, $\Gamma_{\mathrm{L}} = 8 \times 10^{-7}$ s^{-1} and $\beta_{\mathrm{L}} = 1.47 \times 10^{-5}$ s^{-1}. A maximum number of $\sim 9.6 \times 10^5$ atoms could be loaded into the FORT in 135 ms. Dividing this number by the FORT's ellipsoidal volume gives a peak density of 1.3×10^{10} cm^{-3}. A similar number of atoms occupying the $F = 2$ ground state hyperfine level could be loaded into the FORT. This number compares to 1.4×10^7 atoms that are in the CMOT with the FORT laser blocked. Hence, the atom transfer efficiency into the FORT from the CMOT was about 7% which is comparable with that obtained by other groups [86, 87, 89].

The lifetime of the atoms in the FORT was found to be slightly less than 1 s by fitting an exponential function to the data shown in Figure 6.5. These measurements were taken with all lasers, except the FORT laser, blocked using mechanical shutters. This was critical as a very low power of resonant light heats the atoms significantly reducing the lifetime. The atom temperature was found by switching off the FORT laser and using the time of flight method. The temperature for atoms in the $F = 1$

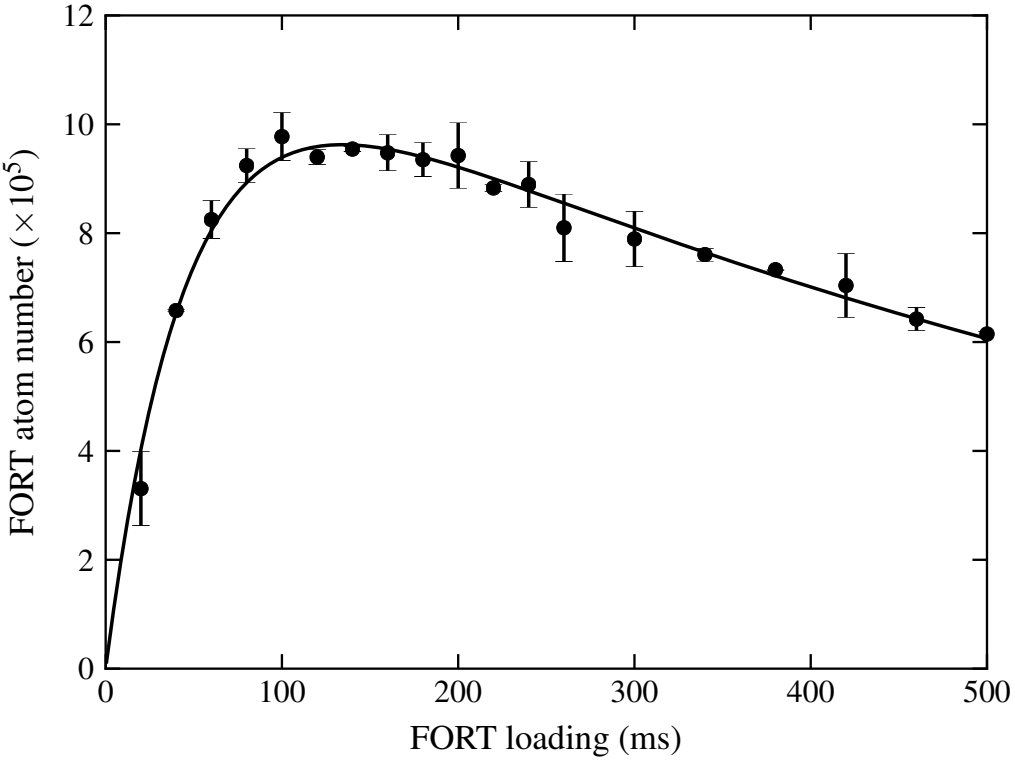

Figure 6.4: Dependence of the number of FORT atoms in the $F = 1$ ground state hyperfine level on loading time. This data was taken with both the CMOT and FORT on. The curve fitted to the data is described in the text.

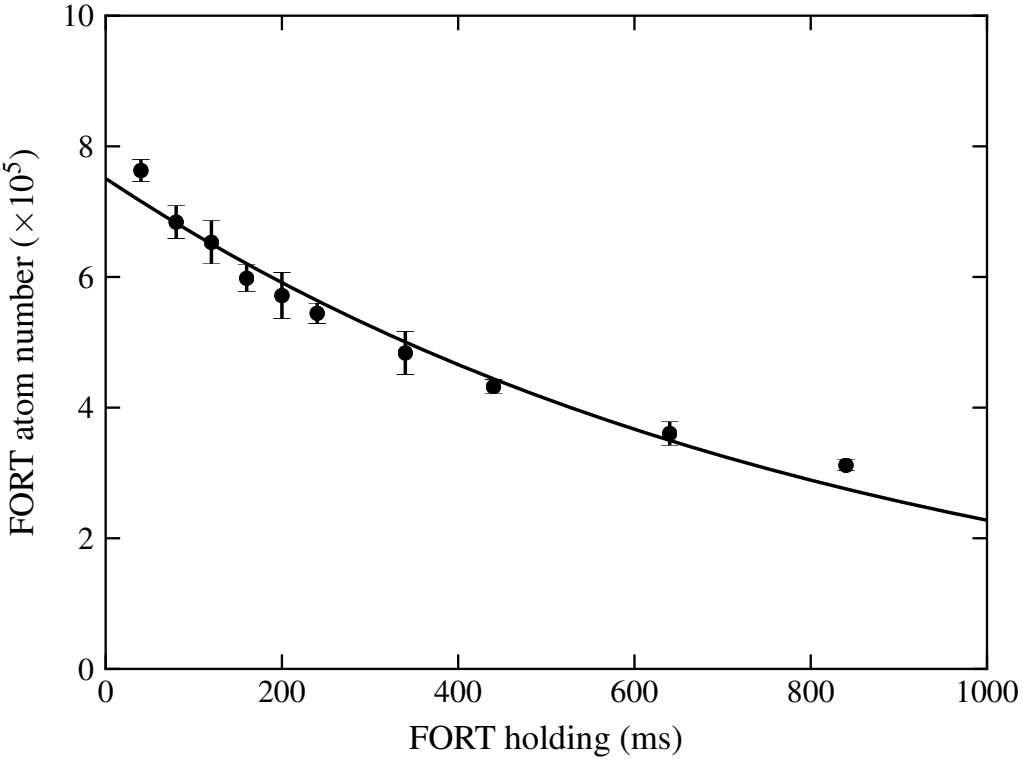

Figure 6.5: Number of atoms in the FORT as a function of the FORT holding time. The fitted exponential decay curve has a lifetime of 840 ± 60 ms.

($F = 2$) hyperfine level was found to be 330 $\pm$ 15 (230 $\pm$ 15) μK. The higher temperature for the $F = 1$ hyperfine level can be explained by heating caused by the repump laser during imaging.

6.3 Characterization of the microtrap array

The microtrap array was turned on by linearly ramping up the chip current to 2.6 A and the z-bias field B_{zbias} in 20 ms. Next, the FORT laser power was decreased. Atoms could be loaded into the microtrap in either the $F = 1$ or $F = 2$ ground state hyperfine levels. Figure 6.6 shows a typical image of the microtrapped atoms occupying the $F = 1$ loaded using a FORT ramp down time of 40 ms. The microtrap array was imaged 20 ms after the FORT laser was ramped down. The microtrap array was then switched off for 0.4 ms before the imaging laser pulse arrived. The atom clouds in the three microtraps were analyzed by fitting Gaussian functions to the optical density profiles. All three microtraps had the same radius of 105 $\pm$ 5 μm. The number of atoms in the left, middle and right microtraps were 3.4×10^4, 6.8×10^4 and 2.2×10^4 respectively corresponding to peak densities of 3.0×10^9, 6.0×10^9 and 1.9×10^9 atoms/cm^3.

Figure 6.7 shows the dependence of the number of atoms in the $F = 1$ hyperfine level in the middle microtrap as a function of the FORT ramp down time. Very few atoms were loaded into the microtrap if the FORT laser was abruptly shut off. The optimum number of about 6.5×10^4 atoms was loaded using a ramp down time of 100 ms. The number of trapped atoms became smaller when longer ramp down times were used. This is to be expected due to the finite lifetime of atoms in the microtrap.

Figure 6.8 shows the effect of the z-bias field, B_{zbias}, on the number of atoms in the middle microtrap. More atoms in the $F = 1$ hyperfine level were loaded into the microtrap than in the $F = 2$ level. This difference is plausible because the two hyperfine levels have different numbers of Zeeman sublevels. For the $F = 1$ hyperfine

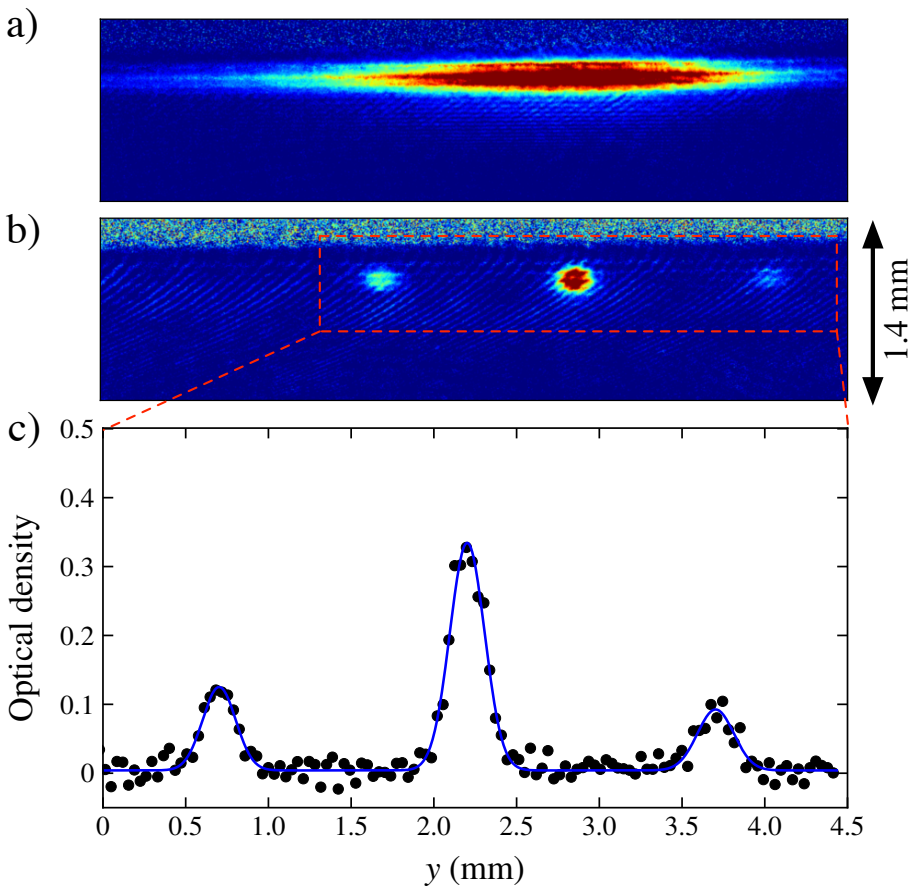

Figure 6.6: Absorption images of atoms trapped in (a) the FORT and (b) the microtrap array. The FORT was located about 220 μm below the atom chip surface. The microtrap array was generated using $I_{\text{chip}} = 2.6$ A and $B_{\text{zbias}} = 3$ G. The image shown in (b) was taken with a FORT ramp down time of 40 ms, a microtrap holding time of 20 ms and a probe delay of 0.4 ms. Populations of 3.4, 6.8 and 2.2×10^4 atoms were in the left, middle and right microtraps, respectively. (c) shows the optical density plotted versus the horizontal direction through the center of the microtraps for the dashed box. Each point is averaged over 5 neighboring pixels. The blue curve is the sum of three Gaussian functions fitted to the data.

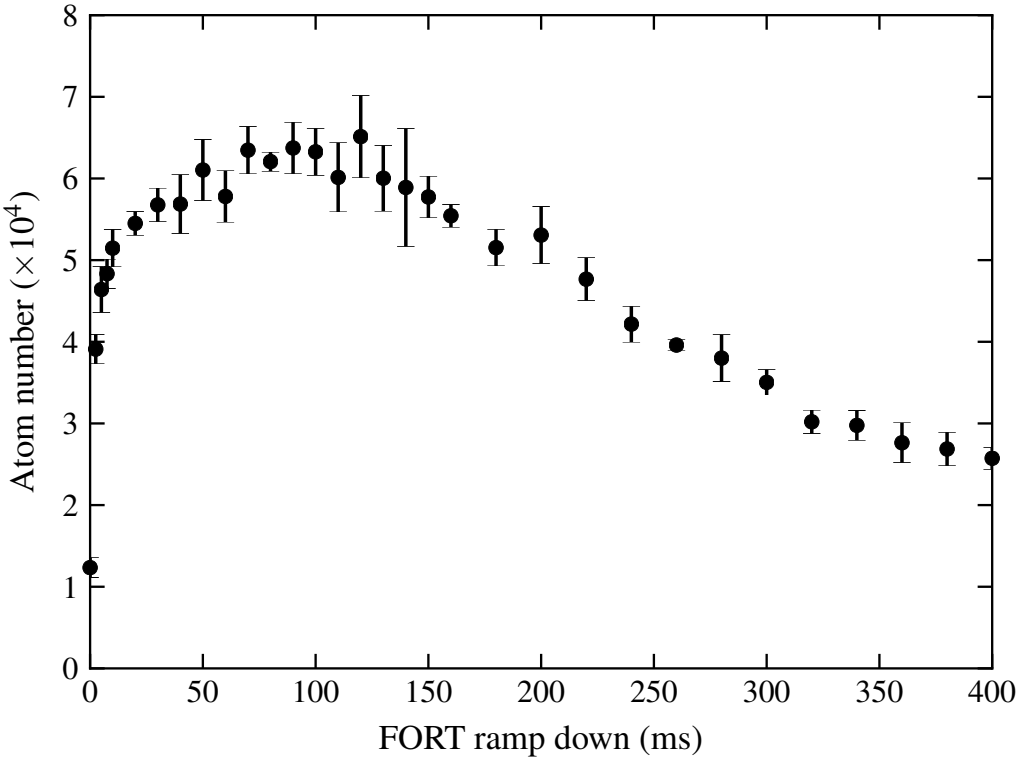

Figure 6.7: Number of atoms in the middle microtrap as a function of the FORT ramp down duration for atoms in the $F = 1$ hyperfine level. The microtrap array was generated using $I_{\text{chip}} = 2.6$ A and $B_{\text{zbias}} = 3$ G. The atom cloud was probed 20 ms after the FORT laser waas ramped down with a probe delay of 0.4 ms.

level, only 1/3 of the Zeeman sublevels, $|1,-1\rangle$, can be magnetically trapped[1]. For the $F = 2$ hyperfine level, two of the five Zeeman sublevels can be trapped but the trap is deepest for the $|2,2\rangle$ sublevel. The sublevel populations in this FORT were equal as this optical trap was independent of the atom's Zeeman sublevel. Therefore, if the FORT has a similar number of atoms in either hyperfine level, one would expect the number of microtrapped atoms in the $F = 1$ hyperfine level to be more than the corresponding number in the $F = 2$ hyperfine level by a factor of 5/3. This agrees with the data. Figure 6.8 also shows the fewest atoms were loaded into the microtrap at zero B_{zbias}. This occurs because the trap depth is smallest without a bias field and the microtrap position at 300 μm did not overlap well with the FORT focus located 220 μm below the atom chip surface.

The microtrap position shifted closer to the FORT and the number of microtrapped atoms increased at higher values of B_{zbias}. However, at a 5 G B_{zbias} field, the number of microtrapped atoms was significantly reduced. The microtrap position below the atom chip for this bias field overlapped the FORT. The dashed line in Figure 6.8(b) indicates the position of the maximum FORT laser beam intensity. Loading the microtrap array was studied using three different FORT positions: 187, 220 and 350 μm below the atom chip surface. For each of the three FORT positions considered, a reduction in the microtrapped atom number of about 50% occurred at the bias field corresponding to overlap of the microtrap and the FORT. This reduction of the microtrapped atom number is due to Majorana spin flips that occur near the microtrap center. Trap loss was therefore maximized when the microtrap and FORT trap centers overlapped. Hence, atoms spend more time near the microtrap center increasing the rate of Majorana spin flips resulting in a reduced number of microtrapped atoms [61]. Figure 6.8(b) shows the microtrap position can be precisely adjusted using the bias field. The atom cloud approached the atom chip surface as

[1]The Landé g factor for $F = 1$ and $F = 2$ hyperfine levels of ^{87}Rb $5S_{1/2}$ ground state are $-\frac{1}{2}$ and $\frac{1}{2}$, respectively.

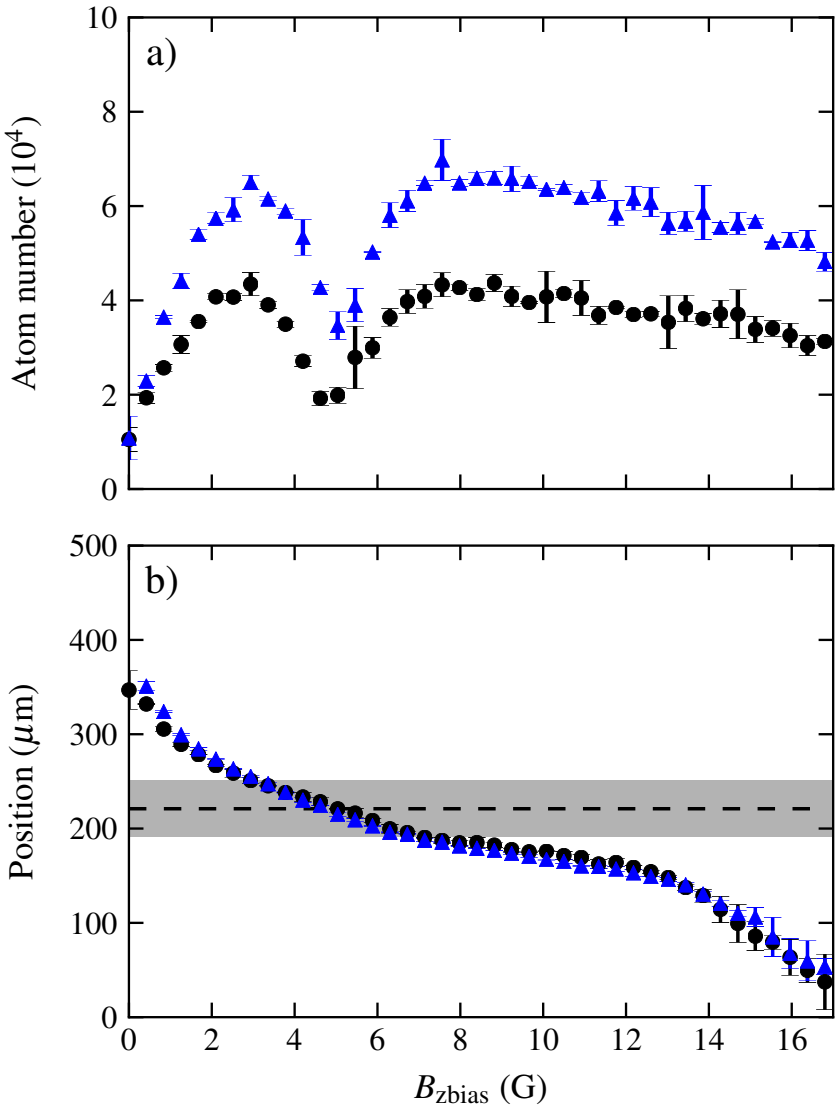

Figure 6.8: Dependence of (a) the number of atoms and (b) the position of the middle microtrapped atom cloud (b) on B_{zbias}. Atoms were loaded in either the $F = 1$ (blue triangles) or $F = 2$ (black dots) hyperfine levels. The FORT ramp down time was 50 ms. All data were taken using an atom chip current of 2.6 A and a microtrap holding time of 20 ms. The time between when the microtrap was turned off and the arrival of the imaging pulse was 0.4 ms. The dashed line in (b) shows the position of the maximum FORT laser beam intensity I_{max} while the grey region is where the FORT laser intensity exceeds I_{max}/e^2.

B_{zbias} increased. The minimum observed distance between the microtrapped atom cloud and the atom chip surface was less than 50 μm.

The lifetime of the microtrapped atoms was studied by imaging the atoms as a function of the microtrap holding time as is shown in Figure 6.9. The same lifetime of 350 ± 15 ms was found for microtrapped atoms in either the $F = 1$ or 2 levels. The atom temperature was determined using the time of flight method. It was studied for different FORT ramp down times as shown in Figure 6.10. The microtrap atom temperature of about 35 μK was nearly an order of magnitude lower than that achieved in the FORT. This result was unaffected by the FORT ramp down times less than 350 ms. This shows that the ultracold atoms of the FORT are preferentially loaded into the microtrap. The decrease of atom temperature to 20 μK at long ramp down times may be due to evaporative cooling [67, 68].

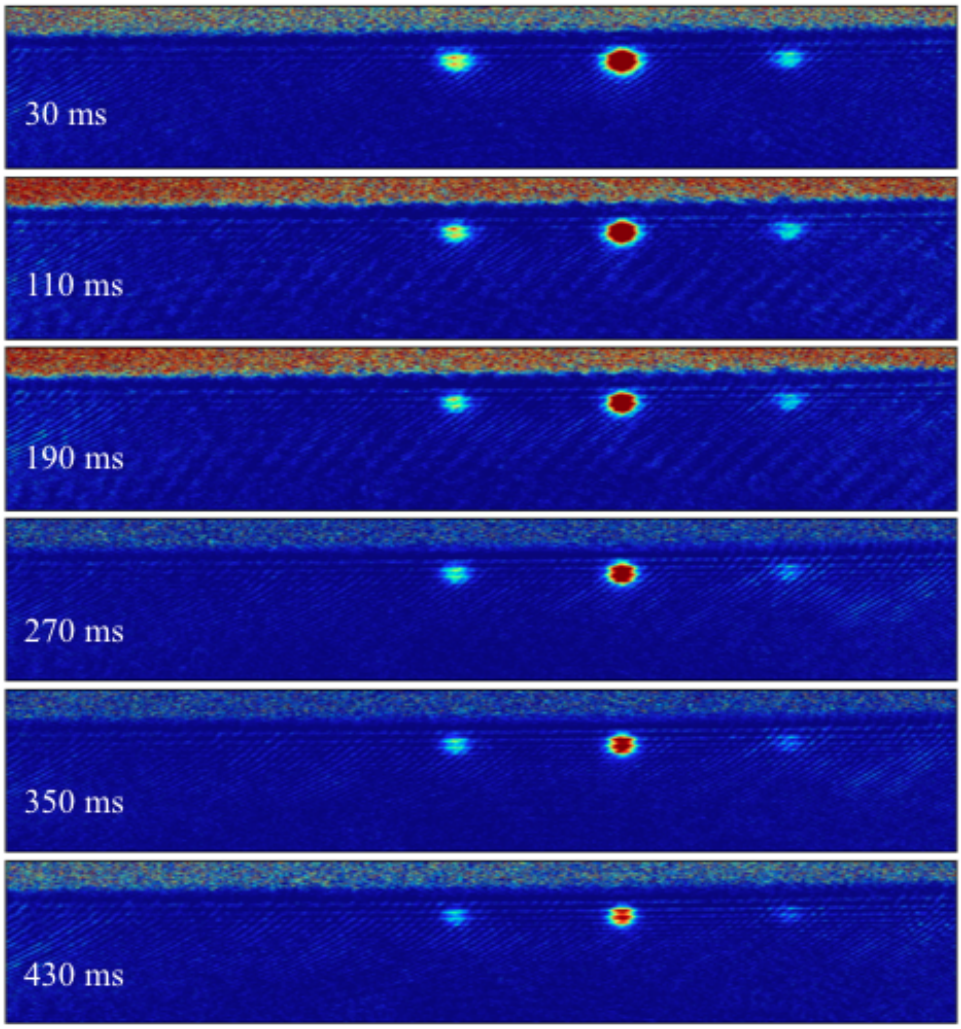

Figure 6.9: Time evolution of the microtrapped atoms in the $F = 1$ hyperfine level versus the microtrap holding time labeled in each image.

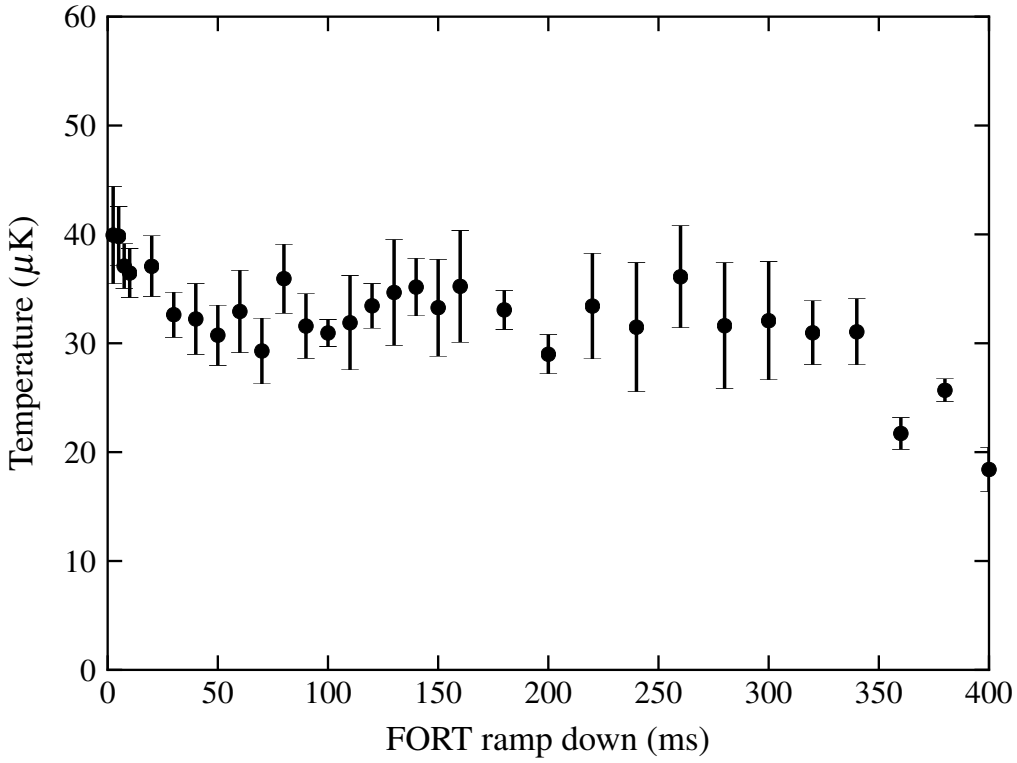

Figure 6.10: Temperature of atoms in the middle microtrap as a function of the FORT ramp down duration for atoms in the $F = 1$ hyperfine level. The data was taken using $I_{\text{chip}} = 2.6$ A and $B_{\text{zbias}} = 3$ G. The atom cloud was probed 20 ms after the FORT laser had ramped down and using a probe delay of 0.4 ms. The error bar of each point was the standard deviation of at least 4 measurements from the mean value.

7 Conclusions

This work successfully demonstrated a new microtrap. Over 10^5 ^{87}Rb atoms were loaded into it at a temperature as low as tens of μK above absolute zero. The trapped atom lifetime was about 350 ms. The double-loop microtrap required a current of only 2.6 A which is an order of magnitude lower than needed by conventional magnetic traps that use macroscopic coils. Moreover, unlike the "Z" and "U" microtraps, it does not require a bias field to trap the atoms although the trap depth can be increased using a bias field. Double-loop microtraps could also be linked in series to create a one dimensional array of microtraps.

Three different techniques were developed to load the microtrap array which are compared in Table 7.1. The technique whereby atoms were first laser cooled using a MOT and then transported using a quadrupole magnetic trap (QMT) to the chip produced the largest number of microtrapped atoms. The atom density, however, was lower than obtained using the other methods. This method also has the important advantage of not requiring the chip surface to be a highly reflective mirror which would allow the study of ultracold atoms interacting with a nonreflective surface. The procedure for this technique is more complex than using a mirror MOT and the magnetic transport of the atoms increased the atom temperature. Loading the microtrap using a mirror MOT required the simplest procedure. However, only one microtrap was loaded because the mirror MOT cloud overlapped a single microtrap. The addition of a FORT to the mirror MOT allowed all three microtraps to be loaded. This is to be expected as the FORT laser propagation direction was aligned with the microtrap array.

Table 7.1: Comparison of loading methods. The total atom number is the sum of all three microtrap populations. The microtrap lifetime obtained using FORT loading is the average of the results obtained using atoms in the $F = 1$ and $F = 2$ ground state hyperfine levels.

	MOT + Transported QMT	Mirror MOT	Mirror MOT + FORT
Number Microtraps Loaded	2	1	3
Atom Number (10^4)	21 ± 1.5	15 ± 1	12 ± 1
Maximum Density ($10^9/\text{cm}^3$)	3.4 ± 0.3	7.8 ± 0.8	9.3 ± 0.9
Temperature (μK)	140 ± 18	82 ± 10	35 ± 5
Lifetime (ms)	336 ± 16	340 ± 20	350 ± 15

Moreover, the temperature of the microtrapped atoms was much lower than found using the other two loading techniques. The attainment of a lower atom temperature using FORT loading of a microtrap has also been found in loading a "Z" microtrap [65]. An important parameter to optimize the microtrap loading was the position of the microtrap relative to the FORT or mirror MOT. The number of trapped atoms was reduced by half when the FORT overlapped the microtrap. Fortunately, the microtrap position could be varied by applying the bias field to spatially shift the microtrap and avoid overlapping the FORT.

The microtrap array has significant future potential. It would be interesting to reduce the size of the microtrap. A reduction of the inner loop radius by a factor of 5 to 60 μm would allow 11 microtraps to fit into the distance occupied by the 3 microtraps in our present atom chip. It would be easier to load similar numbers of atoms into more closely spaced adjacent microtraps. The trap depth scales as the current divided by r_1. Hence, a 5 times smaller microtrap would only require 1/5 the current to achieve the same trap depth. The heat dissipation power equals the square of the current times the resistance. The overall power dissipated by the atom chip would not change assuming the microwire thickness is also reduced by a factor of 5. It is reasonable to expect that the total number of atoms loaded into an array would be the same. However, the number of atoms in each smaller microtrap is likely to be reduced. Scaling to submicron dimensions would enable the creation of a one or even two dimensional array of microtraps each containing a single atom [48]. This may be of interest to study tunneling between neighbouring traps [90] and for quantum information [91].

The maximum density of atoms in the double-loop microtrap is limited by Majorana transitions that occur at the trap center where the magnetic field is zero. It has been proposed to add two straight microwires on either side of the microtrap array to generate a finite field at the trap minimum position [48]. Such a trap would also facilitate evaporatively cooling the microtrapped atoms to achieve lower temperatures

[40, 41].

A very important characteristic of the double-loop microtrap is the ability to precisely control its location using a bias field. The microtrap position could be tuned from 300 μm to 50 μm above the chip surface. This minimum distance is determined by the inner loop size r_1. Hence, a reduction of the microtrap size by a factor of 5 would mean the trapped atoms could be precisely positioned 10 μm above the chip. This would facilitate the study of effects such as the van der Waals interaction of an atom with its mirror image that scales as the inverse of the 6^{th} power of the atom distance to the surface [92]. Atoms in the double-loop microtrap are not positioned above a microwire unlike other microtraps. Hence, this microtrap is ideally suited for surface studies. In conclusion, the double-loop microtrap has significant potential to generate diverse applications.

A Current control circuit

Currents to the atom chip, z-bias coil, x and y-bias coils must be turned on/off during the experiment in a time of less than 1 ms. This was done using the current control circuits originally designed by B. Lü [93] and described in the thesis of B. Schultz [94]. Figure A.1 shows the circuit in the separate "current control boxes" that controlled the z-bias coil (ICC-01) and the atom chip (ICC-02) currents. The coil power supply, operated in constant voltage mode at 15 V, could not be suddenly shut off without being damaged by the back electromotive force. A circuit was therefore constructed to dissipate the current in a dummy load resistor R_D (10.5 Ω). The central part of the circuit is an IRFPS3810 MOSFET which was connected in series to the z-bias coil. The current passing through the coil was determined by the voltage input which was specified by the LabVIEW interface program described in Appendix B. This signal first passed through a preamplifier (OP77). This was followed by an integration stage which stabilized the current using the voltage measured across a sensing resistor R_S (5 mΩ, Isotek RUG-Z-R005-0.1). The feedback loop also consisted of a high performance amplifier (AD624AD) and an external resistor R_G (500 Ω, HR255N). The dependence of the current through the z-bias coil on the Labview input signal is shown in Figure A.2.

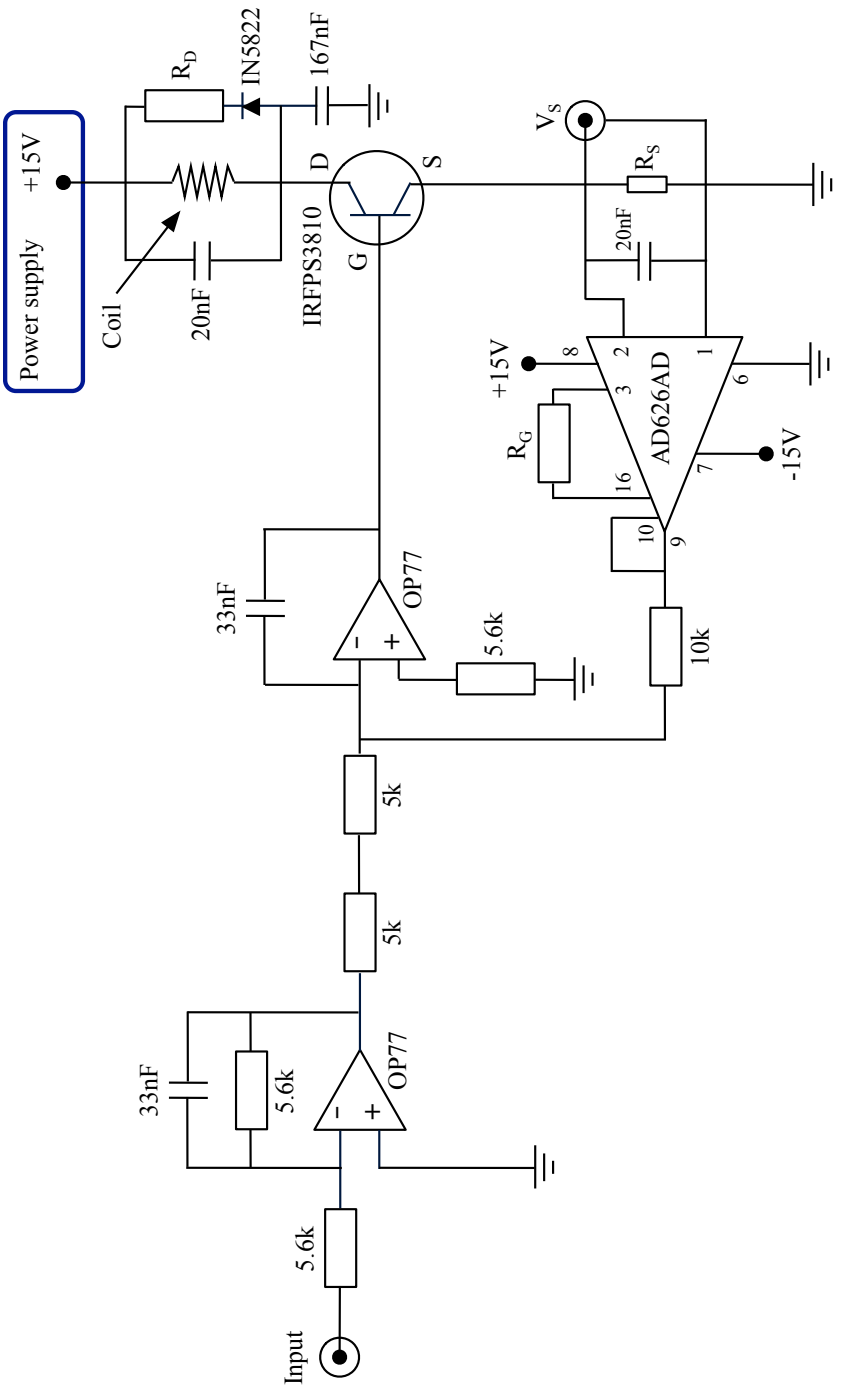

Figure A.1: Circuit used to control the z-bias coil current.

A similar circuit controlled the x (ICC-03) and y-bias (ICC-04) currents. The primary difference was that the required currents were smaller, less than 3 A. The current dependence on the input control signals analogous to that shown in Figure A.2 were found for the x-bias and y-bias coils to be 1.478 and 0.9739 A/V, respectively. The corresponding value for the atom chip circuit was 1.905 A/V. These values were input into the LabVIEW programs that interfaced the power supply to the computer as is discussed in Appendix B. The time to switch the maximum currents on/off in each of the four coils was measured to be less than 1 ms.

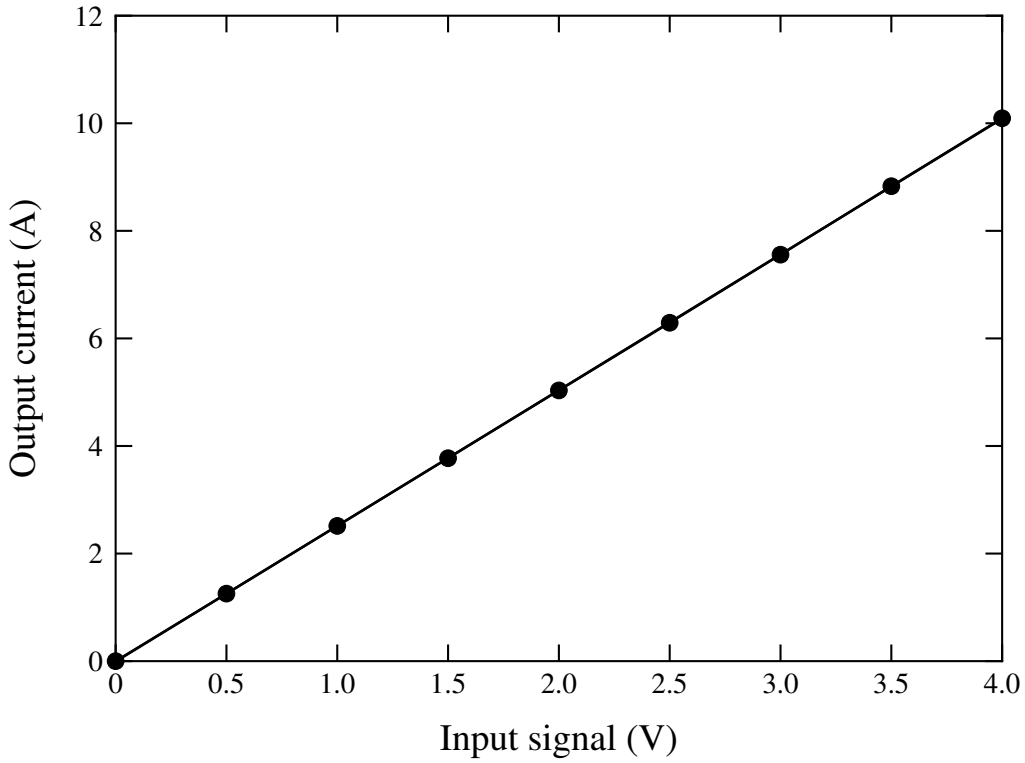

Figure A.2: Dependence of the z-bias coil current on input control signal. A line fitted to the data has a slope of 2.523 A/V.

B LabVIEW interface

Three different LabVIEW programs were written as illustrated in Figures B.1, B.2, and B.3. These programs loaded atoms into the microtrap array from 1) a transported quadrupole trap, 2) a mirror MOT and 3) a FORT. The front panel of each LabVIEW program set various parameters such as the times of the different stages of the experimental procedure, laser powers and the currents of the various coils.

The LabVIEW program generated values for up to 8 analog and 8 digital channels every 0.1 ms for up to 15 s. The output voltage of an analog channel ranged from -10 V to 10 V. For a digital channel, the output was either 5 V ("True") or 0 V ("False") which switched an instrument such as a shutter either open or closed. An example of the LabVIEW program to implement the time dependent atom chip current shown in Figure B.4 is given in Figure B.5. The black rectangular box known as a "frame" generated the analog signal that controlled the power supply that supplied the atom chip current. Similarly, the case of a digital channel that opened/shut the trap laser shutter as shown in Figure B.7 is given by the LabVIEW program in Figure B.6. The complete LabVIEW program consisted of a separate frame for each of the 8 analog and 8 digital channels. The resulting signals were sent to the data acquisition card which was linked to the National Instruments SCB68 connector block. The latter was connected to the various wires of the interfaced instruments and power supplies.

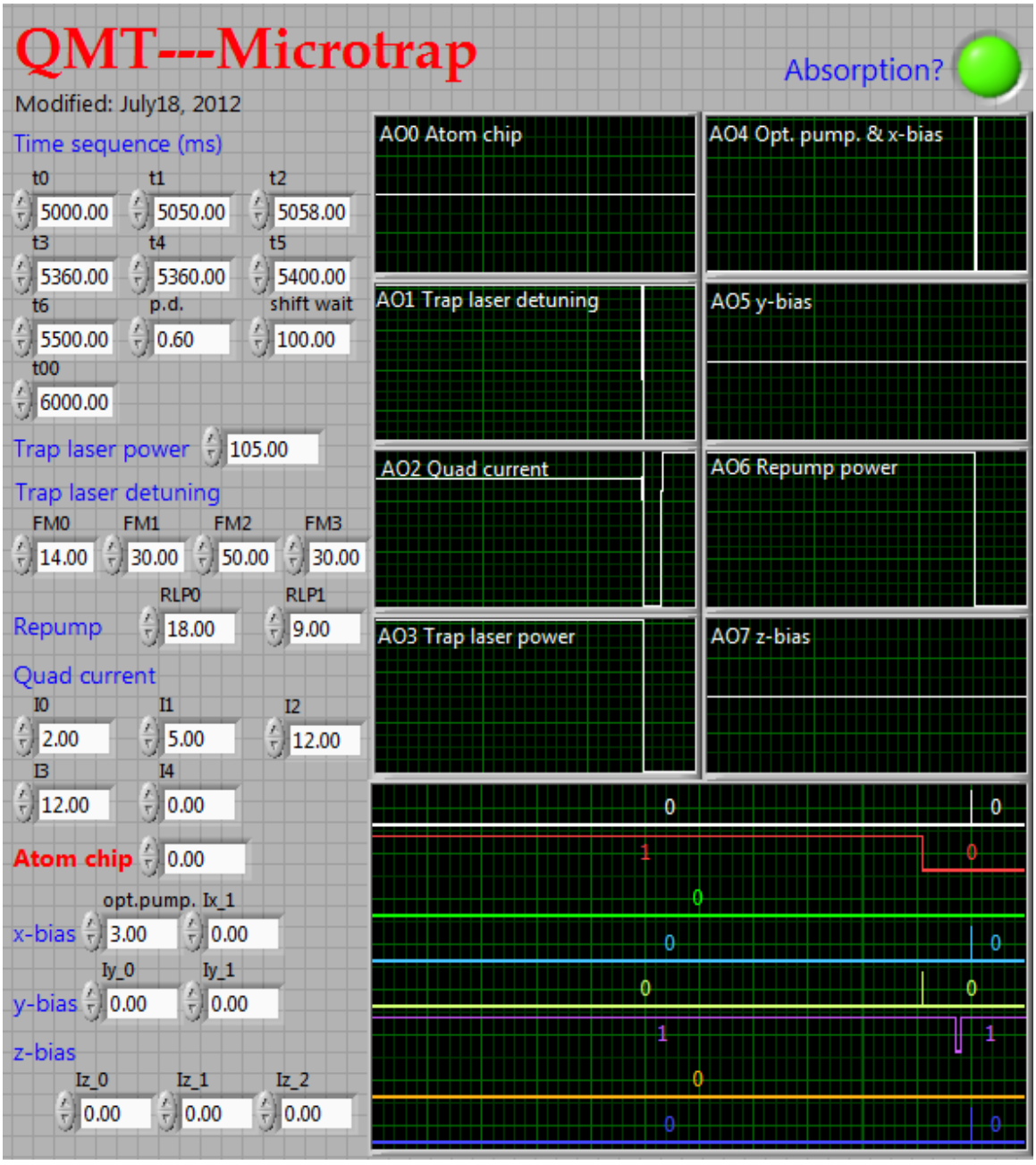

Figure B.1: Snapshot of the LabVIEW front panel used to load atoms into the microtrap from the transported quadrupole magnetic trap. The units for the trap and repump laser powers are in mW, the trap detuning is in MHz while the currents are in A.

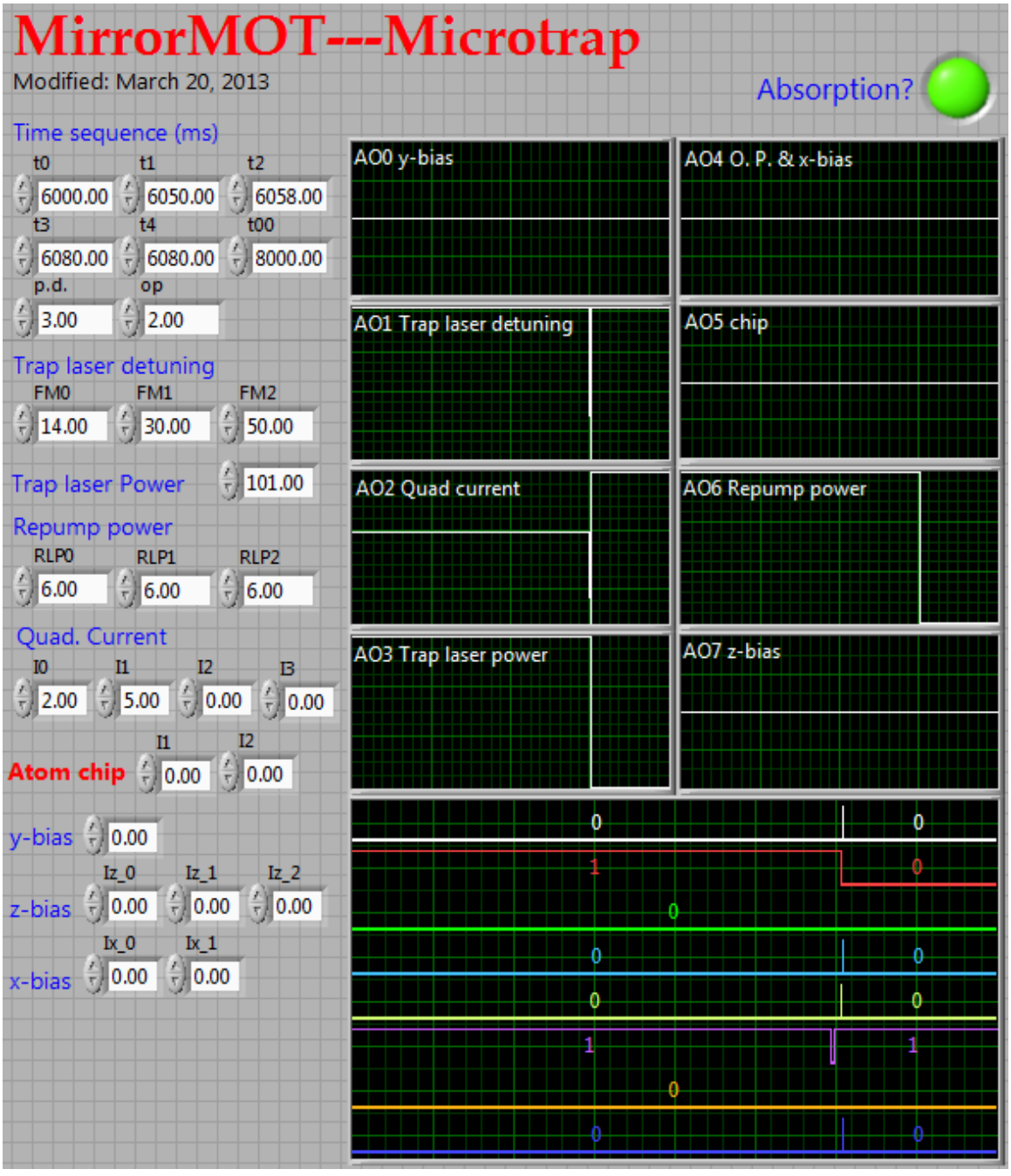

Figure B.2: Snapshot of the LabVIEW front panel used to load atoms into the microtrap from the mirror MOT. The units for the trap and repump laser powers are in mW, the trap detuning is in MHz while the currents are in A.

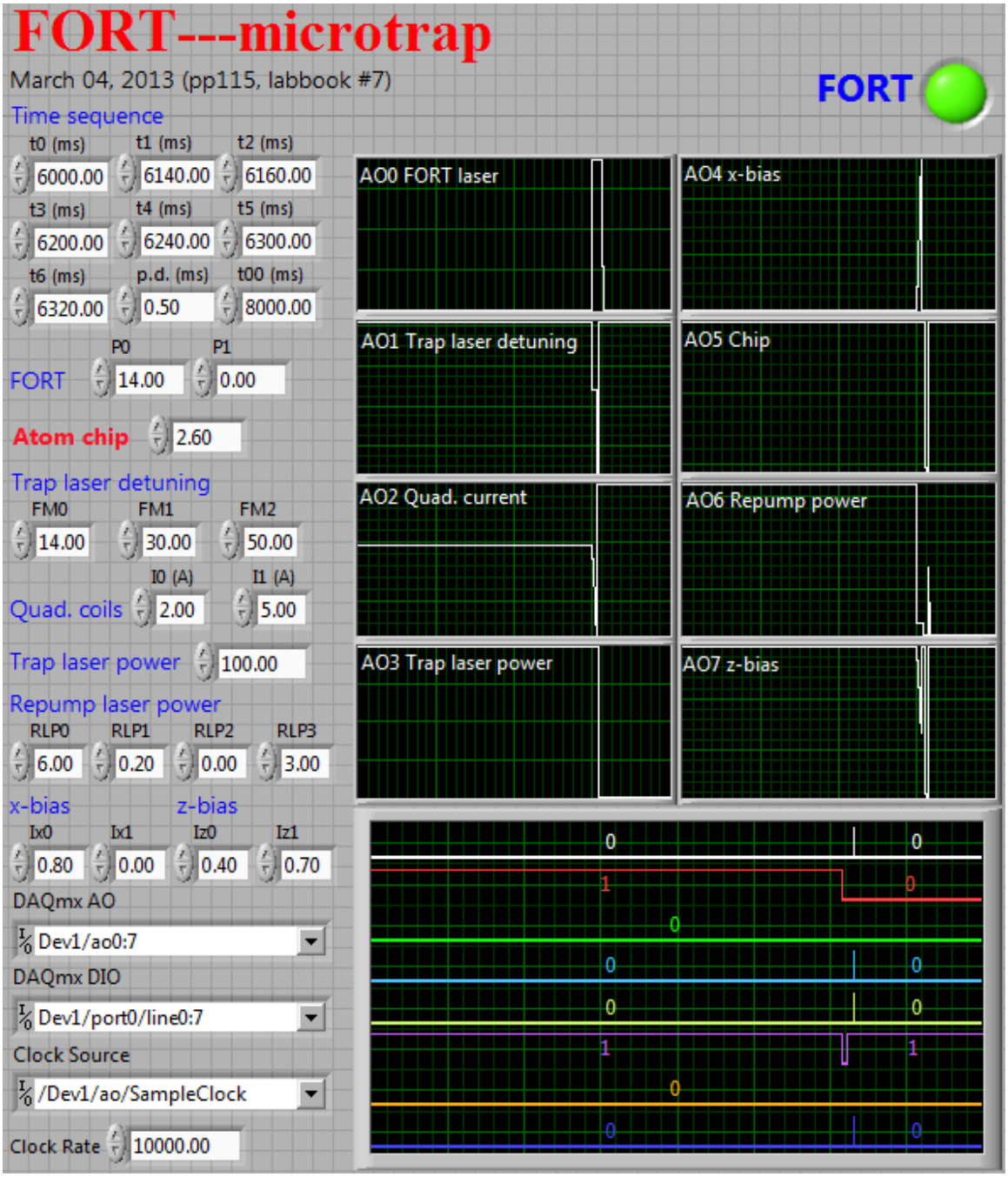

Figure B.3: Snapshot of the LabVIEW front panel used to load atoms into the microtrap from the FORT. The units for the trap and repump laser powers are in mW while the FORT laser power is in W. The trap detuning is in MHz and the currents are in A.

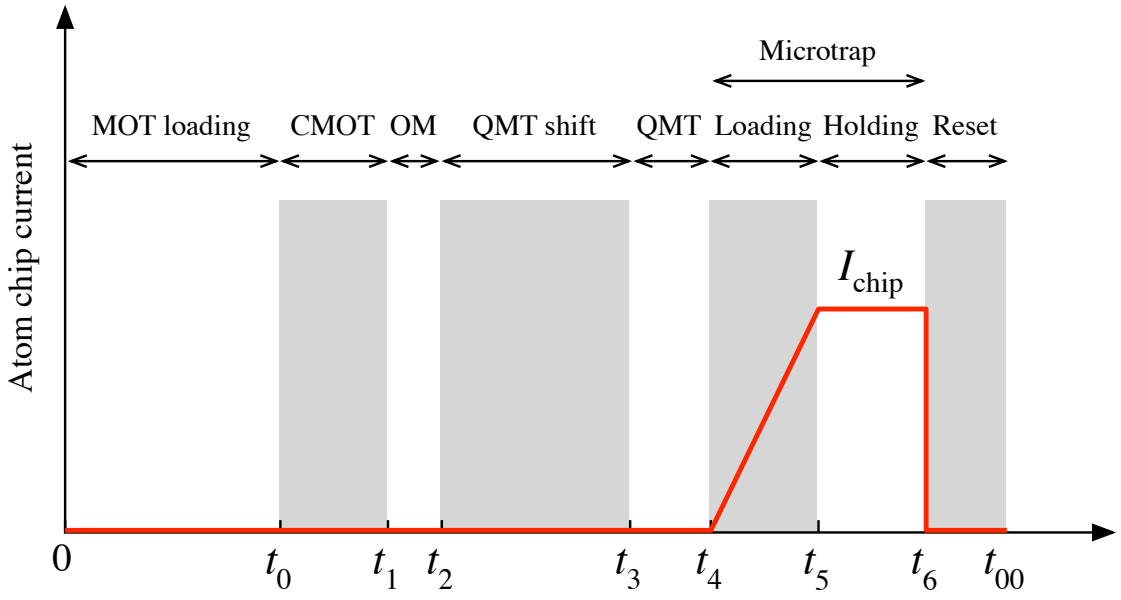

Figure B.4: Sample analog channel timing diagram of the atom chip current.

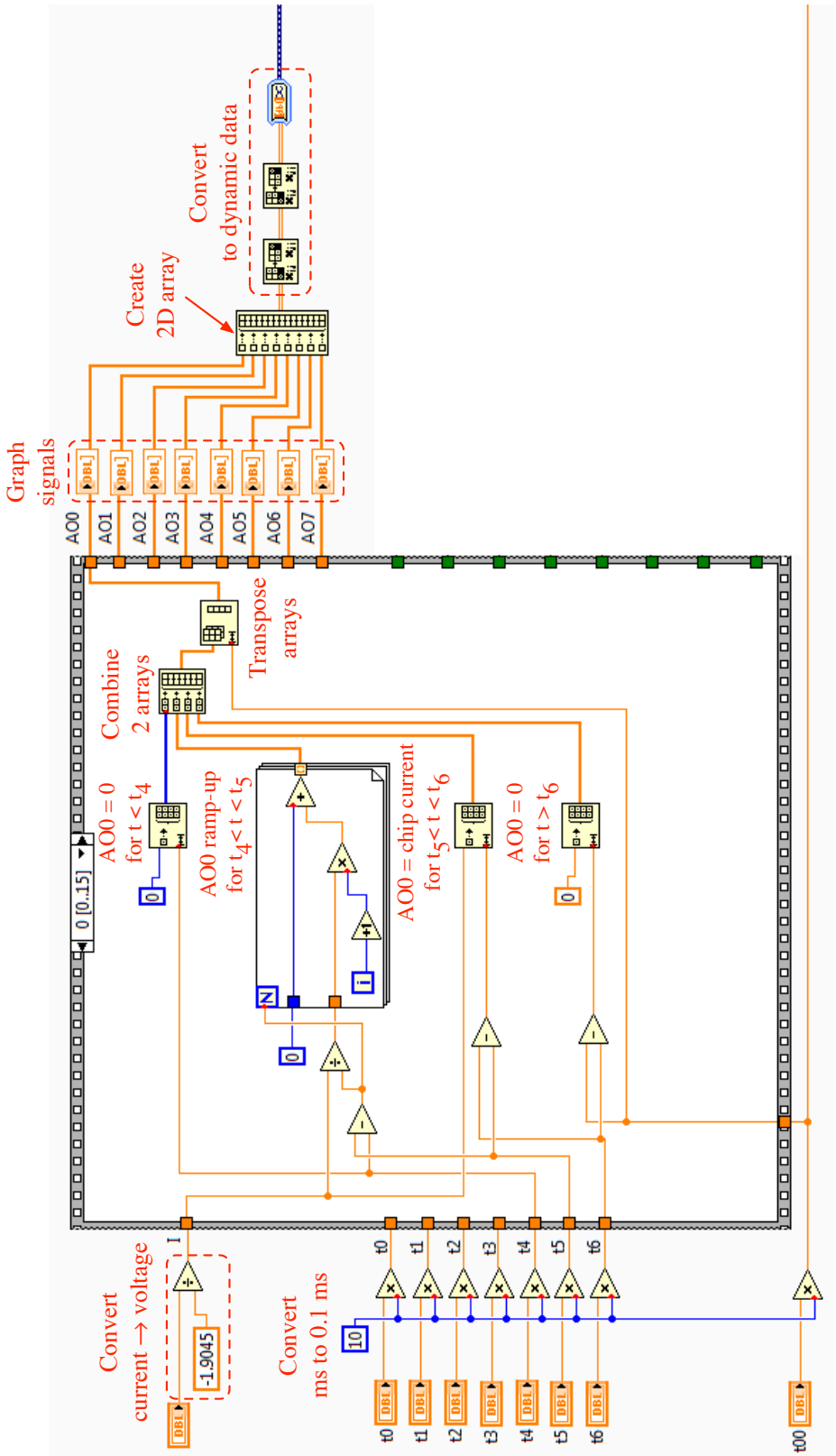

Figure B.5: LabVIEW program of the AO0 channel whose timing sequence is shown in Figure B.4.

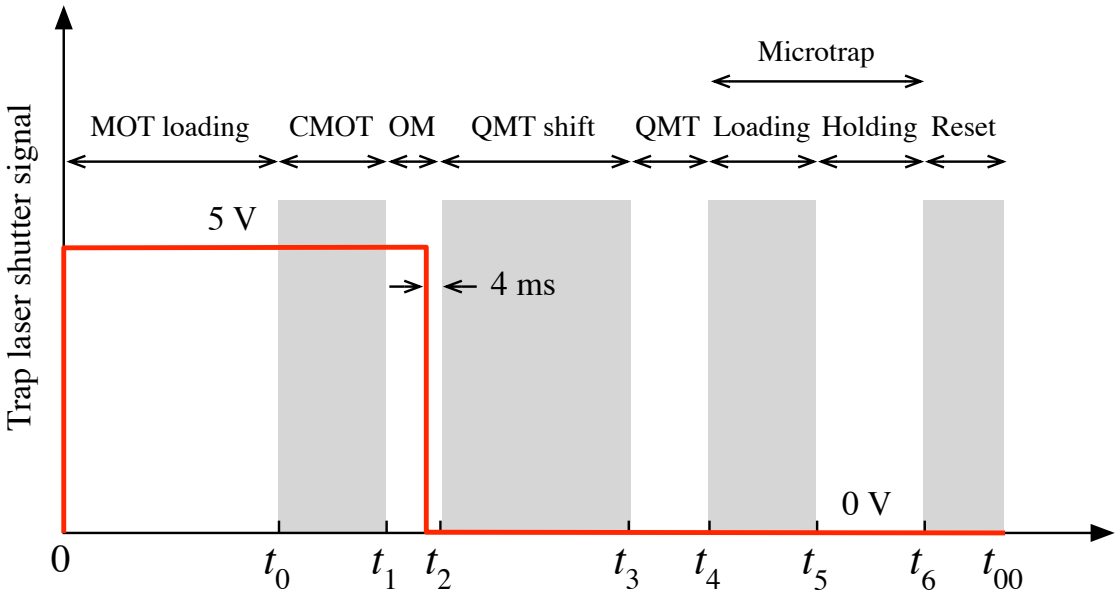

Figure B.6: Sample digital channel timing diagram of the trap laser shutter. The shutter response time is 4 ms. Hence, in order to close the shutter at time t_2, the signal must arrive 4 ms earlier.

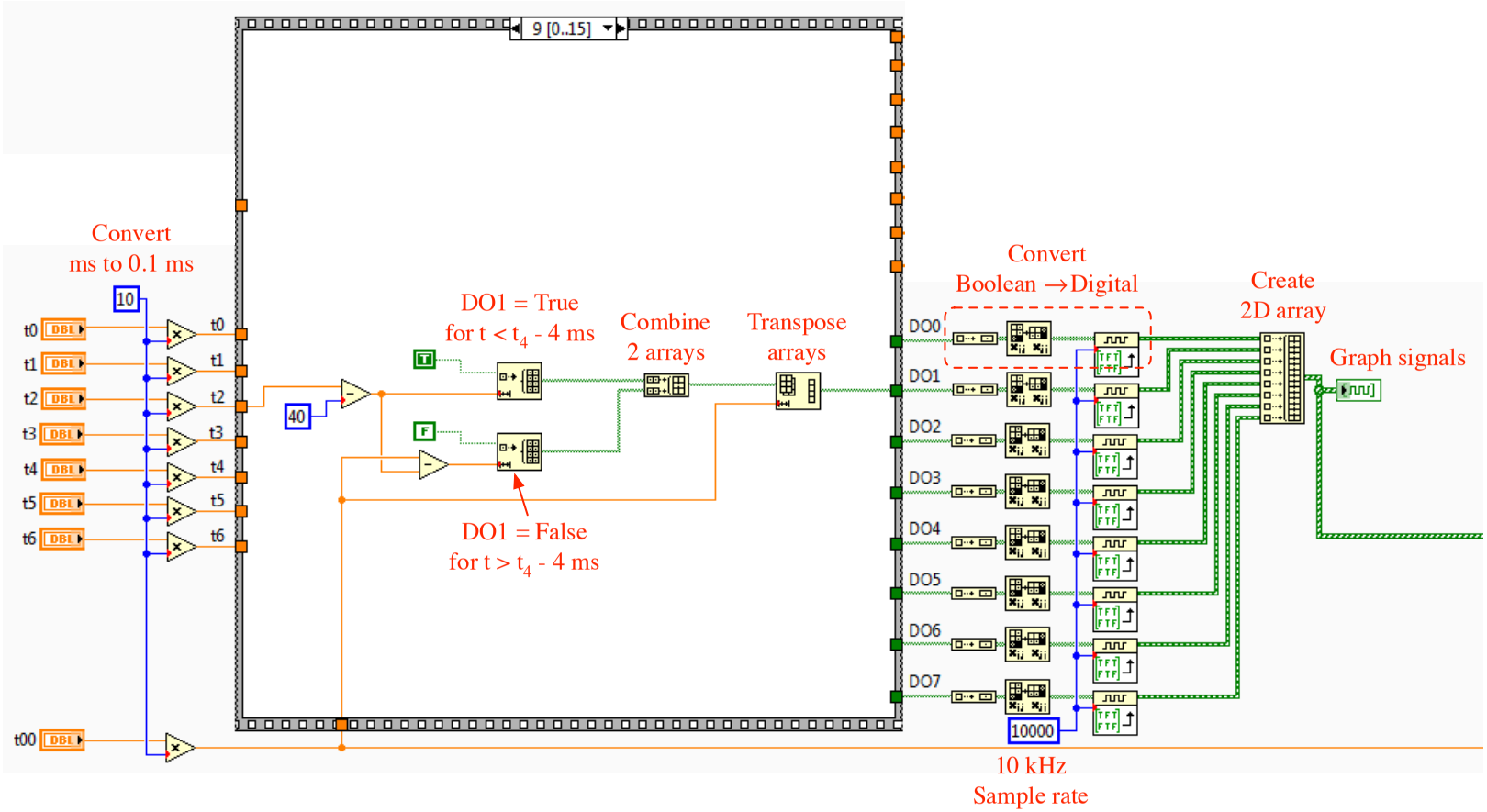

Figure B.7: Snapshot of the LabVIEW program diagram of the DO1 channel whose timing sequence is given in Figure B.6.

C Absorption imaging of cold atoms

Absorption imaging refers to the transmission of the imaging laser beam, which is in resonance with an atomic transition, through an ultracold atom cloud as is illustrated in Figure C.1. The intensity of the spatial profile of the transmitted laser beam was measured by a CCD camera. The objective was to determine the number and density of the trapped atoms.

The imaging laser beam propagated in the x direction. The intensity of the imaging laser beam incident on the atom cloud was given by $I_0(y,z)$. In our experiments, the imaging laser intensity was much less than the saturation intensity of the atomic transition. The imaging laser linewidth was also less than the transition linewidth. The imaging laser intensity transmitted through the atom cloud is given by

$$I(y,z) = I_0(y,z)e^{-\mathrm{OD}(y,z)} \tag{C.1}$$

where the optical depth is defined by

$$\mathrm{OD}(y,z) = \sigma \int_{-\infty}^{\infty} n(x,y,z)dx. \tag{C.2}$$

Here σ is the absorption cross section and $n(x,y,z)$ is the atom density. The on-

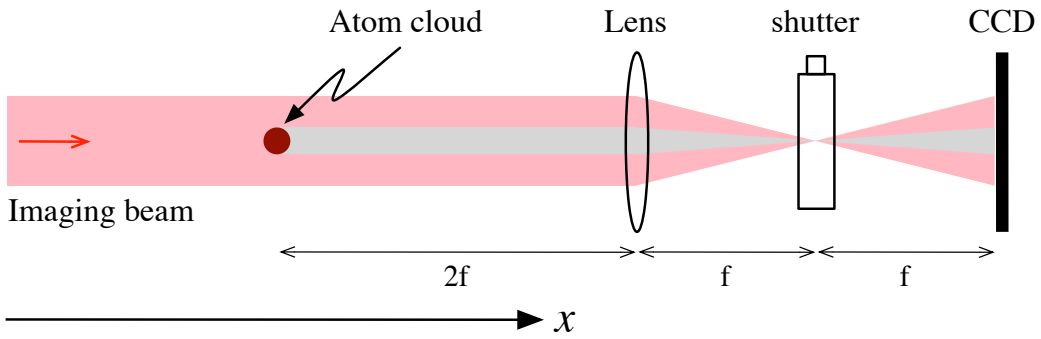

Figure C.1: Schematic of the absorption imaging method. f is the focal length of the lens.

resonance cross section σ is defined as

$$\sigma = \frac{\hbar\omega\gamma}{2I_{\rm sat}}, \tag{C.3}$$

where ω is the angular frequency of the transition, γ is the inverse of the excited state lifetime and $I_{\rm sat}$ is the saturation intensity of the transition. The on resonance absorption cross section σ for the Rb D2 transition equals 1.94 and 2.91×10^{-9} cm^2 for linearly polarized and circularly polarized light, respectively [51].

The total number of trapped atoms was found by integrating the atom density.

$$\begin{aligned} N &= \int_{-\infty}^{\infty}\int_{-\infty}^{\infty}\int_{\infty}^{\infty} n(x,y,z)dxdydz \\ &= \frac{1}{\sigma}\int_{-\infty}^{\infty}\int_{-\infty}^{\infty} \mathrm{OD}(y,z)dydz \\ &= -\frac{1}{\sigma}\int_{-\infty}^{\infty}\int_{-\infty}^{\infty} \ln\left(\frac{I(y,z)}{I_0(y,z)}\right)dydz \end{aligned} \tag{C.4}$$

In the experiments, three types of CCD images were taken. $S^0(y,z)$ was the CCD signal recorded when no atoms were trapped. The background signal $S^{\rm bk}(y,z)$ was taken when the imaging laser was blocked. Finally, $S(y,z)$ was the signal obtained when the imaging laser passed through the atom cloud. The CCD had a linear response to the light intensity which was checked using a calibrated neutral density filter. Subtracting the nonzero background CCD signal, the expression for the atom number becomes

$$\begin{aligned} N &= -\frac{1}{\sigma}\int_{-\infty}^{\infty}\int_{-\infty}^{\infty} \ln\left(\frac{S(y,z)-S^{\rm bk}(y,z)}{S^0(y,z)-S^{\rm bk}(y,z)}\right)dydz \\ &= -\frac{A_{\rm pixel}}{\sigma}\sum_{i,j}\ln\left(\frac{S_{i,j}-S^{\rm bk}_{i,j}}{S^0_{i,j}-S^{\rm bk}_{i,j}}\right), \end{aligned} \tag{C.5}$$

where the two dimensional integral has been replaced by a summation over all pixels encompassing the image in the y and z directions. A_{pixel} was the area of a single pixel.

In the experiments, the atom cloud density was observed to be well approximated by a gaussian distribution

$$n(x,y,z) = n_0 \exp\left[-\left(\frac{x^2}{2\sigma_x^2} + \frac{y^2}{2\sigma_y^2} + \frac{z^2}{2\sigma_z^2}\right)\right]. \tag{C.6}$$

This expression can be integrated to give the total number of trapped atoms N. The peak density n_0 is given by

$$n_0 = \frac{N}{(2\pi)^{3/2}\sigma_x\sigma_y\sigma_z}. \tag{C.7}$$

The cloud radii σ_i where $i = x, y, z$ could be determined from the absorption images.

D Glossary

Abbreviation	Term
AO	Analog Output
AOM	Acoustooptic Modulator
BEC	Bose Einstein Condensation
BS	Beamsplitter
CCD	Charged Coupled Device
CMOT	Compressed Magneto Optical Trap
DAQ	Data Acquisition
DO	Digital Output
FORT	Far Off Resonance Optical Dipole Trap
FWHM	Full Width Half Maximum
HW	Half Wave
ICC	Current Control Circuit
MOT	Magneto Optical Trap
OM	Optical Molasses
OP	Optical Pumping

Abbreviation	Term
OI	Optical Isolator
PBS	Polarizing Beamsplitter
PD	Photodiode
PGC	Polarization Gradient Cooling
QMT	Quadrupole Magnetic Trap
QW	Quarter Wave
RGA	Residual Gas Analyzer
TSP	Titanium Sublimation Pump
UHV	Ultra High Vacuum

Bibliography

[1] E. Arimondo, M. Inguscio and P. Violino, *Rev. Mod. Phys.*, **49**, 31, 1977.

[2] W. A. van Wijngaarden and B. Jian, *Eur. Phys. J. Special Topics*, **222**, 2057, 2013.

[3] W Demtröder, *Laser Spectroscopy*, Springer-Verlag, 1982.

[4] W. E. Lamb and R. C. Retherford, *Phys. Rev.*, **72**, 241, 1947.

[5] S. G. Karshenboim, *Phys. Rep.*, **422**, 1, 2005.

[6] G. A. Noble, B. E. Schultz, H. Ming and W. A. van Wijngaarden, *Phys. Rev. A*, **74**, 012502, 2006.

[7] S. Chu, *Rev. Mod. Phys.*, **70**, 685, 1998.

[8] C. N. Cohen-Tannoudji, *Rev. Mod. Phys.*, **70**, 707, 1998.

[9] W. D. Phillips, *Rev. Mod. Phys.*, **70**, 721, 1998.

[10] C. Monroe, W. Swann, H. Robinson and C. Wieman, *Phys. Rev. Lett.*, **65**, 1571, 1990.

[11] E. L. Raab, M. Prentiss, A. Cable, S. Chu and D. E. Pritchard, *Phys. Rev. Lett.*, **59**, 2631, 1987.

[12] W. D. Phillips and H. Metcalf, *Phys. Rev. Lett.*, **48**, 596, 1982.

[13] J Dalibard and C. Cohen-Tannoudji, *J. Opt. Soc. Am. B*, **6**, 2023, 1989.

[14] P. J. Ungar, D. S. Weiss, E. Riis and S. Chu, *J. Opt. Soc. Am. B*, **6**, 2058, 1989.

[15] D. S. Weiss, E. Riis, Y. Shevy, P. J. Ungar and S. Chu, *J. Opt. Soc. Am. B*, **6**, 2072, 1989.

[16] A. Einstein, *Sitzungsber. Kgl. Preuss. Akad. Wiss.*, **1925**, 3, 1925.

[17] C. J. Pethick and H. Smith, *Bose-Einstein Condensation in Dilute Gases*, Cambridge University Press, 2008.

[18] M. H. Anderson, J. R. Ensher, M. R. Matthews, C. E. Wieman and E. A. Cornell, *Science*, **269**, 198, 1995.

[19] K. B. Davis, M. O. Mewes, M. R. Andrews, N. J. van Druten, D. S. Durfee, D. M. Kurn and W. Ketterle, *Phys. Rev. Lett.*, **75**, 3969, 1995.

[20] E. A. Cornell and C. E. Wieman, *Rev. Mod. Phys.*, **74**, 875, 2002.

[21] W. Ketterle, *Rev. Mod. Phys.*, **74**, 1131, 2002.

[22] B. DeMarco and D. S. Jin, *Science*, **285**, 1703, 1999.

[23] S. Chu, J. E. Bjorkholm, A. Ashkin and A. Cable, *Phys. Rev. Lett.*, **57**, 314, 1986.

[24] J. D. Miller, R. A. Cline and D. J. Heinzen, *Phys. Rev. A*, **47**, R4567, 1993.

[25] R. Grimm, M. Weidemueller and Y. B. Ovchinnikov, *Adv. At. Mol. Opt. Phys.*, **42**, 95, 2000.

[26] A. L. Migdall, J. V. Prodan, W. D. Phillips, T. H. Bergeman and H. J. Metcalf, *Phys. Rev. Lett.*, **54**, 2596, 1985.

[27] T. Bergeman, G. Erez and H. J. Metcalf, *Phys. Rev. A*, **35**, 1535, 1987.

[28] C. C. Bradley, C. A. Sackett, J. J. Tollett and R. G. Hulet, *Phys. Rev. Lett.*, **75**, 1687, 1995.

[29] M.-O. Mewes, M. R. Andrews, N. J. van Druten, D. M. Kurn, D. S. Durfee and W. Ketterle, *Phys. Rev. Lett.*, **77**, 416, 1996.

[30] C. J. Myatt, E. A. Burt, R. W. Ghrist, E. A. Cornell and C. E. Wieman, *Phys. Rev. Lett.*, **78**, 586, 1997.

[31] T. Esslinger, I. Bloch and T. W. Hänsch, *Phys. Rev. A*, **58**, R2664, 1998.

[32] U Ernst, A Marte, F Schreck, J Schuster and G Rempe, *Europhys. Lett.*, **41**, 1, 1998.

[33] J. D. Weinstein and K. G. Libbrecht, *Phys. Rev. A*, **52**, 4004, 1995.

[34] J. Reichel, W. Hänsel and T. W. Hänsch, *Phys. Rev. Lett.*, **83**, 3398, 1999.

[35] R. Folman, P. Krüger, D. Cassettari, B. Hessmo, T. Maier and J. Schmiedmayer, *Phys. Rev. Lett.*, **84**, 4749, 2000.

[36] J. Fortágh and C. Zimmermann, *Rev. Mod. Phys.*, **79**, 235, 2007.

[37] S. Groth, P. Krüger, S. Wildermuth, R. Folman, T. Fernholz, J. Schmiedmayer, D. Mahalu and I. Bar-Joseph, *Appl. Phys. Lett.*, **85**, 2980, 2004.

[38] J. Reichel, *Appl. Phys. B*, **74**, 469, 2002.

[39] S. Du, M. B. Squires, Y. Imai, L. Czaia, R. A. Saravanan, V. Bright, J. Reichel, T. W. Hänsch and D. Z. Anderson, *Phys. Rev. A*, **70**, 053606, 2004.

[40] W. Hänsel, P. Hommelhoff, T. W. Hänsch and J. Reichel, *Nature*, **413**, 498, 2001.

[41] H. Ott, J. Fortágh, G. Schlotterbeck, A. Grossmann and C. Zimmermann, *Phys. Rev. Lett.*, **87**, 230401, 2001.

[42] Y.-J. Lin, I. Teper, C. Chin and V. Vuletić, *Phys. Rev. Lett.*, **92**, 050404, 2004.

[43] G. Birkl and J. Fortágh, *Laser & Photon. Rev.*, **1**, 12, 2007.

[44] Y. Colombe, T. Steinmetz, G. Dubois, F. Linke, D. Hunger and J. Reichel, *Nature*, **450**, 272, 2007.

[45] P. Treutlein, D. Hunger, S. Camerer, T. W. Hänsch and J. Reichel, *Phys. Rev. Lett.*, **99**, 140403, 2007.

[46] D. Hunger, S. Camerer, T. W. Hänsch, D. König, J. P. Kotthaus, J. Reichel and P. Treutlein, *Phys. Rev. Lett.*, **104**, 143002, 2010.

[47] P. Treutlein, P. Hommelhoff, T. Steinmetz, T. W. Hänsch and J. Reichel, *Phys. Rev. Lett.*, **92**, 203005, 2004.

[48] W. A. van Wijngaarden, *Can. J. Phys.*, **83**, 671, 2005.

[49] W. A. van Wijngaarden, *J. Quant. Spectrosc. Radiat. Transfer*, **57**, 275, 1997.

[50] M. S. Safronova, C. J. Williams and C. W. Clark, *Phys. Rev. A*, **69**, 022509, 2004.

[51] D. A. Steck, *Rubidium 87 D Line Data*, *http://steck.us/alkalidata*, 2008.

[52] H. J. Metcalf and P. van der Straten, *Laser Cooling and Trapping*, Springer-Verlag, 1999.

[53] H. J. Metcalf and P. van der Straten, *J. Opt. Soc. Am. B*, **20**, 887, 2003.

[54] S. Chu, L. Hollberg, J. E. Bjorkholm, A. Cable and A. Ashkin, *Phys. Rev. Lett.*, **55**, 48, 1985.

[55] P. D. Lett, R. N. Watts, C. I. Westbrook, W. D. Phillips, P. L. Gould and H. J. Metcalf, *Phys. Rev. Lett.*, **61**, 169, 1988.

[56] C. Cohen-Tannoudji, J. Dupont-Roc and G. Grynberg, *Atom-Photon Interactions: Basic Processes and Applications*, John Wiley & Sons, Inc., 1998.

[57] W. Ketterle and D. E. Pritchard, *Appl. Phys. B*, **54**, 403, 1992.

[58] W. Happer, *Rev. Mod. Phys.*, **44**, 169, 1972.

[59] W. Happer and W. A. van Wijngaarden, *Hyperfine Interact.*, **38**, 435, 1987.

[60] B. Lü and W.A. van Wijngaarden, *Can. J. Phys.*, **82**, 81, 2004.

[61] W. Petrich, M. H. Anderson, J. R. Ensher and E. A. Cornell, *Phys. Rev. Lett.*, **74**, 3352, 1995.

[62] S. Wildermuth, P. Krüger, C Becker, M. Brajdic, S. Haupt, A. Kasper, R. Folman and J. Schmiedmayer, *Phys. Rev. A*, **69**, R030901, 2004.

[63] S. Schmid, G. Thalhammer, K. Winkler, F. Lang and J. Hecker Denschlag, *New J. Phys.*, **8**, 159, 2006.

[64] K. M. Fortier, S. Y. Kim, M. J. Gibbons, P. Ahmadi and M. S. Chapman, *Phys. Rev. Lett.*, **98**, 233601, 2007.

[65] D. Cano, H. Hattermann, B. Kasch, C. Zimmermann, R. Kleiner, D. Koelle and J. Fortágh, *Eur. Phys. J. D*, **63**, 17, 2011.

[66] C. Weitenberg, Ph.D. thesis, Ludwig Maximilian University of Munich, 2011.

[67] C. S. Adams, H. J. Lee, N. Davidson, M. Kasevich and S. Chu, *Phys. Rev. Lett.*, **74**, 3577, 1995.

[68] M. D. Barrett, J. A. Sauer and M. S. Chapman, *Phys. Rev. Lett.*, **87**, 010404, 2001.

[69] S. R. Granade, M. E. Gehm, K. M. O'Hara and J. E. Thomas, *Phys. Rev. Lett.*, **88**, 120405, 2002.

[70] A. E. Siegman, *Lasers*, University Science Books, 1986.

[71] J. T. Verdeyen, *Laser Electronics*, Englewood Cliffs, 1995.

[72] H. Ming and W. A. van Wijngaarden, *Can. J. Phys.*, **85**, 247, 2007.

[73] B. Jian and W. A. van Wijngaarden, *J. Opt. Soc. Am. B*, **30**, 238, 2013.

[74] B. Jian and W. A. van Wijngaarden, *Appl. Phys. B*, 2013, doi:DOI 10.1007/s00340-013-5573-4.

[75] J. M. Obrecht, R. J. Wild, M. Antezza, L. P. Pitaevskii, S. Stringari and E. A. Cornell, *Phys. Rev. Lett.*, **98**, 063201, 2007.

[76] H. Bender, P. W. Courteille, C. Marzok, C. Zimmermann and S. Slama, *Phys. Rev. Lett.*, **104**, 083201, 2010.

[77] P. Treutlein, Ph.D. thesis, Ludwig Maximilian University of Munich, 2008.

[78] C. Wieman and T. W. Hänsch, *Phys. Rev. Lett.*, **36**, 1170, 1976.

[79] D. W. Preston, *Am. J. Phys.*, **64**, 1432, 1996.

[80] C. J. Foot, *Atomic Physics*, Oxford University Press, 2005.

[81] S. Aubin, S. Myrskog, M. H. T. Extavour, L. J. LeBlanc, D. McKay, A. Stummer and J. H. Thywissen, *Nat. Phys.*, **2**, 384, 2006.

[82] B. Squires, Ph.D. thesis, University of Colorado at Boulder, 2008.

[83] M. Greiner, I. Bloch, T. W. Hänsch and T. Esslinger, *Phys. Rev. A*, **63**, 031401, 2001.

[84] H. J. Lewandowski, D. M. Harber, D. L. Whitaker and E. A. Cornell, *J. Low Temp. Phys.*, **132**, 309, 2003.

[85] K. M. O'Hara, M. E. Gehm, S. R. Granade and J. E. Thomas, *Phys. Rev. A*, **64**, 051403, 2001.

[86] S. J. M. Kuppens, K. L. Corwin, K. W. Miller, T. E. Chupp and C. E. Wieman, *Phys. Rev. A*, **62**, 013406, 2000.

[87] K. L. Corwin, S. J. M. Kuppens, D. Cho and C. E. Wieman, *Phys. Rev. Lett.*, **83**, 1311, 1999.

[88] K. M. O'Hara, S. R. Granade, M. E. Gehm and J. E. Thomas, *Phys. Rev. A*, **63**, 043403, 2001.

[89] M. Shiddiq, E. M. Ahmed, M. D. Havey and C. I. Sukenik, *Phys. Rev. A*, **77**, 045401, 2008.

[90] M. Schulz, H. Crepaz, F. Schmidt-Kaler, J. Eschner and R. Blatt, *J. Mod. Opt.*, **54**, 1619, 2007.

[91] D. Schrader, I. Dotsenko, M. Khudaverdyan, Y. Miroshnychenko, A. Rauschenbeutel and D. Meschede, *Phys. Rev. Lett.*, **93**, 150501, 2004.

[92] S. K. Lamoreaux, *Phys. Rev. Lett.*, **78**, 5, 1997.

[93] B. Lü, *Technical report*, York University, 2004.

[94] B. Schultz, Ph.D. thesis, York University, 2010.